UNIVERSIDAD NACIONAL AUTÓNOMA DE MÉXICO

CENTRO DE RADIOASTRONOMÍA Y ASTROFÍSICA

ESTUDIO EN RADIOFRECUENCIAS DE LÍNEAS DE RECOMBINACIÓN EN REGIONES HII GALÁCTICAS Y EXTRAGALÁCTICAS.

TESIS

QUE PARA OBTENER EL GRADO ACADÉMICO DE

DOCTOR EN CIENCIAS (ASTRONOMÍA)

P R E S E N T A

CARLOS ALANÍAS RODRÍGUEZ RICO

DIRECTORES DE TESIS:

DRA. YOLANDA GÓMEZ CASTELLANOS (CRyA, UNAM)

DR. W. MILLER GOSS (NRAO, USA)

2005

Dedicatorias

A mis padres, por su incondicional apoyo

A mis hermanos y a mi abuelo Máximo

CARR

Resumen

Esta tesis se enfoca en el estudio y determinación de las propiedades físicas y la cinemática del gas ionizado en regiones HII galácticas y extra-galácticas. Se presentan observaciones de radiocontinuo y líneas espectrales hechas con el "Very Large Array" (VLA) hacia regiones HII galácticas y galaxias externas con brote de formación estelar. En esta tesis se seleccionaron dos de las regiones HII más brillantes en nuestra galaxia: G34.26+0.15 y G5.89+0.89. De igual manera se seleccionaron las tres galaxias con brote de formación estelar más cercanas y más brillantes: M82, Arp 220 y NGC 253. En particular, Arp 220 es la galaxia ultraluminosa más cercana y al mismo tiempo la más lejana en la que se han observado líneas de recombinación en radio (RRLs). Debido a que estas fuentes son de las más cercanas y brillantes de su tipo, son excelentes para estudiar la cinemática y propiedades físicas del gas ionizado con alta resolución angular. Las observaciones de líneas de recombinación en radio (RRL) con alta resolución angular son muy útiles y necesarias para estudiar la cinemática del gas ionizado. La principal ventaja de las RRLs, contrariamente a la emisión en óptico, es que no son atenuadas por el polvo que se encuentra a lo largo de la línea de visión. Por lo tanto, es posible estudiar las regiones HII compactas y las regiones centrales de las galaxias con brote de formación estelar que en muchos casos no son detectables en el óptico o aún en el cercano infrarrojo.

Las regiones de formación estelar galácticas G34.26+0.15 y G5.89-0.39 fueron observadas en el radiocontinuo a 8.3 GHz y en la RRL H92α. Las observaciones de radiocontinuo a 8.3 GHz hacia G34.26+0.15 muestran una región HII con morfología cometaria y dos regiones HII ultracompactas llamadas A y B. Estas dos regiones HII ultracompactas muestran emisión libre-libre ópticamente gruesa con profundidades ópticas de ~ 2 a 8.3 GHz. La emisión de la línea H92α no se espera en regiones ópticamente gruesas, sin embargo se detectó hacia la componente ultracompacta A de G34.26+0.15. La detección de emisión de la línea H92α hacia A se explicó como proviene de gas ópticamente delgado que se encuentra rodeando a la parte más

compacta de la región. La región HII compacta G5.89-0.39 es particularmente interesante ya que la emisión extendida de radiocontinuo muestra una morfología bipolar mientras que la parte interna es esférica. El gas ionizado en G5.89-0.39 muestra gradientes de velocidad muy pronunciados en la línea H92α y se observa una estructura interna de cáscara en el radiocontinuo. Se modeló la emisión de radiocontinuo a 8.3 GHz y la emisión de línea H92α usando una estructura de disco que tiene una cavidad en el centro como fue sugerido anteriormente por Zijlstra y colaboradores. Los resultados de los modelos concuerdan con las observaciones. Por otro lado, la emisión de la línea H92α integrada sobre la parte oeste de G5.89-0.39 muestra un perfil de doble pico revelando movimientos menos ordenados que no pueden ser explicados solamente por rotación del disco (publicado en Rodríguez-Rico, C. A., Rodríguez L. F., y Gómez Y., 2002, RMxAA, 38, 3).

La región de formación estelar masiva G34.26+0.15 también fue estudiada en el radiocontinuo a 23 GHz y en las transiciones de inversión (2,2) y (3,3) de la molécula de amoníaco (NH$_3$). La molécula de amoníaco es un trazador de gas de alta densidad ($\sim 10^5$ cm^{-3}) y su estudio permite investigar la relación entre el gas ionizado y el gas molecular que rodea a estrellas masivas. Un grumo de amoníaco fue encontrado en G34.26+0.15 con emisión en las transiciones (2,2) y (3,3) hacia el noroeste de la región cometaria además de la estructura molecular previamente reportada en la literatura. Este grumo está asociado con emisión maser de agua y su temperatura rotacional, diámetro y masa molecular fueron estimadas. El grumo podría tener una estrella embebida y además de las estrellas masivas que excitan a las regiones HII previamente reportadas podrían haber otras estrellas jovenes de menor masa en la región (publicado en Gómez, Y., Rodríguez-Rico, C. A., Rodríguez, L. F., y Garay, G., 2000, RMxAA, 36, 161).

Las tres galaxias con brote de formación estelar estudiadas en esta tesis M82, Arp 220 y NGC 253 fueron observadas por primera vez con alta resolución angular a 43 GHz y en la RRL H53α usando los nuevos receptores del VLA a 7mm. Para estas observaciones se implementó una nueva técnica para observar las líneas anchas (> 300 km s^{-1}) que usualmente se observan en galaxias con brote de formación estelar. Esta técnica traslapa varios anchos de banda adyacentes para lograr una amplia cobertura en velocidad. La galaxia con brote de formación estelar M82 fue observada con el VLA en alta resolución angular (0.''6) en el radiocontinuo a 8.3 y a 43 GHz así como en las RRLs H92α y H53α. En el radiocontinuo a 8.3 GHz se identificaron 19 fuentes que no tienen contrapartes en catálogos publicados a otras frecuencias y a 43 GHz se identificaron cinco nuevas fuentes. La distribución espacial de la línea H92α es inhomogénea; se identificaron 27 fuentes de emisión de línea, cerca de la mitad de estas fuentes están asociadas con fuentes de continuo. Aunque se observó con baja señal a ruido, se detectó la línea H53α hacia M82. La emisión de línea

y de continuo se modelaron usando agrupamientos de regiones HII a diferentes distancias del núcleo. Las observaciones pueden ser interpretadas suponiendo varias componentes de densidad. El gas de alta densidad está caracterizado por regiones HII con densidad de $\sim 4 \times 10^4$ cm^{-3} y la componente de baja densidad es un factor de 10 más baja que la componente de alta densidad. La cinemática observada en la línea H92α confirma la presencia de un gradiente de velocidad de 26 km s^{-1} arcsec^{-1} en la región central. Este gradiente tan pronunciado se observa no solamente a lo largo del eje mayor sino también a grandes distancias a lo largo de una banda a un ángulo de posición de $\sim 150°$. La cinemática observada en las zonas de transición entre los dos plateaus determinados a partir de la distribución de luz en el cercano infrarrojo sugiere que el gas se mueve en una variedad de órbitas. Los datos de H92α también revelan la base de un flujo hacia el halo en el lado norte. El flujo está presente en el disco, aún a distancias cercanas al núcleo. Hay una conexión sugerida entre el flujo hacia el halo y el gas que fluye hacia el centro a través del plano de M82 (publicado en Rodríguez-Rico, C., Viallefond, F., Zhao, J.H., Goss, W. M., and Anantharamaiah, K. R., 2004, ApJ, 616, 783).

El sistema de "merger" ultraluminoso Arp 220 se observó en el radiocontinuo a 43 GHz y en la RRL H53α. Se observan dos picos de radiocontinuo a 43 GHz, E y W, que corresponden a cada núcleo galáctico y están separados por ~ 350 pc. Se determinó que los índices espectrales de ambas componentes, usando las imagenes a 8.3 y 43 GHz, son típicos de emisión sincrotrón. Estas observaciones de radiocontinuo a 43 GHz y de la línea H53α confirman las densidades de flujo predichas por los modelos de Anantharamaiah y colaboradores. La línea H53α traza regiones HII compactas (~ 0.1 pc) de alta densidad ($\sim 10^5$ cm^{-3}) en Arp 220. La emisión de la línea H53α muestra dos máximos cercanos a los picos de radiocontinuo no-térmicos y coinciden con los picos de emisión molecular de H_2CO. Las regiones de formación estelar reciente están localizadas principalmente en regiones que son cercanas a los dos picos de radiocontinuo, esto basado en el hecho de que existe una coincidencia espacial entre la emisión integrada de H53α y la emisión maser de H_2CO. Se observa un gradiente de velocidad en la RRL H53α hacia la componente E y un segundo gradiente de velocidad es detectado hacia la componente W. Ambos gradientes de velocidad están orientados a lo largo de ángulos de posición similares a los observados en el CO, HI y OH. La cinemática del gas ionizado de alta densidad, trazado por la línea H53α, concuerda con la presencia de dos discos que rotan en sentido contrario como es sugerido por las observaciones de CO y HI (aceptado en la revista ApJ, Rodríguez-Rico, C., Goss, W. M., Viallefond, F., Zhao, J.H., Gómez, Y., y Anantharamaiah, K. R., 2005).

Finalmente, se observó la región central de la galaxia espiral NGC 253 en el RRL H53α y en radiocon-

tinuo a 43 GHz con resolución angular de $1.''5 \times 1.''0$. Se reanalizaron observaciones de RRL H92α con resolución angular de $1.''5 \times 1.''0$ y $0.''36 \times 0.''21$. Se observa emisión de la línea H53α RRL hacia los $10''$ centrales de NGC 253, la cual tiene asociadas regiones compactas de radiocontinuo reportadas previamente. El gas ionizado localizado cerca del pico de radiocontinuo muestra un gradiente de velocidad pronunciado (110 km s^{-1} arcsec^{-1}) en la RRL H92α a una resolución angular de $0.''36 \times 0.''21$. El sentido y orientación de los gradientes de velocidad H53α y H92α concuerdan. Sin embargo, el sentido de los gradientes de velocidad observados en RRLs no concuerda con las observaciones previas de CO. Se estimo el radiocontinuo debida a emisión libre-libre y se estimó la tasa de formación estelar de ~ 1.3 M$_\odot$ año^{-1}. Se modeló la emisión de radiocontinuo y de RRLs H53α y H92α. Los modelos sugieren que existe una componente de gas ionizado de baja densidad ($\sim 10^3$ cm^{-3}) trazada por la RRL H92α y otra componente de gas ionizado de alta densidad ($\sim 10^3$ cm^{-3}) trazada por la RRL H53α. El gradiente de velocidad calculado de las observaciones de RRL H92α de alta resolución ($0.''36 \times 0.''21$) implica una masa dinámica de $\sim 7 \times 10^6$ M$\odot$. Esta masa dinámica concuerda con la masa de un objeto compacto que pudo haber sido acretado hace $\sim 10^7$ años en NGC 253. La acreción de este objeto podría explicar las diferencias observadas en los campos de velocidades del gas ionizado y el gas molecular. (artículo en preparación Rodríguez-Rico, C., Goss, W. M., Viallefond, F., Zhao, J.H., Gómez, Y., y Anantharamaiah, K. R., 2005).

Abstract

This thesis focuses on studying and determining the physical properties and kinematics of thermally ionized gas in galactic and extragalactic HII regions. Very Large Array (VLA) observations of radio continuum and spectral lines made toward galactic HII regions and starburst galaxies are presented. In this thesis we selected two of the brightest star forming regions in our Galaxy: G34.26+0.15 and G5.89+0.89. Following the same criteria, three of the closest and brightest starburst galaxies were selected: M82, Arp 220 and NGC 253. In particular, Arp 220 is the closest ultraluminous infrared galaxy and the farthest from which radio recombination lines have been observed. Thus, these sources are excellent targets to study the kinematics and physical properties of the ionized gas with high angular resolution. High angular resolution RRLs have been proven to be a very powerful and necesary tool to study the kinematics of the ionized gas from individual sources. The main advantage of RRLs, over optical emission, is that they are not attenuated by dust along the line of sight. Thus, it is possible to study compact HII regions and the nuclear region of starburst galaxies that in many cases are not detected at optical and even near-IR wavelengths.

The galactic star forming regions G34.26+0.15 and G5.89-0.39 were observed in continuum at 8.3 GHz and the H92α RRL. The 8.3 GHz radio continuum observations made toward G34.26+0.15 show a cometary HII region morphology and two ultracompact HII regions named A and B. These two ultracompact HII regions have a continuum optical depth at 8.3 GHz of $\sim$ 2. The H92α line emission is not expected toward regions with optically thick free-free emission. However, the H92α line is detected in the ultracompact component A of G34.26+0.15. The detection of H92α line emission toward A is explained as arising in an optically thin shell that sourrounds the ultracompact HII region. The compact HII region G5.89-0.39, is particularly interesting since the extended radio continuum emission shows a bipolar morphology, while the inner region is spherical. The ionized gas in this HII region shows strong velocity gradients in the H92α line and an inner shell-like structure in the radio continuum. Both the 8.3 GHz continuum and H92α line emission

toward G5.89-0.39 are modeled using a disk-like morphology with a cavity in the center as suggested by Zijlstra and collaborators. The model results are in reasonable agreement with the observations. On the other hand, the H92α line emission integrated over the western edge of G5.89-0.39 shows a double peaked profile that reveals less ordered motions which cannot be attributed only to rotation of the disk (published in Rodríguez-Rico, C. A., Rodríguez L. F., and Gómez Y., 2002, RMxAA, 38, 3).

The massive star forming region G34.26+0.15 was also studied in the radio continuum at 23 GHz and the inversion transitions (2,2) and (3,3) of the ammonia molecule (NH_3). The ammonia molecule in star forming regions traces the high-density ($\sim 10^5$ cm^{-3}) molecular gas. One ammonia clump was found in G34.26+0.15 with (2,2) and (3,3) emission toward the northwest in addition to the main molecular structure previously reported. This clump is associated with water maser spots and its rotational temperature, diameter and molecular mass are estimated. The clump could have an embedded star and in addition to the massive stars that excite the previously reported HII regions there may be other young stars of lower mass in the region (published in Gómez, Y., Rodríguez-Rico, C. A., Rodríguez, L. F., and Garay, G., 2000, RMxAA, 36, 161).

The three starburst galaxies studied in this thesis M82, Arp 220 and NGC 253 were observed for the first time at high angular resolution in the radio continuum at 43 GHz and the RRL H53α using the new receivers at 7 mm of the VLA. For these observations a new technical implementation was made in order to observe the broad RRLs (> 300 km s^{-1}) in starburst galaxies. This technique overlaps several adjacent bandwidths in order to obtain a larger velocity coverage. The starburst galaxy M82 was observed at high angular resolution (0.''6) in the radio continuum at 8.3 and 43 GHz as well as in the RRLs H92α and H53α. In the continuum at 8.3 GHz we identify 19 sources that have no counterparts in catalogs published at other frequencies and at 43 GHz we identify 5 sources that were unknown previously. The spatial distribution of the H92α line is inhomogeneous; we identify 27 line features, about half of them are associated with continuum emission sources. Although observed with poorer signal to noise ratio, the H53α line is detected. The line and continuum emission are modeled using a collection of HII regions at different distances from the nucleus. The observations can be interpreted assuming two density components but equally well with a single-density component. The high-density gas has a density of $\sim 4 \times 10^4$ cm^{-3} and the low-density component has a density a factor of 10 lower. The kinematics observed in the H92α line confirms the presence of a velocity gradient of $\sim$26 km s^{-1} arcsec^{-1} in the nuclear region. This steep gradient is observed not only on the major axis but also at large distances along a band of PA of $\sim 150°$. The kinematics observed suggests gas moving

in different orbits at the transition between the two plateaus observed in the NIR light distribution. The H92α data also reveal the base of the outflow on the Northern side. The outflow signature is present even in the disk at distances close to the nucleus. There is a suggested connection between the outflow and the gas flowing in the plane of M82 towards the center (published in Rodríguez-Rico, C., Viallefond, F., Zhao, J.H., Goss, W. M., and Anantharamaiah, K. R., 2004, ApJ, 616, 783).

The ultraluminous infrared merger system Arp 220 was observed in the radio continuum at 43 GHz and in the RRL H53α. Two radio continuum peaks that correspond to each galactic nucleus of the merger, E and W, are observed at 43 GHz and are separated by $\sim$ 350 pc. The spectral indices for both the E and W components, using radio continuum images at 8.3 and 43 GHz are typical of synchrotron emission. These 43 GHz continuum and H53α line observations confirm the flux densities predicted by the models of Ananthara-maiah and collaborators. The H53α line traces high-density ($\sim 10^5$ cm^{-3}) compact HII regions ($\sim$ 0.1 pc) in Arp 220. The H53α line emission has two maxima toward the non-thermal radio continuum peaks and are coincident with the peaks of molecular emission of H$_2$CO. The regions with recent star formation are located mainly in regions that are close to the two radio continuum peaks as suggested by the coincidence between the integrated H53α and the H$_2$CO maser line emission. A velocity gradient is observed in the H53α RRL toward the E component and a second velocity gradient is detected toward the W component. The velocity gradients are oriented along similar position angles as observed in previous CO, HI and OH observations. The kinematics of the high-density ionized gas traced by the H53α line are in agreement with two counter rotating disks as suggested by the CO and HI observations (accepted for publication to ApJ, Rodríguez-Rico, C., Goss, W. M., Viallefond, F., Zhao, J.H., Gómez, Y., and Anantharamaiah, K. R., 2005).

Finally, the nuclear region of the spiral galaxy NGC 253 was observed in the radio continuum at 43 GHz and the RRLs H53α and H92α. The H53α RRL emission is observed toward four sources that are located in the nuclear regions of NGC 253 and appear associated to previously reported compact continuum sources. The ionized gas located close to the radio continuum nucleus exhibits a large velocity gradient in both RRLs H53α and H92α (paper in preparation Rodríguez-Rico, C., Goss, W. M., Viallefond, F., Zhao, J.H., Gómez, Y., and Anantharamaiah, K. R., 2005).

Agradecimientos

Agradezco a mis asesores Yolanda Gómez y Miller Goss por la gran paciencia que me han tenido, así como el apoyo que me han brindado durante la realización de esta tesis. Por impulsarme a realizar trabajos con altos estándares y las valiosas discusiones que hemos tenido sobre el análisis de nuestras observaciones y guiarme a través de mi desarrollo profesional. A Francois Viallefond por sus grandes enseñanzas y valiosas aportaciones. Agradezco a Jun-Hui Zhao por sus valiosos comentarios y colaboración para realizar exitosamente nuestras observaciones y publicaciones. A Luis Felipe Rodríguez por sus ensenãnzas como profesor durante la maestría. También aprecio mucho el que siempre cediera su tiempo para leer los diferentes artículos que conforman esta tesis y contribuir en la mejora de su contenido.

Agradezco también a mi familia por todo el apoyo brindado, no solamente durante la realización de esta tesis, sino a lo largo de toda mi vida académica y personal. A mi Madre y a mi Padre por creer en mi, por crear en mi ese espiritu de superación y grandes expectativas. A mi hermana Mónica por creer siempre en mi y convivir conmigo durante tiempo de grandes tensiones profesionales. A mis hermanos por ser originales y siempre buscar lograr sus sueños, que a la vez han ayudado a inspirarme para lograr los mios. A Edith Vera por los grandes momentos que hemos compartido.

Agradezco a mis profesores de maestría, así como al personal académico y administrativo del Centro de Radioastronomía y Astrofísica, del Instituto de Astronomía de la UNAM y del National Radio Astronomy Observatory por su apoyo y buenos momentos de convivencia personal. Agradezco a mis amigos de Puebla Ingrid y Wendy Sánchez, Tricia Dillon, Carlos y Raúl Aguilera, Anna Soler, Sergio y Javier Zamora, Saray Guevara, Rene Manrique, Mónica Jimenez, Rafael Ferrer, Zacil Cinco y Teresa García, con quienes conviví durante mi primera etápa como estudiante de posgrado. Agradezco a mis compañeros predocs y posdocs en Socorro, Emmanuel Momjian, Itziar de Gregorio, Kumar Golap, Walter Brisken, Laurent Sjouverman, Fabian Walter, Eva Schrodinger, Cristal Brogan, Tiffany Borders, Jeff Kern, Kelsey Johnson, Ian Hoffman,

General Index

Capítulo 1

Formación estelar galáctica y extragaláctica

1.1 Regiones HII y formación estelar

Desde el punto de vista observacional, el estudio de la formación de estrellas masivas es un reto, debido principalmente a que las estrellas masivas permanecen embebidas en las nubes maternas durante la mayor parte de su vida dificultando su estudio con técnicas ópticas. Las escalas de tiempo de las diferentes etapas de la formación de estas estrellas transcurren muy rápido comparado con el tiempo de dispersión de la nube molecular donde se formaron. Los sitios de formación de estrellas masivas en nuestra galaxia están en el plano galáctico lo cual aunado a la extinción causada por el medio interestelar hace que su estudio se realice preferentemente mediante técnicas de radio (Wood & Churchwell 1989). Las estrellas masivas (20 − 50 veces la masa del Sol) producen gran cantidad de fotones que ionizan sus alrededores creando las llamadas regiones HII.

En esta tesis se realiza un estudio de las propiedades físicas de regiones HII, galácticas y extragalácticas, a través de observaciones de radiocontinuo y líneas de recombinación en radiofrecuencias (LRR). Las LRR y el radiocontinuo nos permiten determinar parametros físicos de las regiones HII tales como la temperatura, densidad electrónica, y estructura de velocidad. La principal motivación para estudiar las regiones HII es la íntima relación que tienen con las regiones de formación estelar y el hecho de que se encuentran entre los

objetos que más fácilmente pueden ser observados en nuestra Galaxia y en otras galaxias.

Las estrellas se forman a través de la compresión de nubes de gas molecular y polvo. Las nubes moleculares densas son parte del medio interestelar (MI) y están compuestas principalmente por H_2, moléculas complejas así como de polvo. El MI ocupa gran parte del volumen de la Galaxia, por lo que las observaciones del MI resultan de gran importancia para poder determinar la naturaleza de los procesos evolutivos que ocurren en nuestra galaxia. Sin embargo, la molécula de H_2 no se puede observar fácilmente de manera directa. El MI es enriquecido de elementos más pesados que el H a través de vientos estelares, nebulosas planetarias, novas y explosiones de supernovas. Son estos elementos pesados los que nos permiten estudiar las nubes moleculares. Los elementos pesados forman moléculas que funcionan como trazadoras de nubes moleculares de H_2. Algunas de estas moléculas, las cuales son más fácilmente observadas que el H_2, son el CO, OH, CS, H_2O, NH_3 y el H_2CO. De la observación de este tipo de trazadores de gas molecular se sabe que las nubes moleculares son estructuras inhomogeneas que contienen estructuras compactas muy densas y calientes. Los núcleos densos ($n_{H_2} \geq 10^7$ cm^{-3}) y tibios (T> 100 K) de las nubes moleculares son los sitios en donde se da inicio a la formación estelar (Garay & Lizano 1999; Kurtz et al. 2000).

La teoría más aceptada sobre la formación de las estrellas que conforman una asociación OB es que éstas se forman de manera casi simultanea. Desde las etapas tempranas de sus vidas, las estrellas comienzan a emitir radiación de acuerdo a su temperatura, y aún embebidas en la nube madre emiten radiación ultravioleta que es capaz de ionizar el gas que las rodea dando lugar a regiones HII. Sin embargo, los procesos físicos por los que pasa una nube molecular para formar estrellas y la influencia de las estrellas recien formadas en la nube molecular madre no están del todo claros. Para lograr este entendimiento es necesario determinar las propiedades físicas de las regiones HII y de las nubes moleculares. Debido a que la extinción por polvo puede ser muy importante en el óptico y aún en el infrarrojo, las observaciones en radio resultan ser esenciales para llevar a cabo la investigación de las propiedades de las regiones HII.

Las tasas de formación estelar (SFR, definida como la masa de estrellas, en un rango dado, formadas por unidad de tiempo, usualmente medida en $M_\odot$ por año) pueden variar en varios ordenes de magnitud de acuerdo al tipo de galaxia. Basados en su tasa de formación estelar, las galaxias han sido clasificadas como galaxias 'normales' y galaxias 'activas'. En nuestra Galaxia, la tasa de formación de estrellas es considerada dentro de los límites de una galaxia 'normal' (~ 1 $M_\odot$ año^{-1}). Las galaxias 'activas', donde la tasa de formación estelar

es mucho mayor ($\geq$ 3 $M_\odot$ año^{-1}) que en nuestra galaxia, son conocidas como galaxias 'starburst' (galaxias con brote de formación estelar).

A continuación se describen en detalle las características de las regiones HII, su relación con las regiones de formación estelar y se describe la manera en que se determinan sus parametros físicos usando observaciones del radiocontinuo y de líneas espectrales.

1.2   Características de las regiones HII

Tabla 1.1: PARÁMETROS FÍSICOS DE LAS REGIONES HII (Kurtz et al. 2002)

Tipo de Region HII	Tamaño (pc)	Densidad (cm^{-3})	ME (pc cm^{-6})	Masa ionizada ($M_\odot$)
Hipercompacta	~ 0.003	$\geq 10^6$	$\geq 10^{10}$	$\sim 10^{-3}$
Ultracompacta	≤ 0.1	$\geq 10^4$	$\geq 10^7$	$\sim 10^{-2}$
Compacta	≤ 0.5	$\geq 5 \times 10^3$	$\geq 10^7$	~ 1
Clásica	~ 10	~ 100	$\sim 10^2$	$\sim 10^5$
Gigante	~ 100	~ 30	$\sim 5 \times 10^5$	$10^3 - 10^6$
Supergigante	> 100	~ 10	$\sim 10^5$	$10^6 - 10^8$

Debido a que las estrellas de tipo temprano viven aproximandamente $10^6 - 10^7$ años, la presencia de regiones HII alrededor de estas estrellas masivas es indicativo de formación estelar reciente. Las estrellas tipo O y B emiten radiación ultravioleta capaz de ionizar el gas a su alrededor a una tasa de $> 10^{49}$ s^{-1}, creando regiones HII que pueden ser clasificadas de acuerdo a su tamaño en seis tipos de regiones. En la Tabla 1.1 se listan las características de los seis tipos de regiones HII (Kurtz et al. 2000). Los parámetros físicos que caracterizan a las regiones HII son su tamaño y densidad electrónica. La medida de emisión está definida por ME= $n_e^2 L$, en donde n_e es la densidad electrónica y L es el diámetro de la región HII. De acuerdo a la Tabla 1.1 las regiones HII más compactas ($\sim$ 0.003 pc) contienen gas más denso ($\sim 10^6$ cm^{-3}) que las regiones más extendidas ($\sim$ 10 pc). A través de sus luminosidades combinadas, una asociación OB es capaz de ionizar una región más grande de hidrógeno a su alrededor. Como las estrellas del Trapecio en Orión que producen una región ionizada con una extensión de $\sim$ 3 pc (Figura 1.1; Subrahmanyan 1992).

La gran variedad de tamaños que puede tener una región HII depende principalmente del número de fotones ionizantes (N_{Lyc}) disponibles de la asociación OB, la densidad electrónica n_e de la nube que la rodea y de la evolución dinámica de la región HII. La región ionizada es conocida también como esfera de Stromgren, que tiene un radio R_S definido, a

primera aproximación, por:

$$R_S = \left(\frac{N_{Lyc}}{\frac{4}{3}\pi n_e^2 \alpha_B(T)} \right)^{1/3} \tag{1.1}$$

donde $\alpha_B(T)$ es el coeficiente de recombinación del caso B, en el cual no se consideran las recombinaciones al nivel base.

Las nubes donde se da la formación estelar están compuestas en su mayor parte por hidrógeno ($\sim$ 75 %), aproximadamente 25 % de He y una pequeña parte está constituida por elementos más pesados ($<$ 1 %). La fotoionización producida por la estrella masiva no es instantanea en cualquier lugar de la esfera de Stromgren, esta ocurrirá solamente en la vecindad de la estrella. Al ser ionizada la región más cercana a la estrella, su temperatura varia desde una temperatura inicial de $\sim$ 100 K a temperatura final $\sim$ 10^4 K y un incremento de la densidad numérica en un factor de dos suponiendo puro hidrógeno. Entonces, la presión de la región ionizada será alrededor de 200 veces más grande que en el medio neutro que la rodea, suponiendo que sigue la ecuación de gases ideales. Por lo tanto, el gas ionizado se expandirá hacia la región neutra creando un frente de choque. El tamaño de la región HII depende del tiempo que tome expandirse la región con gas ionizado debido al frente de choque. La creación del frente de choque y la velocidad de expansión de la región con gas ionizada depende de la densidad del gas que rodea a la estrella y del viento asociado a esta. La expansión se detendrá al alcanzar el equilibrio de presiones entre el gas ionizado de la región HII y el gas neutro que la rodea.

De acuerdo a su morfología, las regiones HII ultracompactas se han clasificado principalmente en seis tipos (De Pree et al. 2005; Kurtz et al. 1994; Wood Churchwell 1989): cometarias (20 %), de estructura de cáscara (4 %), bipolares, irregulares (17 %), esféricas (17 %) y núcleo-halo (16 %). En la Figura 1.2 se muestran dos ejemplos de estos tipos de regiones HII, G5.89-0.24 es una región HII con estructura de cáscara y G34.26+0.15 es una region HII cometaria. La forma de las regiones HII depende de varios parámetros, como estructura de densidad del medio interestelar que rodea a la región HII, movimiento de la estrella ionizante respecto a la región HII, y a la dinámica del gas ionizado y neutro. La dependencia de la morfología respecto a estos parámetros no ha sido cuantificados apropiadamente, por lo que se han propuesto varios modelos: el modelo de flujo de champaña, el de choque de proa, el de discos fotoevaporados, el de confinamiento por presión y el de vientos cargados de masa (Garay & Lizano 1999).

Las regiones HII emiten radiación en diferentes longitudes de onda, desde el óptico hasta el radio. La emisión de radio de las regiones HII está dominada por radiación libre-
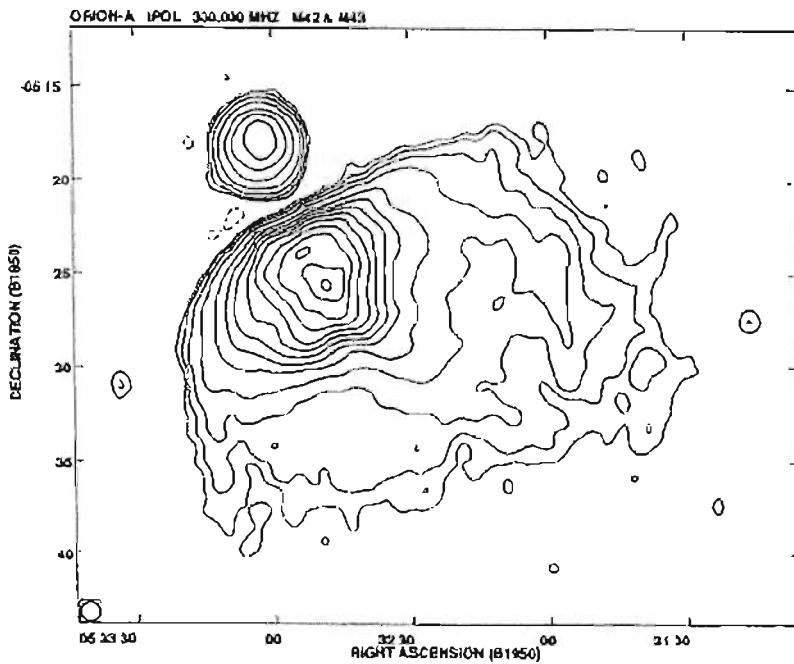
Figura 1.1: Imagen del VLA hacia las regiones HII M42 y M43 a 330 MHz (Subrahmanyan 1992). Los contornos son $32 \times (-1, 1, 2, 4, 8, 16, 24, 32, 48, 56, 62, 65, 68)$ mJy beam^{-1}. El area a potencia media del haz es 57×57 arcsec^2 y está indicado en la esquina inferior izquierda.

libre debido a que es emitida cuando los electrones libres (no ligados) son desviados por los protones al interactuar a través de su carga. Debido a que son partículas libres sus estados no están cuantizados y la emisión libre-libre muestra un espectro continuo. La emisión de continuo de una región HII también incluye la emisión térmica de las partículas de polvo que son calentadas por la radiación estelar. La emisión del polvo es similar a la emisión de cuerpo negro y puede ser más intensa que la emisión libre-libre, pero debido a que su temperatura efectiva es ~ 100 K, su pico de emisión se da en la parte infrarroja del espectro.

Además de la emisión libre-libre, el gas ionizado puede emitir líneas de recombinación (RRLs). Las RRLs son producidas cuando los electrones han perdido suficiente energía, de tal manera que estos ya se encuentran ligados a los protones, siendo entonces capaces de emitir solamente radiación cuantizada. Los electrones pueden permanecer solo un tiempo finito de vida en cada estado cuantizado por lo que van decayendo de estado de energía emitiendo las RRLs espontáneamente y de manera estimulada por la radiación de continuo (Shaver 1964). El radiocontinuo provee información sobre la tasa de fotones ionizantes emitidos por la estrella y las líneas espectrales en radio proveeen información sobre la
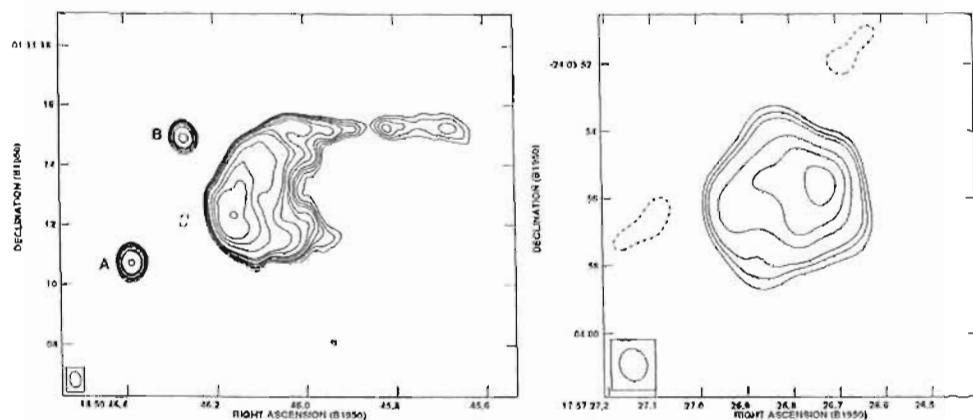
Figura 1.2: Morfología de dos regiones HII. (a) Región cometaria G34.3+0.15 y (b) región con estructura de cascara G5.89-0.24.

estructura de velocidad, temperatura y densidad electrónica de las regiones HII.

En nuestra Galaxia las regiones HII se encuentran localizadas principalmente en los brazos espirales, mismos que se encuentran en el plano galáctico y se extienden varios kiloparsecs desde el centro. En las galaxias con brote de formación estelar, la mayoría de las regiones HII se encuentran concentradas en las partes centrales de este tipo de galaxias.

1.3   Radiocontinuo y líneas de recombinación en radio

Desde las primeras detecciones de las RRL hacia regiones de gas ionizado en nuestra galaxia (Sorochenko & Borodzich, 1965), las RRL se han vuelto una herramienta muy poderosa para poder distinguir entre las fuentes térmicas y las no térmicas, para poder estudiar las regiones de formación estelar, para investigar el medio interestelar difuso, así como para explorar la estructura galáctica. En un inicio las observaciones de las RRL hacia regiones HII se hacia con telescopios de un solo plato, con lo cual los estudios detallados sobre variaciones en la estructura de las regiones de gas ionizado no eran posibles. En la mayoría de los casos el haz del telescopio era a lo mucho comparable con el tamaño de las regiones observadas, con la excepción de la nebulosa de Orión. La construcción de radio-interferómetros con receptores muy estables y muy sensitivos, como el WSRT y el VLA, hicieron posible estudiar las regiones HII con alta resolución angular (van Gorkom et al. 1980).

Hay un gran número de transiciones de líneas de recombinación que pueden ser observadas, el rango de frecuencias sobre el cual se detectan es muy amplio: desde el óptico

hasta el radio. Debido al rango tan amplio de frecuencias en el que pueden ser observadas las líneas de recombinación, estas pueden ser usadas para estudiar objetos que tienen propiedades físicas muy diferentes. De las líneas de recombinación más conocidas se encuentran las $H\alpha$ y $H\beta$, las cuales se observan en longitudes de onda visibles. Estas líneas surgen debido a transiciones electrónicas entre estados cuánticos bajos, en particular $H\alpha$ ocurre entre n=3 y n=2 y $H\beta$ entre n=4 y n=2.

Las observaciones de RRL juegan un papel muy importante para estudiar regiones en las que el oscurecimiento por polvo, en el óptico o infrarrojo cercano, es muy importante. Las RRL se observan cuando ocurren transiciones electrónicas entre estados cuánticos n$\geq$ 40. El espectro de emisión de las RRL, para cualquier especie de átomos, es de tipo hidrogénico y está dado por:

$$v = Z^2 R_X c \left(\frac{1}{n^2} - \frac{1}{(n + \Delta n)^2} \right) \tag{1.2}$$

donde v es la frecuencia asociada a la transición (n+Δn)$\rightarrow$ n, Z es la carga nuclear de la especie de ion X, c es la velocidad de luz, R_X es la constante de Rydberg para la especie X. Esta transición del número cuántico $(n + \Delta n) \rightarrow n$ de la especie X se denota como Xnα (Δn= 1), Xnβ (Δn= 2), etc.

Se puede obtener mucha información sobre las regiones HII usando el radiocontinuo y las RRL. Para determinar los parématros físicos del gas ionizado, se necesita calcular la intensidad teórica del radiocontinuo y de las RRL usando la ecuación de transporte radiativo. Para la emisión de radiocontinuo se usan los coeficientes de emisión y absorción en el continuo, κ_C y j_C, en la ecuación de transporte radiativo:

$$-\frac{dI_C}{ds} = \kappa_C I_C - j_C, \tag{1.3}$$

en esta ecuación I_C es la intensidad específica de la radiación de continuo de la nube de gas ionizado. La razón j_C/κ_C es llamada la función fuente y en el caso de que exista equilibrio termodinámico esta está dada por la función de Planck $B(T, v)$ a través de la relación de Kirchoff. La función de Planck en longitudes de onda de radio ($hv \ll kT$) está dada por la aproximación de Rayleigh-Jeans: $B(T, v) \simeq \frac{2v^2 kT}{c^2}$. En el caso de una nube isotérmica de gas ionizado que sostiene un ángulo sólido Ω, suponiendo una fuente de fondo con densidad de flujo S_o, la solución a la ecuación de transporte radiativo predice una densidad de flujo

de continuo S_c dada por:

$$S_c = S_u e^{-\tau_c} + \Omega \frac{2kT_e \nu^2}{c^2}(1 - e^{-\tau_c}). \tag{1.4}$$

La profundidad óptica de la emisión libre-libre, τ_c, está dada por:

$$\tau_c = \int_0^L \kappa_c ds \simeq 8.235 \times 10^{-2} \left(\frac{n_e}{cm^{-3}}\right)^2 \left(\frac{L}{pc}\right)\left(\frac{T_c}{K}\right)^{-1.35} \left(\frac{\nu}{GHz}\right)^{-2.1}. \tag{1.5}$$

en donde n_e es la densidad electrónica y L es el tamaño de la nebulosa a lo largo de la línea de visión. A partir de la Ec. 1.4 se pueden obtener dos aproximaciones despreciando la fuente de fondo S_u. Para altas frecuencias el gas ionizado es ópticamente delgado, i.e. $\tau_c \ll 1$, lo que resulta en

$$S_c \simeq \Omega \frac{2kT_c \nu^2 \tau_c}{c^2} \propto \nu^{-0.1}, \tag{1.6}$$

y para bajas frecuencias el gas es ópticamente grueso, i.e. $\tau_c \gg 1$ y tenemos que

$$S_c \simeq \Omega \frac{2kT_e \nu^2}{c^2} \propto \nu^2. \tag{1.7}$$

Si se identifica la frecuencia a la que $\tau_c = 1$ y se determina la temperatura electrónica, se puede estimar lo que es conocido como medida de emisión, ME. La medida de emisión está definida por $\int_0^L n_e^2 ds$. A través de la ME se puede cuantificar la masa de la nebulosa que emite la radiación libre-libre. Aunque esta técnica funciona de manera adecuada para determinar las propiedades físicas promedio de una región HII, se debe tener en cuenta que las regiones HII son inhomogeneas y existen gradientes de velocidad y temperatura que deben ser determinados usando observaciones de alta resolución angular.

Las RRLs del hidrógeno proveen el método más sencillo y más preciso para determinar la temperatura electrónica (T_e) de las regiones HII. Para esto, como se hizo para la emisión libre-libre, se plantea una ecuación de transporte radiativo usando los coeficientes de absorción y emisión para la línea en equilibrio termodinámico local (LTE) κ_L^* y j_L^*. La profundidad óptica de la línea en LTE, τ_L^*, esta definida por

$$\tau_L^* = 2.33 \times 10^4 \left(\frac{\Delta\nu_L}{kHz}\right)^{-1} \left(\frac{\nu_L}{GHz}\right)^{2.1} \left(\frac{T_e}{K}\right)^{-1.15} \tau_c, \tag{1.8}$$

donde $\Delta\nu_L$ es el ancho de la línea y ν_L la frecuencia de la RRL. Usando la aproximación de

Rayleigh-Jeans, se tiene que la densidad de flujo en la RRL de la región HII en LTE es:

$$S_L = S - S_c = \Omega \frac{2kT_e \nu^2}{c^2} \left[1 - e^{-(\tau_c + \tau_L^*)} - (1 - e^{-\tau_c}) \right] + S_o e^{-\tau_c}(e^{-\tau_L^*} - 1). \qquad (1.9)$$

En el caso de LTE para gas ópticamente delgado ($1 \gg \tau_c \gg \tau_L^*$) y despreciando la emisión de cualquier fuente de fondo, la razón de línea a continuo es:

$$\frac{S_L}{S_c} = \frac{\tau_L^*}{\tau_c} = 6.985 \times 10^3 \left(\frac{\Delta V}{km \ s^{-1}} \right)^{-1} \left[\frac{\nu}{GHz} \right]^{1.1} \left[\frac{T_e}{K} \right]^{-1.15} \frac{1}{1 + N(He+)/N(H+)}, \qquad (1.10)$$

la cual nos permite estimar directamente la temperatura electrónica.

1.3.1 Desviaciones de LTE

Para considerar las desviaciones de LTE, se introducen los coeficientes de absorción $\kappa_l(\nu)$ y de emisión $j_l(\nu)$, así como la profundidad optica de la RRL fuera de LTE:

$$\kappa_l(\nu) = b_n \beta_n \kappa_l^*(\nu), \qquad (1.11)$$

$$j_l(\nu) = b_n j_l^*(\nu), \qquad \cdot \qquad (1.12)$$

$$\tau_L = \tau_L^* b_n \beta_n, \qquad (1.13)$$

los cuales dependen de los coeficientes de desviación de LTE b_n y β_n, que para un nivel de energía n dado, con población N_n^* en LTE, población real N_n y una energía E_n de ese nivel se definen como:

$$b_n = \frac{N_n}{N_n^*} \qquad (1.14)$$

$$\beta_n = 1 - kT_e \frac{d(ln(b_n))}{dE_n}. \qquad (1.15)$$

La función fuente para la RRL fuera de LTE se puede escribir como

$$S_{fuente} = \frac{j_c + j_L}{\kappa_c + \kappa_L}, \qquad (1.16)$$

por lo que la densidad de flujo de la RRL de una región HII fuera de LTE, con fuente de emisión de fondo es:

$$S_L = S - S_c = \Omega \frac{2kT_e \nu^2}{c^2} \left(\frac{\tau_c + b_n \tau_l^*}{\tau_c + \tau_L} \right) \left[1 - e^{-(\tau_c + \tau_L)} - (1 - e^{-\tau_c}) \right] + S_o e^{-\tau_c}(e^{-\tau_L} - 1). \qquad (1.17)$$

La razón de línea a continuo tomando en cuenta la desviaciones de LTE, en el caso opticamente delgado y sin fuentes de fondo se reduce a:

$$\frac{S_L}{S_c} = \frac{\tau_L^*}{\tau_c}\left[b_n\left(1 - \frac{\beta_n\tau_c}{2}\right)\right]. \tag{1.18}$$

1.3.2   Ensanchamiento de las RRLs.

Existen diferentes mecanismos por los que las RRLs se ensanchan y se describen a continuación:

Ensanchamiento natural. Es una propiedad intrínseca del átomo que resulta de la longitud finita del tren de onda emitido y la variación de su amplitud sobre el periodo de emisión. Este ensanchamiento tiene un perfil Lorentziano que va como:

$$\phi_G(\nu) = \frac{\Gamma/\pi}{\pi\left|4(\nu - nu_o)^2 + (\frac{\Gamma}{2\pi})^2\right|}, \tag{1.19}$$

en donde Γ es la constante de amortiguamiento, que es la suma de las constantes de amortiguamiento dadas para el nivel cuántico inferior y superior n_1 y n_2, respectivamente y está dada por:

$$\Gamma = \Gamma_{n_1} + \Gamma_{n_2} = \sum_{n_1=1}^{n_2-1} A_{n_2,n_1} + \sum_{n_0=1}^{n_1-1} A_{n_1,n_0}, \tag{1.20}$$

aquí A_{n_2,n_1} y A_{n_1,n_0} son las constantes de Einstein para el decaimiento espontáneo. La magnitud de este ancho natural es del orden de $\sim 10^{-4}$ km s^{-1}.

Ensanchamiento Doppler. Este ensanchamiento está determinado por la distribución de velocidades de Maxwell-Boltzmann si la turbulencia a gran escala no es considerada. El perfil de línea $\phi_G(\nu)$ es una Gaussiana con un ensanchamiento Doppler dado por:

$$\phi_G(\nu) = \left(\frac{4\ln 2}{\pi}\right)^{1/2}\frac{1}{\Delta\nu_G}exp\left[-4\ln 2\left(\frac{\nu_o - \nu}{\Delta\nu_G}\right)^2\right], \tag{1.21}$$

en donde $\Delta\nu_G$ es el ancho a potencia media (FWHM) de la línea ensanchada térmicamente y ν_n es la frecuencia en reposo de la línea en Hz. La línea ensanchada térmicamente se refiere a una equipartición de energía entre los tres grados de libertad para las partículas que tienen asociada una temperatura.

El ancho Doppler de RRLs es más ancho que el ancho natural de la línea. Si se toma en cuenta la microturbulencia, generada por celdas de gas que se mueven unas con respecto a otras, el ancho Doppler ΔV_G es:

$$\Delta V_G = (4 \ln 2)^{1/2} \sqrt{\frac{2kT}{M} + V_T^2} \qquad (1.22)$$

en donde ΔV_G es el ancho de la línea por la dispersión de velocidades dada por la ecuación de Maxwell-Boltzmann y V_T es el ancho de la línea debido a la microturbulencia. M es la masa de los átomos de una especie dada, T la temperatura y k es la constante de Boltzmann.

Ensanchamiento Stark y/o ensanchamiento por presión electrónica. Estos tipos de ensanchamiento son los más importantes para las RRL cuando se trata de gas de alta densidad y las líneas provienen de números cuánticos grandes. El ensanchamiento Stark consiste en el desdoblamiento y desplazamiento de los niveles de energía atómicos por la superposición de campos eléctricos externos que varían en el tiempo debido a la perturbación por electrones libres cercanos. El efecto de los campos eléctricos que varían en el tiempo sobre el tren de onda emitido produce una variación abrupta en la fase de la onda. Este ensanchamiento depende esencialmente de la densidad del gas y su perfil de línea es Lorentziano dado por

$$\phi(\nu) = \frac{2\Delta\nu_L}{\pi[4(\nu - \nu_a)^2 + \Delta\nu_L^2]}, \qquad (1.23)$$

en donde $\Delta\nu_L$ es el ancho a potencia media de la línea. El ensanchamiento por presión da como resultado un perfil de Lorentz y se debe al efecto de choques entre partículas elementales, dando lugar a una alteración de sus velocidades proyectadas.

Los diferentes mecanismos mencionados como responsables del ensanchamiento de la línea da como resultado el llamado perfil de Voigt, que es la convolución de los diferentes perfiles de línea antes mencionados, y toma la forma

$$\phi(\nu) = \left(\frac{4 \ln 2}{\pi}\right)^{1/2} \frac{1}{\Delta\nu_G} H(a, y), \qquad (1.24)$$

en donde "a" es un parámetro de la mezcla de los perfiles Gaussiano y Lorentziano,

$$a = \frac{\sqrt{\ln 2}\Delta\nu_L}{\Delta\nu_G}, \qquad (1.25)$$

el parámetro "y" toma en cuenta la distancia desde el centro de la línea,

$$y = \frac{\sqrt{4 \ln 2}(v - v_o)}{\Delta v_G}, \tag{1.26}$$

y la función $H(a, y)$ está dada por,

$$H(a, y) \equiv \frac{a}{\pi} \int_{-\infty}^{\infty} \frac{e^{-t^2}}{a^2 + (y - t)^2} dt. \tag{1.27}$$

1.4   Razón de línea a continuo y temperatura electrónica

Uno de los parámetros físicos más importantes que puede ser determinado es la temperatura electrónica, Te. La T_e es el parámetro que determina la población de los números cuánticos principales del átomo además del grado de ionización. La dependencia con la temperatura de cada población, las que corresponden a los estados cuánticos ligados y los no ligados, es diferente. Esta dependencia diferente con la T_e nos permite determinar la temperatura electrónica usando la razón entre la densidad de flujo de la línea de recombinación y la densidad de flujo del continuo (S_L/S_C). En la Figura 1.3 se muestran valores observados de S_L/S_C para diferentes RRL observadas hacia NGC 1976 (mejor conocida como la nebulosa de Orión). En esta figura se muestran también los valores teóricos de la razón S_L/S_C en el caso de LTE para gas ionizado a 8500 K, suponiendo una componente debida a turbulencia de $V_T = 10$ km s^{-1}.

Sin embargo, existen varios efectos que dificultan la determinación de T_e usando RRL. Existen desviaciones del LTE al poblar los diferentes niveles cuánticos del hidrógeno. A frecuencias muy altas la desviación de equilibrio termodinámico hace que el número de átomos que pueden emitir decrezca, disminuyendo así la emisión de la RRL por debajo de los valores de LTE. A altas frecuencias también se tiene que la contribución del polvo a la radiación del continuo comienza a ser importante. Esta emisión del polvo incrementa la emisión total de continuo, teniendo ya no solamente la emisión libre-libre. Estos dos efectos, presentes a altas frecuencias, disminuyen el valor de la razon de S_L/S_C dejandolo por debajo de valores de LTE. En la Figura 1.3 se ilustra como estas desviaciones de LTE influyen para frecuencias > 40 GHz.

El segundo efecto es que se subestima la energía radiada en la línea debido al ensanchamiento por presión, (y también el efecto Stark), que re-distribuye la emisión desde el centro de la línea hacia las alas, en donde se mezcla con la emisión de continuo. Al subesti-
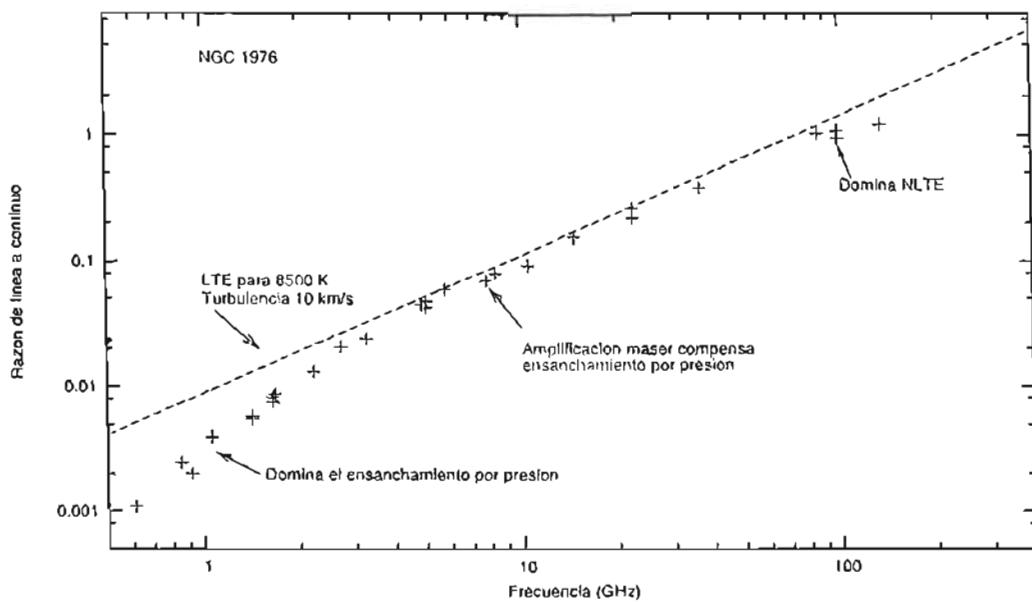
Figura 1.3: Razón de línea a continuo observada (cruces) para RRL Hnα en NGC 1976 y valores en LTE (línea) para una temperatura electrónica de 8500 K en función de la frecuencia. Los datos fueron tomados de Lockman & Brown (1975), Gordon (1989) y Gordon & Walmsley (1990).

mar la emisión pico de la línea se sobre-estima T_e. El efecto debido al ensanchamiento por presión es reducido a ciertas frecuencias en las que la emisión maser compensa el efecto Stark al aumentar la densidad de flujo máxima de la línea. Otro problema que está presente a frecuencias bajas es que la opacidad de la emisión libre-libre puede ser importante. La razón S_L/S_C observada corresponde a regiones con $\tau_C < 1$. Así, debido a las variaciones de la densidad dentro de las regiones HII, los valores observados de S_L/S_C reflejarán las propiedades físicas de regiones con gas más tenue con $\tau_C < 1$. El efecto del ensanchamiento por presión se hace más notable para frecuencias < 6 GHz (ver Figura 1.3).

Sin embargo, a frecuencias intermedias $\sim 10-40$ GHz si es posible medir la T_e de manera más exacta. Esta ventaja del rango de frecuencias intermedias sobre frecuencias muy bajas o muy altas es debida al efecto parcial de maser que compensa el efecto Stark. Por otro lado, debido a que el gas está distribuido de manera inhomogénea, es mejor observar a la frecuencia más alta posible para reducir el efecto de la opacidad del continuo sin ser afectados por las desviaciones de LTE y emisión de continuo por polvo. La manera directa de estimar T_e a partir del cociente S_L/S_C es usando la Ec. 1.10.

1.5   Galaxias con brote de formación estelar

Una galaxia con brote de formación estelar es aquella en la cual el fenómeno de formación estelar ocurre de una manera muy eficiente. Mientras que la SFR estimada para toda nuestra galaxia (en un diámetro de ~ 60 kpc) es de ~ 1 $M_\odot$/año, en las galaxias con brote de formación estelar esta tasa es $\gtrsim 3$ $M_\odot$/año y ocurre en regiones más pequeñas (diámetro de ~ 1 kpc). En casos extremos se han estimado SFRs tan grandes como 1000 $M_\odot$/año. En tales sistemas la luminosidad bolométrica es esencialmente dominada por la luminosidad IR, entre mayor sea la luminosidad en el FIR más intenso será el brote de formación estelar. Sin embargo, se debe notar que una alta luminosidad en el FIR no es suficiente para describir una galaxia como con brote de formación estelar. Las dos condiciones anteriores, alta luminosidad en el FIR y alta tasa de formación estelar, usualmente implican que la formación estelar asociada al brote de formación estelar domina sobre la formación estelar de fondo (la que no está asociada con el brote de formación estelar) en casi todas las longitudes de onda. En la región en donde se da el brote de formación estelar el gas se consume sobre una escala de tiempo mucho más pequeña que la vida de la galaxia. El tiempo de consumo del gas, que determina la eficiencia del brote de formación estelar, esta dado por $t_d = M_{gas}/SFR$. Ya que la SFR es función del tiempo, se define un tiempo característico para el periodo del brote de formación estelar como $t_d = M_{gas}/SFR_{cte}$, donde SFR_{cte} es una SFR constante. Para galaxias con brote de formación estelar, el tiempo de consumo de gas debido a la formación estelar puede ser tan corto como $10^7 - 10^8$ años, mientras que para nuestra galaxia, es de $\sim 10^9 - 10^{10}$ años.

Las galaxias con brote de formación estelar fueron identificadas en un inicio por su exceso de emisión infrarroja (IR) por lo que fueron clasificadas como "Galaxias Infrarrojas" (Low & Kleinmann, 1968; Kleinmann & Low, 1970 a, b). La luminosidad en longitudes de onda infrarrojas es comparable, si no es que mayor, a su luminosidad en el óptico. A partir de observaciones de las galaxias NGC 253 y M82 (Rieke et al. 1980) se demostró que el exceso de emisión en el IR se debe a la emisión térmica del polvo predominantemente calentado por emisión estelar. Los espectros ópticos de galaxias con brote estelar se caracterizan por tener fuertes líneas de emisión de hidrógeno y otros elementos ionizados. Estas líneas son creadas en las envolventes gaseosas de estrellas tipo OB de las cuales hay miles en una región muy pequeña. Ciertamente, el espectro óptico e infrarrojo de una galaxia con brote de formación estelar es muy similar al de las regiones HII galácticas. De la tasa de formación estelar, calculada del tamaño de la región que contiene al polvo que emite en el

infrarrojo y de la cantidad de gas en esa región, se obtiene que, a la tasa de formación este-
lar presente, todo el gas será consumido en un tiempo muy corto ($\sim 10^7 - 10^8$ años). La tasa
de formación estelar (definida como la masa de estrellas, en determinado rango, formadas
por unidad de tiempo (usualmente medida en $M_\odot$ por año), necesita ser mucho mayor que
en otras galaxias normales (Harwit & Pacine 1975). Por lo tanto, se concluyó que esta alta
tasa de formación estelar es un fenómeno que dura poco tiempo (comparado con la vida de
la galaxia), denominándose a estas galaxias como galaxias con brote de formación estelar
(Wedman et al. 1981). El corto tiempo de vida de este fenómeno implica un mecanismo
que lo inicie y posiblemente, otro mecanismo que lo detenga. Se han encontrado sistemas
con formación estelar que inició hace $3 - 6 \times 10^6$ años, consistente con la duración de
este fenómeno en galaxias. Este mecanismo también se vió que puede explicar las galaxias
con exceso al azul. De manera general, una galaxia azul es aquella que tiene una contribu-
ción significante de objetos calientes y masivos confirmando que están formando estrellas
de manera activa. El telescopio espacial IRAS revolucionó este tema al descubrir miles de
galaxias con exceso infrarrojo que de otra manera hubieran sido clasificadas como normales
debido a sus características en el óptico.

La dependencia de la SFR con el tiempo en regiones con brote de formación estelar
no es bien conocida. Se han derivado SFR instantáneas, constantes, así como exponencial-
mente decrecientes para diferentes galaxias. Se ha mostrado que la tasa de formación es
proporcional a la luminosidad en el FIR. La eficiencia de formación estelar (SFE) es pro-
porcional a la SFR por unidad de masa de gas, y está definida como L_{IFR}/M_{H2}. El valor de
SFE varía desde 2 $L_\odot/M_\odot$ para galaxias normales hasta alrededor de 200 $L_\odot/M_\odot$ para brotes
de formación estelar extremos. La SFE puede ser expresada también como la razón entre la
masa estelar que participa en el brote de formación estelar y la masa de gas. Esta razón es
< 5 % para galaxias normales, pero puede ser tan alto como 50 % para brotes de formación
estelar.

Ya que las galaxias con brote de formación estelar tienen una tasa de formación estelar
alta, también consisten de un gran número de estrellas OB, las cuales dominan el continuo
en el óptico y la emisión de línea. Por lo tanto una fracción grande de galaxias en los catálo-
gos Markarianos y Byurakiano son brotes de formación estelar. Las galaxias con brote de
formación estelar tienen grandes cantidades de gas molecular y por lo tanto polvo asocia-
do. Este polvo absorbe la radiación UV de las estrellas OB y es calentado a temperaturas
de 30-80 K. El polvo entonces re-emite térmicamente en el infrarrojo, con un máximo de
emisión en la región entre $60 - 100\ \mu$m del FIR. La reserva de gas molecular también da

lugar a fuertes líneas moleculares en el mm y en el sub-mm. Las estrellas OB ionizan el gas alrededor de ellas, formando regiones HII, las cuales emiten líneas nebulares en el óptico y en el IR y también emisión libre-libre en la banda de radio. Además, el gas ionizado emite líneas de recombinación en el radio. Sin embargo, la emisión de radiocontinuo aparece dominada por emisión sincrotrón no-térmica de los electrones relativistas acelerados por choques en las SNR. Ya que en una galaxia con brote de formación estelar el número de estrellas con masa > 8 $M_\odot$ es grande y por lo tanto la tasa de supernovas también es grande, la emisión de radio será mayor comparada con galaxias normales. Se sabe que la emisión de radiocontinuo y la de FIR están fuertemente correlacionadas para todas las galaxias con formación estelar, incluyendo las galaxias con brote de formación estelar.

1.5.1 Mecanismo de activación de los brotes de formación estelar

Se sabe que la tasa de formación estelar es proporcional a la densidad superficial del gas, lo cual se refiere como la ley de Schmidt (Schmidt 1959; Kennicutt 1998). Ya que la SFR para las galaxias con brote de formación estelar es mayor que lo normal, entonces estas galaxias tienen también alta densidad de gas molecular, esto es de hecho lo que se observa. Ya que la fase activa del brote de formación estelar es un fenómeno relativamente corto que requiere una densidad de gas mayor que el promedio, se requiere un mecanismo que pueda concentrar el gas de manera eficiente en una pequeña región. La concentración del gas ocurrirá bajo la influencia de torcas externas. Las torcas pueden ser producidas por un potencial no axi-simétrico, las fuentes para esto son las barras, interacción galaxia-galaxia o fusión de galaxias. Se ha establecido a través de observaciones que para los sistemas interactuantes, la fracción de galaxias con brote de formación estelar es mucho mayor que entre las galaxias solitarias sin barra no interactuando. También, entre más fuerte es la interacción, más intenso es el brote de formación estelar en esa galaxia. Sin embargo, un mecanismo para concentrar el gas en una pequeña región no es suficiente. Cualquier mecanismo de este tipo debe ser capaz de hacer eso en escalas de tiempo corto. La formación estelar se conoce que es un proceso altamente regulado con retroalimentación negativa que es provista por una variedad de procesos. El más importante de estos (en parte porque tiene una escala de tiempo más corta que otros procesos) es la ionización del gas alrededor de estrellas OB recién formadas, por lo tanto previniendo que este gas forme más estrellas. La escala asociada es de unos millones de años, lo que lleva a la SFE observada en galaxias normales de 1-5 %. Entonces, en una galaxia con brote de formación estelar, la mayoría de

la formación estelar, y por lo tanto la concentración de gas en una pequeña región, debe ocurrir en escalas de tiempo más cortas que esto.

1.5.2 Relación entre la emisión en IR y la presencia del brote de formación estelar.

Las galaxias con brote de formación estelar son brillantes en el IR, y por lo tanto se encuentran en el catálogo IRAS. Sin embargo, lo inverso no es verdad, i.e. no todas las galaxias IRAS son necesariamente galaxias con brote de formación estelar. La luminosidad en el IR puede tener contribuciones debido a la emisión de polvo de los discos con formación estelar a gran escala, que no necesariamente contienen un brote de formación estelar. También puede tener contribuciones significativas de "grumos" de polvo, calentado por estrellas evolucionadas, y también de polvo calentado por un AGN central. Debido a la baja resolución de IRAS, identificar entre las diferentes fuentes de emisión en IR, basados solo en el flujo total de IRAS, es difícil. Sin embargo, ha sido establecido que entre mayor es la luminosidad en el FIR, mayor es la probabilidad de que la galaxia tenga un brote de formación estelar. La luminosidad FIR observada varía de 10^6 $L_\odot$ (en galaxias normales como nuestra Galaxia) a $> 10^{12}$ $L_\odot$ (en brotes de formación estelar extremos). Las galaxias con brotes de formación estelar muy intensos son clasificadas como Galaxias Luminosas en Infrarrojo o LIGs ($L_{FIR} > 10^{11}$ $L_\odot$) y galaxias ultraluminosas en el infrarrojo o ULIGs (LFIR$> 10^{12}$ $L_\odot$) y casi todas las galaxias con $L_{FIR} > 10^{11}$ $L_\odot$ se observa que son galaxias con brote de formación estelar. Entre las galaxias cuya luminosidad bolométrica es mayor que 10^{12} $L_\odot$, las ULIGs constituyen las poblaciones dominantes, comparables en densidad espacial a los cuásares seleccionados en el óptico. La fracción de galaxias en fusión incrementa con la luminosidad en el FIR, de 5 % para $10^9 L_\odot < L_{FIR} < 10^{10}$ $L_\odot$ y 50 % para $10^{10} L_\odot < L_{FIR} < 10^{12}$ $L_\odot$ hasta 100 % para $L_{FIR} > 10^{12}$ $L_\odot$. Entonces todos los brotes de formación estelar intensos parecen ocurrir en fusiones de galaxias, pero también es conocido que no todas las galaxias en fusión de igual intensidad resultan en un brote de formación estelar. A pesar de que un alto valor de la luminosidad en el FIR no implica, en principio, un brote de formación estelar, la razón de su luminosidad a la luminosidad en el óptico, L_{FIR}/L_B, es un buen indicador de un brote de formación estelar. Esta razón es alrededor de 0.1 para galaxias normales, > 10 para brote de formación estelar con luminosidad moderada, y > 100 para ULIGs.

Para poder entender la evolución de las galaxias es muy importante estudiar la historia de la formación estelar. Las observaciones de galaxias de campo sugieren un incremento

en la formación estelar a corrimientos al rojo z≈ 1.5. En el universo cercano las galaxias con tasas de formación estelar altas son relativamente comunes. Muchas de las galaxias con brote de formación estelar han sufrido de interacciones con galaxias cercanas. Se piensa que la interacción entre galaxias ayuda a que el gas sea concentrado en sus centros, creando las condiciones necesarias para que se den los brotes de formación estelar.

1.5.3   RRL hacia galaxias con brote de formación estelar

Las primeras detecciones de líneas de recombinación en radio se hicieron hacia la galaxia con brote de formación estelar M82 (Shaver et al. 1977, Bell & Seaquist 1977, Chaisson & Rodríguez 1977), localizada a ~ 3 Mpc de nosotros. Shaver et al. (1977) propusieron que el principal mecanismo de emisión de las RRL extragalácticas es la estimulación de las líneas debido al continuo no térmico presente hacia las galaxias con brote de formación estelar. Shaver et al. (1978) observaron hacia M82 diferentes RRL, en el rango de frecuencias $1.4 - 15$ GHz, y determinaron que las RRL hacia M82 son observadas principalmente debido a que estas líneas son amplificadas por el continuo no térmico de fondo.

Por otro lado, Seaquist & Bell (1977) realizaron observaciones de RRL hacia la galaxia con brote de formación estelar NGC 253, localizada a una distancia similar a la de M82 (~ 3 Mpc). A partir de las observaciones de la línea H102α, Seaquist & Bell (1977) determinaron que el mecanismo de emisión de las RRL hacia NGC 253 es principalmente debido a emisión espontánea. De acuerdo a calculos de la intensidad teórica de las RRL emitidas de manera espontánea, las RRL pueden ser observadas para objetos localizados a distancias < 10 Mpc. Sin embargo, si las RRL son emitidas de manera estimulada, por fuentes no térmicas de fondo, entonces se pueden observar objetos más lejanos (Shaver 1978). Shaver propuso que la mejor ventana para observar las RRL es entre 1 y 10 GHz, sin embargo solamente se detectaron RRL hacia un número limitado de galaxias.

Las primeras observaciones fueron realizadas con radiotelescopios de plato sencillo. Posteriormente, las observaciones de RRL extragalácticas con el VLA a ~ 8 GHz motivaron más observaciones de RRL a frecuencias similares (Anantharamaiah et al. 1993; Zhao et al. 1996; Mohan et al. 2002) y a frecuencias mayores (Puxley et al. 1991; Zhao et al. 2000; Anantharamaiah et al. 2000), hacia galaxias con brote de formación estelar.

El estudio de estos brotes de formación estelar usando líneas de recombinación en radio con alta resolución angular nos permite conocer en detalle las condiciones físicas y cinemáticas del gas que da origen a estos brotes de formación estelar en galaxias. En esta

tesis hemos implementado un método que reduce las incertidumbres al sobreponer varias ventanas espectrales cuando se observan líneas de recombinación en el milimétrico hacia galaxias con brote de formación estelar que se describe en el apéndice A.

Capítulo 2

Radio Continuum and H92α Recombination Line Observations of G34.26+0.15 and G5.89-0.39

Rodríguez-Rico, C. A., Rodríguez, L. F., & Gómez, Y.,

Resumen

Las dos regiones HII estudiadas en este capítulo muestran diferentes morfologías, lo cual puede deberse al medio interestelar en que se encuentran embebidas. Estudiar la relación entre estas regiones HII y su medio ambiente es la principal motivación para analizar observaciones de RRL. Se analiza la estructura de velocidad, usando la RRL H92α, de las regiones HII: G34.26+0.15 que tiene una morfología cometaria (Reid & Ho 1985) y G5.89-0.39 que tiene morfología de cascara con lóbulos bipolares (Zijlstra et al. 1990; Gómez

et al. 1991). Ambas regiones HII tienen anchos inusuales en sus líneas de recombinación
($\geq$ 50 km s^{-1}), los cuales no pueden explicarse por ensanchamiento térmico mas movimientos turbulentos. Estas dos regiones tienen emisión maser de OH y H_2O asociada, lo cual sugiere que son regiones de formación estelar joven.

G34.26+0.15 es una región HII estudiada en varias longitudes de onda, en radiocontinuo (Turner et al. 1974; Reid & Ho 1985; Wood & Churchwell 1989), RRLs (Garay et al. 1985;Garay, Rodríguez, & Van Gorkom 1986; Gaume et al. 1994; Fey et al. 1994) y líneas moleculares (Benzon & Johnston 1984; Heaton et al. 1985; Anderson & Garay 1986; Gaume & Mutel 1987; Keto, Ho, & Reid 1987; Garay & Rodríguez 1990; Carral & Welch 1992; Watt & Mundy 1999; Gómez et al. 2000). Las observaciones de radiocontinuo muestran una región HII cometaria ultracompacta (UC) con extención de $\sim$ 4$''$ y dos regiones HII UC al este de la cometaria, cada una con tamaño angular de $\sim$ 1$''$, y una región HII extendida con morforlogía de anillo. La región cometaria parece ser excitada por una estrella O7 ZAMS, si se supone una distancia de 3.3 kpc (Kuchar & Bania 1994). Las observaciones de la RRL H76α revelaron un gradiente de velocidad, en la dirección norte-sur a lo largo de la región HII cometaria, de $\sim$ 16 km s^{-1} arcsec^{-1}, interpretado como gas ionizado que rota perpendicular al eje de simetría de la región cometaria (Garay et al. 1986; Gaume et al. 1994). El gas molecular también muestra un gradiente de velocidad de $\sim$ 15 km s^{-1} arcsec^{-1} a lo largo de $\sim$ 0.2 pc (Carral & Welch; Akeson & Carlstrom 1996; Gómez et al. 2000) pero en sentido opuesto al gradiente de velocidad del gas ionizado.

G5.89-0.39 (conocida también como W28 A2) ha sido estudiada en longitudes de onda de radio e IR. La emisión de radiocontinuo hacia esta fuente es ópticamente gruesa para longitudes de onda >1.3 cm (Gómez et al. 1991). La region HII puede estar excitada por al menos una estrella O6 ZAMS, suponiendo una distancia de 2.6 kpc (Downes et al. 1980). G5.89-0.39 tiene uno de los flujos moleculares mas poderosos y masivos observados en la Galaxia (Harvey & Forveille 1988; Cesaroni et al. 1991; Zijlstra et al. 1990; Acord et al. 1997). El radiocontinuo muestra un núcleo con morfología de cáscara con un diametro de $\sim$ 4$''$ y lóbulos bipolares débiles en la direccion noroeste-sureste (Gómez et al. 1991). La orientación del flujo molecular permanece incierto y no ha sido posible hacer una comparación confiable entre los flujos moleculares y de gas ionizado. Sin embargo, el gas de alta velocidad trazado por ambos el CS (Cesaroni et al. 1991) y por los maseres de H_2O (Hofner & Churchwell 1996) sugieren una orientación similar a la observada en los lóbulos bipolares de radiocontinuo.

En este capítulo reportamos observaciones de radiocontinuo a 8.3 GHz y de la RRL

H92α hechas con el VLA hacia las regiones de formación estelar G34.26+0.15 y G5.89-0.39. Ambas regiones tienen una opacidad promedio considerable ($\tau_c \simeq 2$) en el radiocontinuo a 8.3 GHz y la línea H92α se utiliza para estudiar las variaciones de opacidad como función de la posición. Detectamos emisión de la linea H92α en la componente ultracompacta A en G34.26+0.15, pero no en la componente ultracompacta B. Este resultado es intrigante porque ambas componentes ultracompactas son similares en densidad de flujo en el continuo y en tamaño angular. La observación de la RRL H92α hacia la componente A puede explicarse si esta tiene una cáscara ópticamente delgada, de donde proviene la emisión de RRL H92α, que la envuelve. Si bien G5.89-0.39 muestra gradientes pronunciados de velocidad en la linea H92α, estos no pueden explicarse solamente con rotación, como se ha propuesto anteriormente.

Abstract

We report VLA observations of 8.3 GHz continuum and H92α radio recombination line toward the star forming regions G34.26+0.15 and G5.89-0.39. Both regions show considerable mean optical depth in the continuum at 8.3 GHz, $\tau_c \simeq 2$, and the H92α line can be used to study the opacity variations across the face of the nebula. We detected H92α line emission in the ultracompact component A of G34.26+0.15, but not in the ultracompact component B. This result is puzzling since both ultracompact components are similar in continuum flux density and angular size. G5.89-0.39 shows strong velocity gradients in the H92α line, but these cannot be attributed only to rotation, as previously reported.

2.1 Introduction

Compact HII regions (<0.1 pc) are small ionized regions found around one or more young luminous OB stars deeply embedded in their parent molecular cloud. These sources are known to exhibit distinct morphologies (Wood & Churchwell 1989; Kurzt, Churchwell, & Wood 1994), possibly reflecting the conditions of the surrounding gas. The relationship between HII regions and their environment has been one of the motivations to further study the radio recombination lines (RRLs) of HII regions, in order to understand the conditions of the interstellar medium in which these massive stars are formed. RRL from compact HII regions provide a valuable tool to study their velocity structure, which can assist in the determination of the type of HII region and can lead to possible models (Garay, Lizano & Gómez 1994; Gaume, Fey, & Claussen 1994; Garay & Lizano 1999). In this work we

analyze the velocity structure, through the RRL H92α, toward two compact HII regions: G34.3+0.15, which exhibits a cometary-like morphology (Reid & Ho 1985), and G5.89-0.39, which exhibits a shell-like shape with bipolar lobes (Zijlstra et al. 1990; Gómez et al. 1991). Both compact HII regions are characterized by having unusually large radio recombination line widths (≥ 50 km s^{-1}), which are difficult to explain with thermal broadening plus turbulent motions (Garay, Reid, & Moran 1985; Afflerbach et al. 1996). These regions show OH and H$_2$O maser emission, suggesting that they are young, active star forming regions.

G34.26+0.15 is an HII region studied at many wavelengths, including radio continuum (Turner et al. 1974; Reid & Ho 1985; Wood & Churchwell 1989), radio recombination lines (Garay et al. 1985; Garay, Rodríguez, & Van Gorkom 1986; Gaume et al. 1994; Fey et al. 1994) and molecular lines (Benzon & Johnston 1984; Heaton et al. 1985; Anderson & Garay 1986; Gaume & Mutel 1987; Keto, Ho, & Reid 1987; Garay & Rodríguez 1990; Carral & Welch 1992; Watt & Mundy 1999; Gómez et al. 2000). Radio continuum observations show a cometary ultracompact (UC) HII region with extent of $\sim 4''$, with two UC HII to its east, each $\sim 1''$ in angular size, and an extended ring-like HII region. The cometary region seems to be excited by one O7 ZAMS star, assuming a distance of 3.3 kpc (Kuchar & Bania 1994). H76α recombination line observations revealed a velocity gradient, in the north-south direction across the cometary HII region, of ~ 16 km s^{-1} arcsec^{-1}, interpreted as ionized gas rotating perpendicular to the symmetry axis of the cometary HII region (Garay et al. 1986; Gaume et al. 1994). The molecular gas also exhibits a velocity gradient of ~ 15 km s^{-1} arcsec^{-1} over ~0.2 pc (Carral & Welch; Akeson & Carlstrom 1996; Gómez et al. 2000) but in an opposite sense to the velocity gradient of the ionized gas.

G5.89-0.39 (also known as W28 A2) has been studied extensively at radio and IR wavelengths. The radio continuum emission toward this source is optically thick for wavelengths >1.3 cm (Gómez et al. 1991). The HII region may be excited by at least one O6 ZAMS star, assuming a distance of 2.6 kpc (Downes et al. 1980). G5.89-0.39 has one of the most powerful and massive molecular outflows observed in the Galaxy (Harvey & Forveille 1988; Cesaroni et al. 1991; Zijlstra et al. 1990; Acord et al. 1997). The radio continuum exhibits a shell-like core with angular diameter of $\sim 4''$ and faint bipolar lobes in the northwest-southeast direction (Gómez et al. 1991). The orientation of the molecular outflow remains uncertain and it has not been possible to make a reliable comparison between the ionized and molecular outflows. However, the high velocity gas traced both by CS (Cesaroni et al. 1991) and by H$_2$O masers (Hofner & Churchwell 1996) suggests an orientation similar to
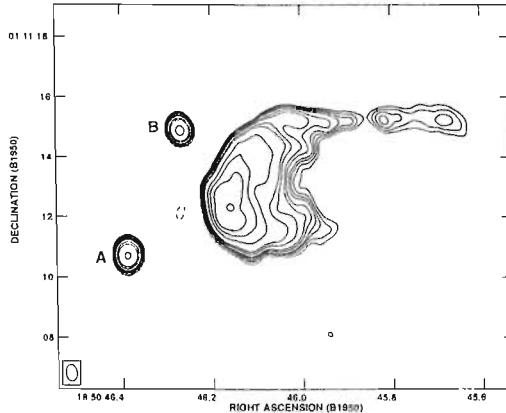
Figure 2.1: VLA continuum contour map of G34.3+0.15 at 3.6-cm, made with natural weighting. Contour levels are -3, 3, 4, 5, 6, 8, 10, 15, 20, 40, 60, and 80 mJy/beam. The rms noise of this map is 0.46 mJy/beam. The ultracompact components A and B are indicated. The half power contour of the beam, $0.''55 \times 0.''37$, with PA = 7°, is shown in the bottom left corner.

that observed in the radio continuum bipolar lobes.

2.2   Observations

The observations were made with the Very Large Array (VLA) of the National Radio Astronomy Observatory (NRAO) in the spectral line mode on 1991 July 09. The array was in the A configuration. We observed with one polarization and 12.5 MHz bandwidth with 64 channels having a frequency separation of 195.3 kHz (7.0 km s^{-1}). The spectral window was centered at a frequency approximately intermediate between the H92α and He92α recombination lines. The angular resolution was $0.''4$ for images made with natural weighting. The flux density scale was determined by observing 1328+307, for which we assumed a flux density of 5.25 Jy at 3.6 cm. The phase calibrator was 1749+096, for which we derive a flux density of 1.71 ± 0.01 Jy. The bandpass calibration was made using the calibrator 1226+023. The observations of G5.89-0.39 were made at a v_{LSR} of 10.0 km s^{-1}, while those of G34.26+0.15 were made at a v_{LSR} of 53.0 km s^{-1}. All data were edited and calibrated following standard procedures for line data and images were made using the NRAO software AIPS. The spectral data were further calibrated by applying the solution obtained from a self-calibration on the continuum channel (which contains the average of the central 75% of the bandpass).

2.3 Results and discussion

2.3.1 G34.26+0.15

A 3.6 cm map of this region made from the continuum channel is shown in Figure 2.1. The well known cometary morphology of the HII region is clearly evident, with the "tail" to the west and the "head" to the east. We can also observe the ultracompact components A and B (Reid & Ho 1985) to the east of the "head". The 3.6 cm total flux density of G34.26+0.15 is 2.36 ± 0.01 Jy. We do not expect to miss significant amounts of flux density in our maps since for the A configuration at 3.6 cm the largest angular scale detectable is ~ 7″, while most of the flux from the source originates at comparable or smaller angular scales. Since at higher frequencies the total flux density of this source reaches ~ 5 Jy, we corroborate the conclusion of Garay et al. (1986) that the source is optically thick below ~ 10 GHz. From the observed flux densities at several frequencies, we estimate a 3.6 cm average optical depth of 1.7 in the continuum.

For the ultracompact components A and B we obtain total flux densities of 84±1 and 72± 1 mJy, respectively. The deconvolved angular diameters are 0″4 and 0″3, for components A and B, respectively. The observed flux densities and angular diameters imply brightness temperatures of about 10^4 K for components A and B, suggesting considerable optical depth in the continuum. From the flux densities reported for sources A and B at 4.8 GHz (33.5 and 20.5 mJy; Wood & Churchwell 1989), 8.3 GHz (84 and 72 mJy; this paper), and 14.7 GHz (140 and 110; Garay et al. 1986) we estimate average optical depths at 8.3 GHz of ~ 2 for both components.

Despite the evidence of significant optical depth in the continuum, we clearly detected H92α emission toward the cometary region and toward component A. In Figure 2.2 we show the continuum emission, the integrated line emission, and the line-to-continuum ratio for the region.

Assuming that the line and continuum have the same excitation temperature, for a given radial velocity we have that

$$\frac{S_l(v)}{S_c} = \frac{[1 - e^{-[\tau_c + \tau_l(v)]}] - (1 - e^{-\tau_c})}{(1 - e^{-\tau_c})}. \tag{2.1}$$

Now, if we assume that the line (but not necessarily the continuum) is optically thin, the
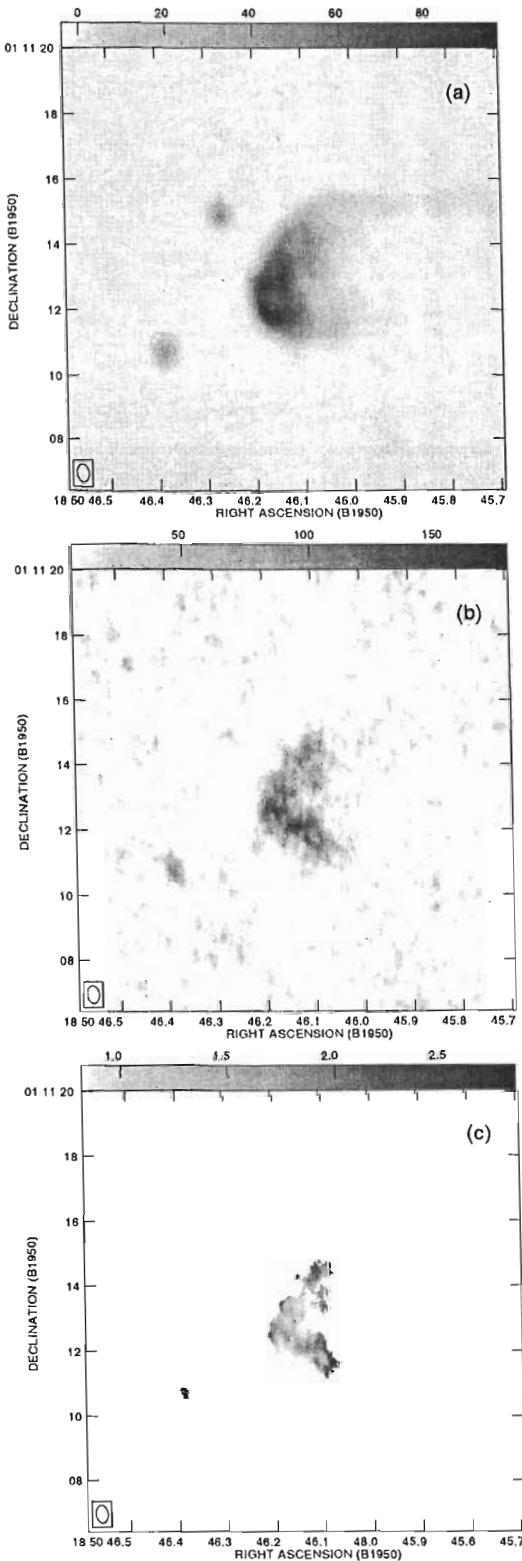
Figure 2.2: Grayscale images of G34.26+0.15 in (a) continuum emission (given in mJy beam^{-1}), (b) integrated line emission (given in mJy beam^{-1} km s^{-1}), and (c) line-to-continuum ratio (given in km s^{-1}). The ranges of the grayscales are given in the wedge on top of each image. The angular resolution is as in Fig. 3.1.
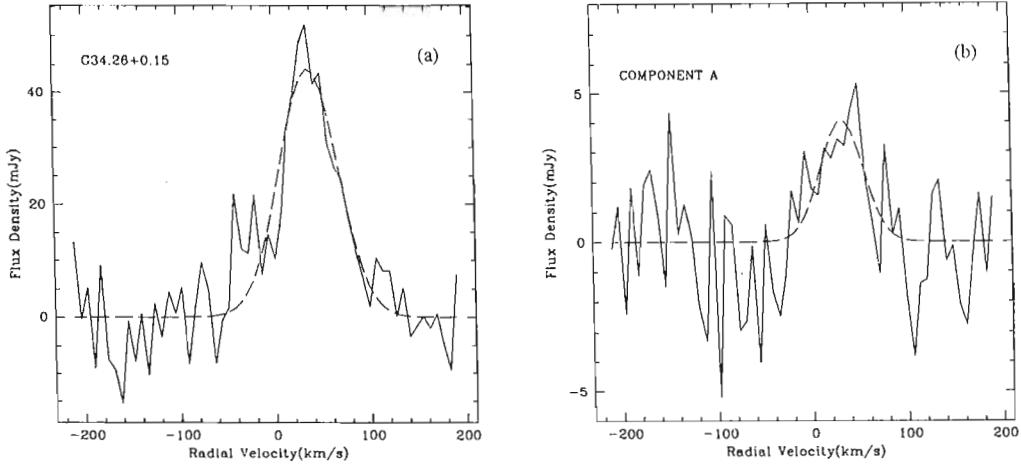
Figure 2.3: (a) H92α spectra from the cometary HII region G34.26+0.15 and (b) from the compact component A. The dashed line indicates the least-squares fit to the data.
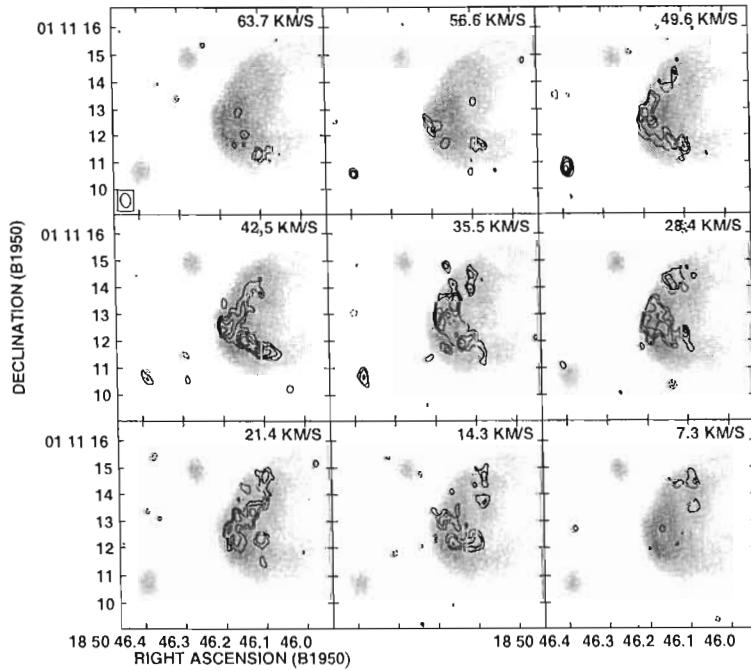
Figure 2.4: Channel images of the H92α emission from G34.26+0.15. Contours are -3, 3, 4, 5, 6, 7 and 8 times 0.57 mJy beam^{-1}. The LSR radial velocity is shown in the top right side of each map. The continuum emission above 6 mJy beam^{-1} is shown in grayscale.

integrated line-to-continuum ratio will be given by

$$\frac{\int S_l dv}{S_c} = \frac{\int \tau_l dv}{(e^{-\tau_c} - 1)}.$$ (2.2)

Adopting an electron temperature of 7500 K (Garay et al. 1986) and ignoring the effect of ionized helium, we find that for the H92α line

$$\int \tau_l dv = 2.7\tau_c.$$ (2.3)

Then, the observed integrated line-to-continuum ratio can be used to estimate the continuum opacity using

$$\frac{\int S_l dv}{S_c} = \frac{2.7\tau_c}{(e^{-\tau_c} - 1)}.$$ (2.4)

This equation implies that integrated line-to-continuum ratios of ~ 2.7 km s^{-1} are expected from optically thin regions, while integrated line-to-continuum ratios of ~ 0.9 km s^{-1} will be observed in regions where $\tau_c \simeq 2$.

From Figure 2.2(c) we can see that the edges of the cometary HII region have line-to continuum ratios (< 1), while the center of the region reaches line-to continuum ratios of ~ 2.5.

We also detect H92α line emission from the ultracompact component A, but not from B. The detection of H92α in component A is unexpected, given that (as derived above) the continuum optical depth of the regions at 8.3 GHz is ~ 2. Indeed, something seems to be enhancing the line emission, because the integrated line-to-continuum ratio for a continuum optical depth of ~ 2 under LTE conditions is about 0.9 km s^{-1}, while we observe ~ 2.2 km s^{-1}. On the other hand, the non detection of component B seems to imply $\tau_c \geq 2$, in agreement with the continuum optical depth derived from the observed continuum flux densities. Given the similarity in angular size and continuum flux densities of component A and B, it is not easy to account for the difference in H92α emission.

However, it should be noted that despite their similarity in the radio continuum, the ultracompact components A and B are quite different in other continuum and line tracers. Campbell et al. (2000) clearly detected component A in the mid-IR, but failed to detect component B. This result suggests that component B is probably a younger, more deeply embedded source than component A. This suggestion is supported by the image of the OH masers in the region, which shows several features associated with component B, but none
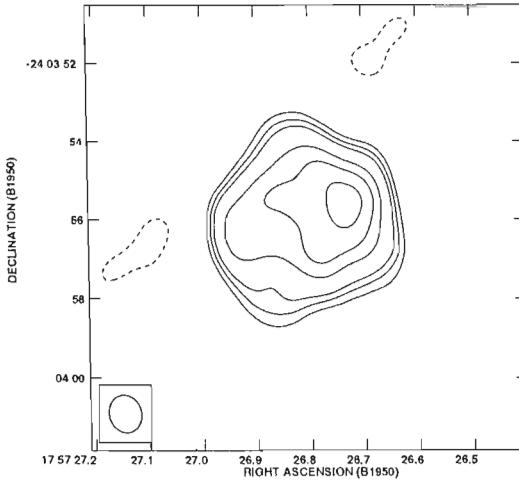
Figure 2.5: VLA continuum contour map of G5.89-0.39 at 3.6-cm, made with natural weighting and a (u,v) taper of 200 kλ. Contour levels are -3, 3, 4, 5, 6, 8, 10, and 12 times 11 mJy/beam, the rms noise of the map. The half power contour of the beam, $0\farcs97 \times 0\farcs81$, with PA = 14°, is shown in the bottom left corner.

with component A (Gaume & Mutel 1987; Zheng, Reid, & Moran 2000). Finally, Hatchell, Fuller, & Millar (2001) suggest that component B is the driving source of a massive outflow seen in SiO. It is well known that the driving sources of molecular outflows are generally deeply embedded in surrounding gas.

In Figure 2.3 we show the spatially integrated H92α spectra from the cometary and from component A. The peak flux density, full width at half maximum, amd radial LSR velocity are 44.2±3.1 mJy, 71.7±5.8 km s^{-1}, and 36.8±2.4 km s^{-1} for the cometary region, and 4.1±1.0 mJy, 53.0±15.1 km s^{-1}, and 32.6±6.4 km s^{-1} for component A. The line width observed toward component A, although large for an HII region, seems to disagree with the suggestion of Gaume et al. (1984) that the continuum emission from this source originates in an ionized stellar wind, since in this case a much wider line would be expected.

Finally, in Figure 2.4 we show the H92α line emission for different radial velocities. The images clearly show the velocity gradient first seen by Garay et al. (1986), with the redshifted line emission coming from the southern half of the cometary and the blueshifted emission coming from the northern half.

2.3.2   G5.89-0.39

A 3.6 cm map of this region is made from the continuum channel is shown in Figure 2.5. In Figure 2.6 we show grayscale images of the continuum, line, and line-to-continuum ratio

of G5.89-0.39. The line emission is not detected over the entire nebula, but mostly toward the E and W edges.

The integrated line-to-continuum ratio goes from values ≤ 1 km s^{-1} at the center of the nebula to $3 - 4$ km s^{-1} at the E and W edges. From the discussion given for G34.26+0.15, we believe that this result implies that the center of the nebula is optically thick in the continuum, with $\tau_c \geq 2$, while the edges are optically thin. This result is consistent with the value of the average opacity, $\tau_c(8.3$ GHz$)\simeq 1.9$, derived from the analysis of Gómez et al. (1990). A simple model to explain the continuum and line emission can be made, following the suggestion of Zijlstra et al. (1990) that the ionized core of G5.89-0.39 has a disk like morphology that is seen approximately edge-on.

In Figure 2.7 we show a cut made approximately in the E-W direction along the center of the nebula for the continuum, line, and line-to-continuum ratio. The cut was centered at $\alpha(1950) = 17^h57^m26\overset{s}{.}77$; $\delta(1950) = -24°03'56\overset{''}{.}6$ with a position angle of $-95°$. In the right-hand side of the same Fig. 2.7 we show the results from a simple LTE model made assuming that the disk has a cavity in its center, with radius of 42% of the total radius, and with a continuum optical depth of $\tau_c = 1.2$ for a line-of-sight along the center of the disk. We further assume that the ionized gas has an electron temperature of $T_e = 7000$ K. We modeled the expected emission using the transfer equation in the continuum as well as in the line emission, the former with a continuum optical depth as defined above, and the latter with a line optical depth $\tau_l \sim 0.84\tau_c$ (Dupree & Goldberg 1970) and a line width velocity of 70 km s^{-1}. Finally the results were convolved with a Gaussian beam of FWHM $\sim 0\overset{''}{.}8$. As noted above, the results obtained are shown on the right part of Fig. 2.7. As can be seen from the figure, the agreement between the observations and our simple model is reasonable.

Zijlstra et al. (1990) found that the H76α emission from the eastern edge peaked at $v_{LSR} \simeq 10$ km s^{-1}, while that from the western edge peaked at $v_{LSR} \simeq 30$ km s^{-1} and suggested that this may imply rotation. The H92α spectra of the eastern and western edges, shown in Figure 2.8, suggest a more complex situation. Toward the eastern edge we detect a single feature with a peaked flux density of $S_l = 1.6 \pm 0.2$ mJy, a full width at half maximum of $\Delta v = 95 \pm 14$ km s^{-1}, and a radial velocity with respect to the local standard of rest of $v_{LSR} = 12 \pm 5$ km s^{-1}. This velocity component is consistent with the result of Zijlstra et al. (1990). However, toward the western edge we detect two features, one has $S_l = 2.0 \pm 0.2$ mJy, $\Delta v = 71 \pm 7$ km s^{-1} and $v_{LSR} = -46 \pm 3$ km s^{-1}, while the other has $S_l = 1.2 \pm 0.2$ mJy, $\Delta v = 51 \pm 10$ km s^{-1} and $v_{LSR} = 67 \pm 4$ km s^{-1}. This line emission
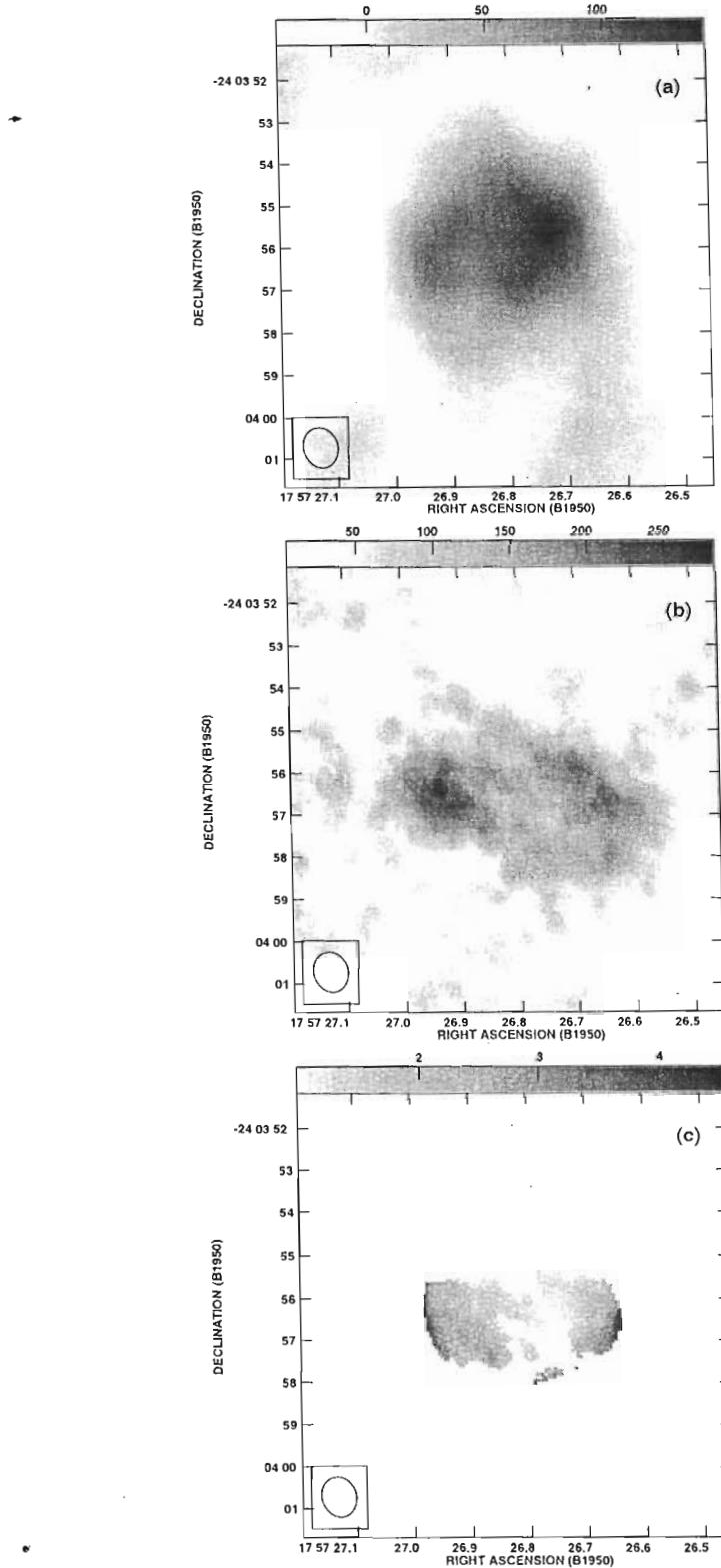
Figure 2.6: Grayscale images of G5.89-0.39 in (a) continuum emission (given in mJy beam^{-1}), (b) integrated line emission (given in mJy beam^{-1} km s^{-1}), and (c) line-to-continuum ratio (given in km s^{-1}). The ranges of the grayscales are given in the wedge on top of each image. The angular resolution is as in Fig. 2.5.
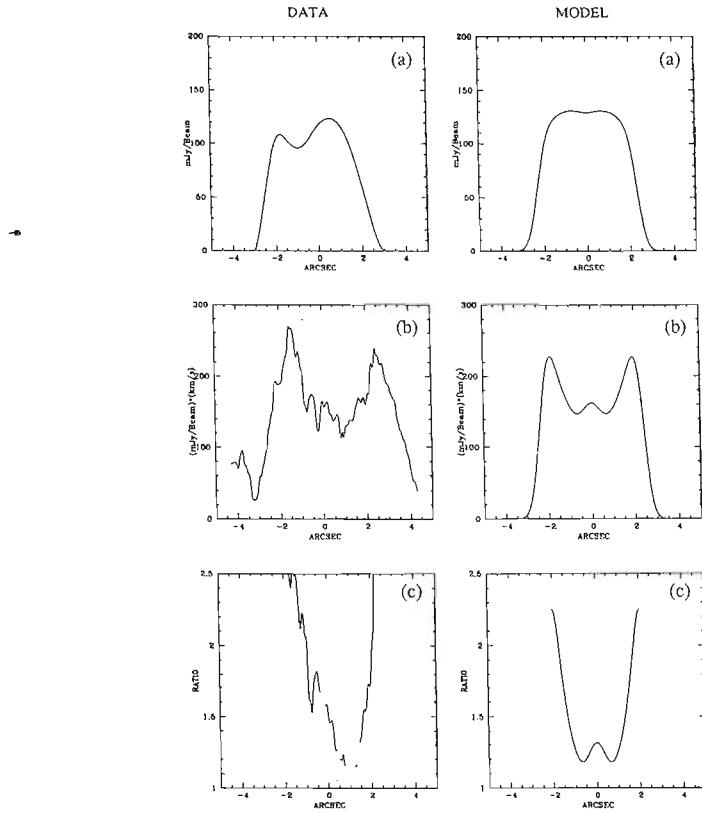
Figure 2.7: Left: Slices of the source G5.89-0.39, in continuum (a), line integrated emission (b), and line-to-continuum ratio (c). Right: Cuts from the model described in the text for the same parameters of the left side of the figure.
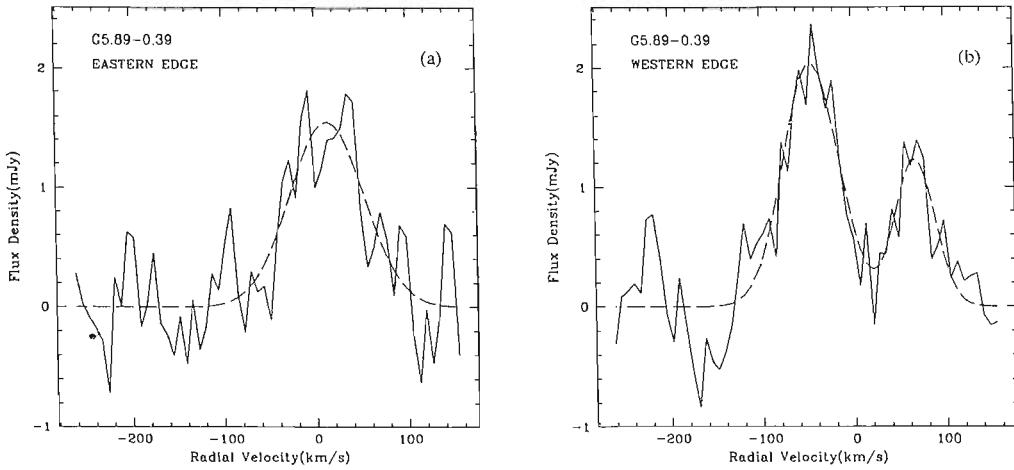
Figure 2.8: (a) H92α spectra from the eastern edge and (b) from the western edge of G5.89-0.39. The dashed line indicates the least-squares fit to the data.

appears to suggest more complex kinematics than that reported by Zijlstra et al. (1990) and we tentatively attribute the difference to the considerable optical depth of the source at 8.3 GHz or to peculiar kinematics. Zijlstra et al. (1990) attributed the observed velocity gradients to rotation, while our results suggest a less ordered model.

2.4   Conclusions

Using the VLA, we observed 8.3 GHz continuum and H92α radio recombination line toward the compact H II regions G34.26+0.15 and G5.89-0.39. Both sources have considerable optical depth at this wavelength and we discussed the continuum opacity variations across the face of the HII regions.

We detected for the first time radio recombination line emission from the ultracompact component A in G34.26+0.15. This detection is puzzling, since the region is optically thick in the continuum at the observed frequency and a much weaker line was expected.

We modeled adequately the continuum and integrated line emissions in G5.89-0.39 in terms of a disk-like structure such as the one proposed by Zijlstra et al. (1990). The velocity gradient in this source is complex and requires more than rotation to be explained.

Chapter 3

A New Warm Molecular Clump toward the Star Forming Region G34.26+0.15

Gómez, Y., Rodríguez-Rico, C. A., Rodríguez, L. F., & Garay, G.

Resumen

G34.26+0.15 es una región de formación estelar que, al ser observada en radiocontinuo, muestra diferentes componentes: una región HII ultracompacta con morfología cometaria llamada componente C (Reid & Ho 1985; Garay et al. 1986; Wood & Churchwell 1989; Gaume et al. 1994), dos regiones HII ultracompactas llamadas A y B con diámetro menor a 2000 AU (Reid & Ho 1985; Garay & Rodríguez 1990), y una región HII extendida con morfología de anillo de 1′ de diámetro llamada componente D (Reid & Ho 1985; Fey et al. 1992; Fey et al. 1994). G34.26+0.15 ha sido estudiada en radiocontinuo (Turner et al. 1974; Reid & Ho 1985; Wood & Churchwell 1989), RRL (Garay, Reid, & Moran 1985;

Garay, Rodríguez, & van Gorkom 1986; Gaume, Fey, & Claussen 1994; Fey et al. 1994) y líneas moleculares (Benson & Johnston 1984; Heaton et al. 1985; Anderson & Garay 1986; Gaume & Mutel 1987; Keto, Ho, & Reid 1987; Garay & Rodríguez 1990; Carral & Welch 1992).

Se ha observado emisión maser de H_2O y OH hacia G34.26+0.15 (Genzel & Downes 1977; Garay et al. 1985; Gaume & Mutel 1987; Fey et al. 1994). El gas molecular ha sido observado en NH_3, HCO^+, SO, CH_3CN, y CO (Heaton, Little, & Bishop 1989; Anderson & Garay 1986; Carral, Welch, & Wright 1987; Henkel, Wilson, & Mauersberger 1987; Carral & Welch 1992; Garay & Rodríguez 1990; Churchwell, Walmsley, & Wood 1992; Heaton et al. 1993; Akeson & Carlstrom 1996; Watt & Mundy 1999) y muestra la presencia de una estructura molecular localizada cerca de la "cabeza" de la región HII cometaria. La cinemática del gas molecular hacia la componente C muestra un gradiente de velocidad de $\sim$ 15 km s^{-1} pc^{-1} a lo largo una región de $\sim$ 0.2 pc (Carral & Welch 1992; Akeson & Carlstrom 1996) que está orientado en el sentido opuesto al gradiente de velocidad del gas ionizado al ser observado en RRLs (Garay et al. 1986; Gaume et al. 1994). Garay & Rodríguez (1990) interpretaron la emisión de amoníaco invocando la existencia de dos componentes principales de material molecular: un cúmulo con forma de disco con gas tibio, ópticamente grueso (T$\sim$ 60 K, n_{H_2} $\sim$ 10^6 cm^{-3}) y una envolvente molecular que le rodea (T$\sim$ 18 K, n_{H_2} $\sim$ 10^4 cm^{-3}).

En este capítulo presentamos un reanálisis de datos del VLA de las transiciones de inversión de amoníaco (2,2) and (3,3) tomados por Garay & Rodríguez para: (1) investigar la relación entre la cinemtática de la nube molecular y la región HII observada en RRL H92α (ver Capítulo 2) y (2) buscar emisión hacia la fuente milimétrica recientemente identificada G34.24+0.13MM, localizada 84'' al sureste de la componente C, la cual ha sido interpretada como una proto-estrella B altamente embebida (Hunter et al. 1998). No se detectó emisión de amoníaco a un nivel de 3σ (30 mJy $beam^{-1}$) hacia la fuente milimétrica pero encontramos un nuevo cúmulo de amoníaco hacia el noroeste de G34.26+0.15 (además de la estructura molecular). Este nuevo grumo de amoníaco está asociado con máseres de agua. y se le estimó una temperatura rotacional de $\sim$ 54 $\pm$ 12 K, un diámetro de $\sim$ 0.15 pc (suponiendo una distancia de 3.8 kpc) y una masa molecular de 10 $M_\odot$ (suponiendo un cociente [H_2/NH_3] de 10^7). Estos resultados sugieren que el grumo podría tener una estrella embebida y que además de las estrellas masivas que excitan las regiones HII previamente reportadas, pueden existir otras estrellas jóvenes de menor masa en la región.

Abstract

In this work we reanalyze VLA ammonia (2,2) and (3,3) observations toward the massive star forming region G34.26+0.15. We find one new ammonia clump with (2,2) and (3,3) emission toward the northwest in addition to the main molecular structure previously reported. The new clump is associated with water maser spots and we estimate for it a rotational temperature of $\sim 54 \pm 12$ K, a diameter of ~ 0.15 pc (assuming a distance of 3.8 kpc) and a molecular mass of 10 $M_\odot$ (assuming an $[H_2/NH_3]$ ratio of 10^7). These results suggest that the clump could have an embedded star and that in addition to the massive stars that excite the HII regions previously reported, there may be other young stars of lower mass in the region.

3.1 Introduction

Ultracompact HII regions are small (< 0.1 pc) and dense ($n_e > 10^4$ cm^{-3}) regions of ionized gas generally excited by O and B stars that are still embedded in their natal molecular cloud (Ryle & Downes 1967; Wood and Churchwell 1989). The presence of maser emission and warm molecular gas are strong indicators of recent star formation (cf. Garay & Lizano 1999 and references therein). G34.26+0.15 has been extensively studied in radio continuum (Turner et al. 1974; Reid & Ho 1985; Wood & Churchwell 1989), radio recombination lines (Garay, Reid, & Moran 1985; Garay, Rodríguez, & van Gorkom 1986; Gaume, Fey, & Claussen 1994; Fey et al. 1994) and molecular lines (Benson & Johnston 1984; Heaton et al. 1985; Anderson & Garay 1986;Gaume & Mutel 1987; Keto, Ho, & Reid 1987; Garay & Rodríguez 1990; Carral & Welch 1992). At radio continuum frequencies it exhibits several components: an ultracompact HII region with a cometary shapenamed component C (Reid & Ho 1985; Garay et al. 1986; Wood & Churchwell 1989; Gaume et al. 1994), two ultracompact HII regions called A and B with diameter less than 2000 AU (Reid & Ho 1985; Garay & Rodríguez 1990), and an extended ring-like HII region with a diameter of 1' called component D (Reid & Ho 1985; Fey et al. 1992; Fey et al. 1994). H$_2$O and OH maser emission have been observed toward G34.26+0.15 (Genzel & Downes 1977; Garay et al. 1985; Gaume & Mutel 1987; Fey et al. 1994). Molecular gas has been mapped in NH$_3$, HCO$^+$, SO, CH$_3$CN, and CO (Heaton, Little, & Bishop 1989; Anderson & Garay 1986; Carral, Welch, & Wright 1987; Henkel, Wilson, & Mauersberger 1987; Carral & Welch 1992; Garay & Rodríguez 1990; Churchwell, Walmsley, & Wood 1992; Heaton et al. 1993; Akeson & Carlstrom 1996; Watt & Mundy 1999) showing the presence of molecular structure located close to the "head" of the cometary HII region. The kinematics of
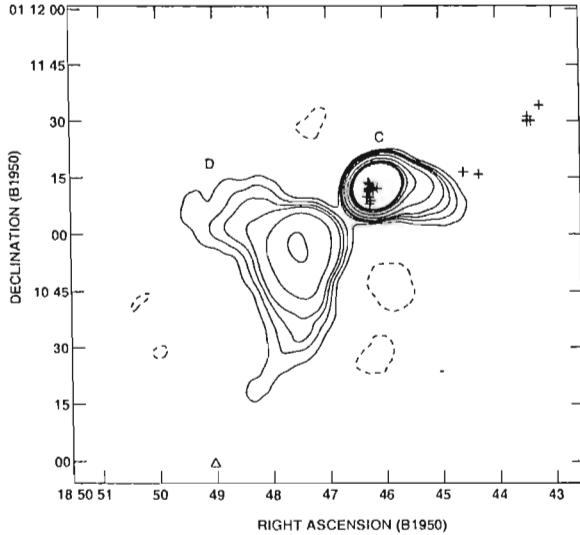
Figure 3.1: VLA continuum contour map of G34.3+0.15 at 1.3 cm with $\sim 7''$ resolution. Contour levels are -3, 3, 5, 7, 9, 15, 30, 50, 70, and 90 times 6 mJy/beam, the rms noise of the map. The crosses indicate the position of the H_2O masers reported by Fey et al. 1994. The small triangle at the bottom of the figure marks the position of the millimeter source proposed as a massive protostellar object (Hunter et al. 1998)

the molecular gas shows a gradient of ~ 15 km s^{-1} pc^{-1} in ~ 0.2 pc (Carral & Welch 1992; Akeson & Carlstrom 1996; this paper) which is in opposite sense to the velocity gradient of the ionized gas across component C observed in radio recombination lines (Garay et al. 1986; Gaume et al. 1994). Garay & Rodríguez (1990) interpreted the ammonia emission as arising from two main components of molecular material: a warm, optically thick disk-like clump (T~ 60 K, $n_{H_2} \sim 10^6$ cm^{-3}) and a molecular envelope around it (T~ 18 K, $n_{H_2} \sim 10^4$ cm^{-3}).

In this work we reanalyzed the VLA data of the (2,2) and (3,3) inversion transitions of ammonia taken from Garay & Rodríguez in order to search for emission toward the recently identified millimeter source G34.24+0.13MM, located 84$''$ southeast of component C, that has been interpreted as deeply embedded proto-B star (Hunter et al. 1998). No ammonia emission was detected at a 3-sigma level of 30 mJy beam^{-1} toward the millimeter source, but we found one new ammonia clump toward the northwest of G34.26+0.15 which is closely associated with water maser spots.

Table 3.1: Observed Radio Continuum Parameters at 1.3 cm

Component	Flux Density (Jy)	Peak Flux (mJy/beam)	α (1950) (h m s)	δ (1950) (° ′ ″)	Deconv. Size (″)
C	5.1 ± 0.1^{a}	4200	18 50 46.14	01 11 12.7	~ 3
D	1.6 ± 0.1	194	18 50 47.55	01 10 57.0	~ 20

^{a} Includes flux density of compact components A and B.

3.2 Observations.

The observations were made using the Very Large Array (VLA) of the NRAO. All data were edited and calibrated following standard procedures and maps were made using the NRAO software AIPS. The observations were taken on January 23, 1986 in the D configuration toward the star forming region G34.26+0.15. A summary of the observations is reported in Garay & Rodríguez (1990). The (J,K)=(2,2) and (3,3) inversion transitions of the ammonia molecule (NH$_3$) were observed assuming a rest frequency of 23722.633 and 23870.129 MHz, respectively. The bandpass was 12.5 MHz, centered at an LSR velocity of 55 km s^{-1}, and we used 31 spectral channels 195.3 kHz wide each (~ 2.5 km s^{-1} at the observing frequencies). The flux density scale was determined from observations of the amplitude calibrator 3C 286, for which a flux density of 2.93 Jy was assumed. The phase calibrator was 1749+096, for which a bootstraped 1.3 cm flux density of 3.70 ± 0.09 Jy was obtained. The shape of the bandpass was determined from observations of the source 3C 84, from which we determine a flux density of 34 ± 2 Jy. Line data were self-calibrated (Schwab 1980) in phase and amplitude using the continuum channel (including the central 75% of the bandpass). The continuum (line-free) channels were subtracted from the visibility data by use of the task UVLIN. Maps were made by using the task IMAGR with the robust parameter of Briggs (1995) set equal to 5 (equivalent to natural weight) and a Gaussian taper of 30 kλ which resulted in a synthesized beam of ~ 7″ × 6″ for the (2,2) and (3,3) transitions. The rms noise level in a single spectral line channel were about 11 and 13 mJy beam^{-1} for the (2,2) and (3,3) observations, respectively.

Table 3.2: AMMONIA LINE PARAMETERS

Component	Transition	Flux Density (mJy)	V_{LSR} (km s^{-1})	ΔV (km s^{-1})
1	(2,2;m)	-200 ± 47	62.4 ± 0.6	4.2 ± 1.0
	(3,3;m)	266 ± 32	59.3 ± 0.5	8.5 ± 1.0
2	(2,2;m)	251 ± 40	57.2 ± 0.5	6.9 ± 1.3
	(3,3;m)	469 ± 35	59.3 ± 0.3	9.6 ± 0.8
3	(2,2;m)	156 ± 20	58.2 ± 0.4	6.4 ± 1.0
	(3,3;m)	245 ± 20	59.7 ± 0.2	6.1 ± 0.6
4	(2,2;m)	41 ± 6	60.8 ± 0.5	7.9 ± 1.3
	(3,3;m)	56 ± 6	61.2 ± 0.3	6.8 ± 0.8

3.3 Results and Discussion

3.3.1 Continuum

Figure 3.1 shows a 1.3 cm radio continuum self-calibrated map made from the continuum channel of the (2,2) data. The map exhibits the bright cometary-like H II region (component C) and the extended ring-like H II region to the southeast (component D). The observed radio continuum parameters of these components are show in Table 3.1. Note that the A and B compact H II regions are not resolved and they appear blended with component C due to the low angular resolution of the observations ($\sim$ 7″). For component C we estimate a luminosity of $2.5 \times 10^5 \, L_\odot$, which is equivalent to that provided by an O6 ZAMS star, in good agreement with previous estimates (Andersson & Garay 1986; Garay et al. 1986; Heaton et al. 1989; Garay & Rodríguez 1990).

3.3.2 Molecular Gas

Line maps in the (2,2) and (3,3) transitions of ammonia, shown in Figure 3.2, reveal the presence of an extended molecular structure toward component C (0.2 × 0.1 pc), which is seen in the velocity range from 52.5 km s^{-1} to 64.9 km s^{-1} and centered at $\sim$ 59 km s^{-1}. Figure 3.3 presents contours of the velocity integrated (2,2) line emission (from 52.5 to 64.8 km s^{-1}) overlaid on a 1.3 cm continuum contour which indicates the extent of the ratio continuum tracing the free-free emission. Based on the morphology, it is possible to identify five different ammonia components, including the new ammonia clump (component 4) reported here. The spectra of the spatially integrated (2,2) and (3,3) ammonia emission from the four clearly detected (see below) ammonia components (marked with

boxes in Fig. 3.3) are presented in Figure 3.4. The parameters of the main ammonia lines from each component, determined by fitting a Gaussian profile to the corresponding spectra, are given in Table 3.2. Component 1 shows the main (2,2) transition of ammonia in absorption and the main (3,3) line in emission, a situation that was interpreted by Garay & Rodríguez (1990) as due to a blend, within a synthesized beam, of two components of molecular gas in front of the H II region: a warm, optically thick cloud of gas very close to the H II region, and an extended component of cold gas with moderate optical depth. Components 2 and 3 exhibit the main (2,2) and (3,3) ammonia lines in emission. The presence of component 3 was not reported by Garay & Rodríguez (1990) but it appears detected in the (3,3) ammonia transition map by Heaton et al. (1989). Components 4 and 5 are weak, new ammonia clumps that are associated with water masers. Since component 5 is only marginally detected ($\sim 4\,\sigma$ level) in the (2,2) ammonia transition and not detected in the main (3,3) ammonia line, we will not consider it further. However, we note that emission at 350 μm (Hunter et al. 1998) and HCO$^+$ (Carral & Welch 1992) has been detected at position of component 5. More sensitive observations are needed to confirm this ammonia clump. Component 4 has been considered in this work as a new molecular clump because it was detected in both (2,2) and (3,3) ammonia lines, and it is associated with water maser emission. Until now no radio continuum has been found toward this position. Garay et al. (1986) set a 5-σ level of 0.5 mJy beam^{-1} at 14.7 GHz.

3.3.3 The New Ammonia Clump in G34.26+0.15: Component 4

The average central velocity of the molecular gas in emission in components 1, 2, and 3 is around 59 km s^{-1}, whereas the average velocity of component 4 is approximately 61 km s^{-1}, which is slightly redshifted with respect to the other components. This new ammonia clump has four water masers associated with it (Fey et al. 1994), as can be seen in Fig. 3.3. Three of these masers are located just at the center of the clump and have an average velocity of ~ -15 km s^{-1}, the other water maser spot, which is at the edge of the clump, has a velocity of +36.3 km s^{-1}. All these masers appear blueshifted with respect to the ammonia gas velocity ($\sim +61$ km s^{-1}). Given the coincidence in position between the ammonia gas and the water masers we consider that the masers are associated with the clump. The large velocity difference between the ammonia and the water masers suggests that there may be outflow activity associated with this clump.

Since both the (2,2) and (3,3) main lines appear in emission toward component 4 (see
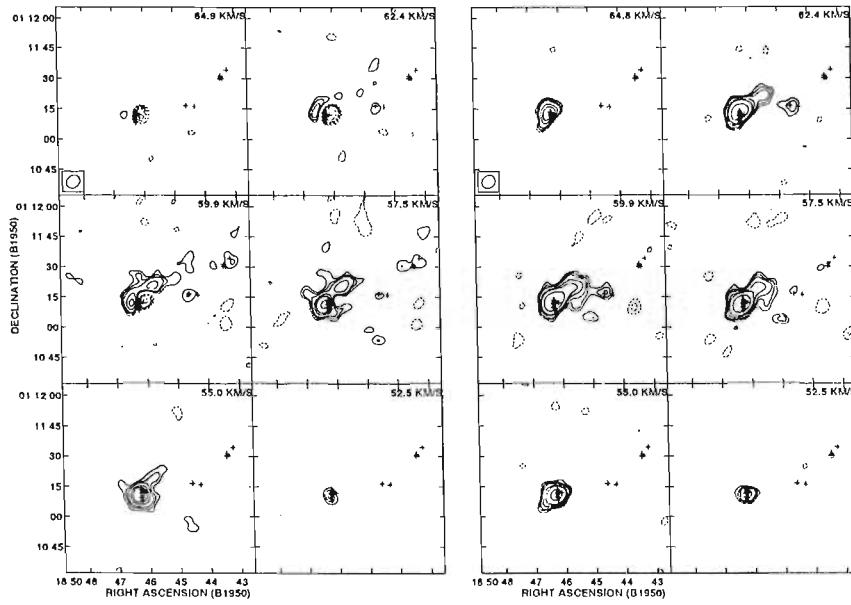
Figure 3.2: Channel maps of the ammonia (2,2) and (3,3) transitions toward the G34.26+0.15 region. Left: (2,2) transition. Contour levels are $-15, -9, -7, -5, -3, 3, 4, 5, 7, 9$, and 15×11 mJy beam^{-1}, the rms noise of the maps. Right: (3,3) transition. Contour levels are $-3, 3, 4, 5, 7, 9$, and 15×13 mJy beam^{-1}, the rms noise of the maps.

Fig. 3.2), this allows us to estimate the rotational temperature of the ammonia clump. Assuming an LTE ortho-para ratio for the NH_3 molecule and assuming that the emission is optically thin, the average rotational temperature from the ratio of the (2,2) and (3,3) main lines is given by

$$T_{rot}(33, 22) = 59.6 \left[ln \left(3.5 \frac{S_L(2,2)\Delta v(2,2)}{S_L(3,3)\Delta v(3,3)} \right) \right]^{-1} K,$$

where $S_L(J,K)$ and $\Delta v(J,K)$ are the flux density and the line width of the main line of the (J,K) inversion transition. Using the parameters given in Table 3.2 for this component we derive an average rotational temperature of $\sim 54 \pm 12$ K. This warm temperature suggests the presence of an embedded star. A B0 ZAMS embedded star (with luminosity of $\sim 2.5 \times 10^4 \, L_\odot$) could provide the observed temperature. This temperature is obtained assuming the molecular cloud is a black body heated by the central star. One difficulty with this interpretation is that, if an optically-thin HII region is produced by the B0 ZAMS star, a source with flux density of order $\sim 10^2$ mJy would be expected. This flux density is well above the upper limit of ~ 0.5 mJy (Garay et al. 1986). However, it is well known that
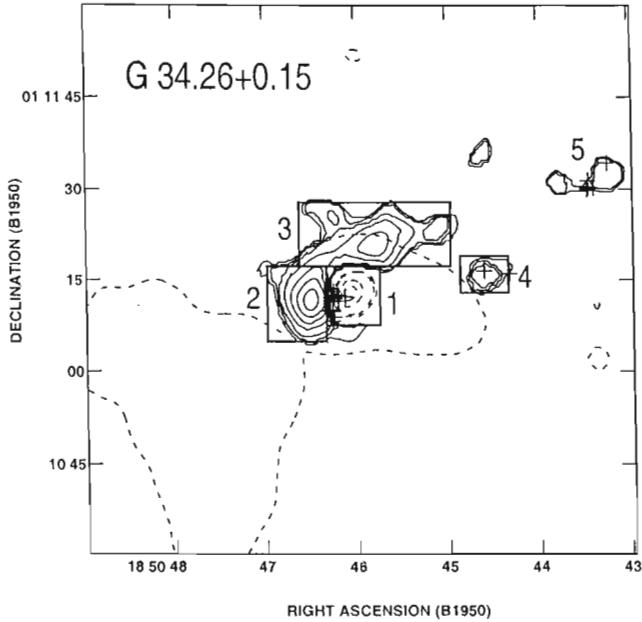
Figure 3.3: Contour map of the zero moment of the (2,2) emission toward the H II complex. The extent of the 1.3 cm radio continuum emission is shown with a dashed line. Contour levels are −90, −70, −50, −30, −20, 10, 15, 20, 30, 40, 50, 60, 70, 80, and 90 percent of 120 mJy beam^{-1} km s^{-1}. The different ammonia components, including the new ammonia clump, are enclosed in thick-line rectangles and indicated with numbers. The crosses indicate the position of the H_2O maser spots (Fey et al. 1994).

observed flux densities from H II regions excited by young massive stars are much lower than expected (Carral et al. 1999).

Can the heating be provided externally by the O6 ZAMS star ($\sim 2.5 \times 10^5 L_\odot$) that ionizes the cometary H II region (component C)? We assume a distance from the H II region to the clump of ~ 0.55 pc (30″ at a distance of 3.8 kpc). Following Scoville & Kwan (1976) and assuming that there is no absorption between the O6 star and the ammonia clump and a dust absorptivity frequency dependence of ν^{+1}, we derive a temperature of ~ 50 K, similar to the derived rotational temperature. In this case, the clump could be heated externally by the central star of the H II region. However, most likely there is considerable opacity between the two objects and following the discussion of Scoville & Kwan (1976) and Natta et al. (1981) a lower value, of order 25 K, would be expected for the temperature of the clump, if externally heated.

Given the uncertainties in our knowledge of the conditions in this complex region, we cannot argue in a compelling way for the presence of a star embedded in the clump. However, the association with water masers and the warm temperature of the clump suggest an
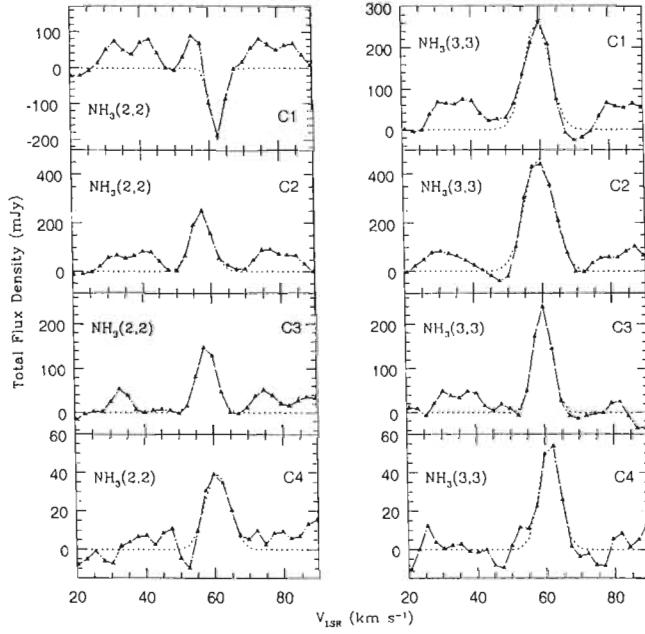
Figure 3.4: Spectra of the spatially integrated (2,2) and (3,3) ammonia emission from four different components (marked with boxes in Figure 3.3) identified toward G34.26+0.15. The fit to the main transition is shown with dashed lines.

embedded energy source.

Assuming an LTE population for all ammonia levels, it is possible to estimate the total column density of NH_3 for the clump knowing the optical depth of a (J,K) inversion transition and the rotational temperature, by the relation (Garay & Rodríguez 1990)

$$
\begin{aligned}
N(NH_3) &= \frac{1.65 \times 10^{14}}{\nu_{GHz} \, g_K} \frac{J(J+1)}{K^2(2J+1)} \Delta V \\
&\times \tau(J,K) \, Q \, T_{ex} \, exp(E/kT_{rot}),
\end{aligned}
$$

where ν is the transition frequency in GHz, g_K is the statistical weight, $E(J,K)$ is the rotational energy of the (J,K) level above the ground state, ΔV is the line width in km s^{-1}, Q is the partition function, and k is Boltzmann's constant. For $T_{rot} \gg 20$ K, the partition function is given by (e.g., Genzel et al. 1982)

$$
Q = 115 \left[\frac{T_{rot}}{200K} \right]^{3/2}.
$$
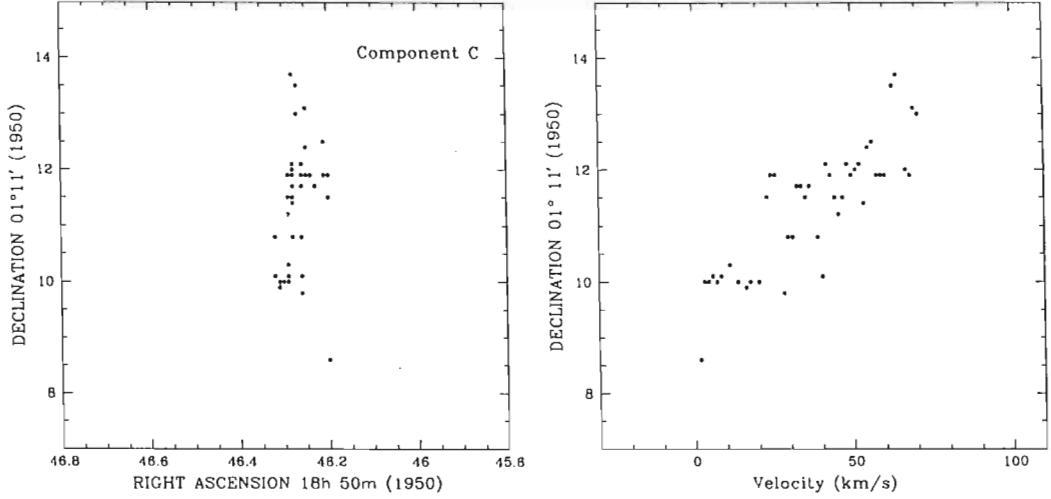
Figure 3.5: (Left) Distribution of water maser positions toward component C. (Right) Declination versus radial velocity for the water masers toward component C.

An upper limit to the opacity of the main line of the (3,3) transition, $\tau(3,3;m)$, can be obtained using the expression

$$\frac{S_L(3,3;m)}{S_L(3,3;s)} = \frac{1 - exp[-\tau(3,3;m)]}{1 - exp[-\tau(3,3;m)/33]},$$

where $S(3,3;s)$ is the flux density of a satellite line of the (3,3) transition. For component 4 we estimate, from the spectrum shown in Fig. 3.4, that $S_L(3,3;m)/S_L(3,3;s) \geq 10$, implying $\tau(3,3;m) \leq 3$. A more direct estimate of $\tau(3,3;m)$ can be derived from the peak brightness temperature, $T_L^b = 3.11(S_L/\Theta_b^2)$, where S_L is in mJy and Θ_b in arcsec. In the (3,3,m) line, clump 4 has a deconvolved angular size of $\sim 8''1$ (~ 0.15 pc at the distance of 3.8 kpc) and a flux density of $\sim 56 \pm 6$ mJy. From the radiative transfer equation

$$T_L^b = f(T_{ex} - T_{bg})[1 - exp(-\tau(3,3;m))] \ ,$$

where f is the filling factor, assuming that $T_{ex} = T_{rot} = 54$ K, $T_{bg} = 2.7$ K, and $f = 1$, we find $\tau(3,3;m) \simeq 0.061$. Note that this value provides a lower limit to the (3,3;m) opacity since f is likely to be smaller than 1. Since $\tau(3,3) \simeq 1.12\tau(3,3;m)$, then $\tau(3,3) \simeq 0.068$. The total ammonia column density is $\geq 2.7 \times 10^{15}$ cm^{-2}. Further, the molecular hydrogen density can be estimated from the total column density assuming a path length and a [H$_2$/NH$_3$] abundance ratio. For clumps in massive star forming regions a wide range of values of this

ratio have been reported, from $\sim 10^6$ to 10^8 (Garay & Lizano 1999; Harju, Walmsley, & Wouterloot 1993). Here we adopt $[H_2/NH_3]=10^7$. Using a path length of 0.15 pc, equal to the projected linear size, we obtain $n(H_2) \geq 6 \times 10^4$ cm^{-3}. Assuming a spherical structure we then estimate a molecular mass for the clump of $\geq 10 \ M_\odot$. An estimate of the virial mass for this clump gives $\sim 300 \ M_\odot$. The large difference between the two estimates suggests that the clump is not in virial equilibrium, but probably undergoing expansion and/or outflowing motions. However, given the uncertainties in the mass determination from the ammonia lines, this result is not conclusive.

3.3.4 The Molecular Gas around Component C

As shown in Fig. 3.3, several of the water maser spots reported by Fey et al. (1994) lay projected between the emission and absorption features seen toward the C component in the (2,2) ammonia line. In order to investigate if there is any relation between the kinematics of the ammonia gas and the water masers located near the "head" of the H II region we selected all 43 water masers from Fey et al. (1994) in the velocity range from 1.8 to 70.5 km s^{-1}. Masers with velocities higher than this range where not taken into account since it is very unlikely that they could be gravitationally bound. Figure 3.5 shows the distribution in position and radial velocity of the water masers in the vicinity of the H II region C. To the north the masers are redshifted and to the south they are blueshifted. We measure a velocity shift, ΔV, of $\simeq 70$ km s^{-1} over an angular extent, $\Delta\Theta$, of $\simeq 5\rlap{.}''3$ (~ 0.098 pc), implying a velocity gradient of ~ 700 km s^{-1} pc^{-1} and a virial mass of $\sim 10^4 \ M_\odot$.

The first-order moment slice from the (3,3) ammonia emission through $\alpha(1950) = 18^h 50^m 46\rlap{.}^s31$ and along a declination from $05''$ to $20''$ where the water masers appear shows a slight velocity gradient in the same sign as the water masers do, with higher velocities toward the north and lower velocities toward the south. This shift corresponds to a velocity gradient of ~ 15 km s^{-1} pc^{-1}. This value is consistent with other estimates: 13 km s^{-1} pc^{-1} for the H^{13}CN, and 20 km s^{-1} pc^{-1} for the SO in 0.2 pc (Carral & Welch 1992); 16 km s^{-1} pc^{-1} for the CH$_3$CN in 0.18 pc (Akeson & Carlstrom 1996). These values are consistent with a virial mass of $\sim 80 \pm 20 \ M_\odot$. We then conclude that the kinematics of the water masers cannot be attributed to bound motions and are most likely the result of shock acceleration.

3.4 Conclusions

We found one new warm ammonia clump toward the northwest of the HII region G34.26+0.15. Our study suggests that in addition to the massive stars that excite the HII regions previously reported, there could be other young stars of lower mass in the region. However, the presence of a star embedded in the clump is not certain. On one hand, the association with water masers and the warm temperature of the clump suggest an embedded energy source. On the other hand, the mass of the clump ($\sim 10\ M_\odot$, obtained assuming an $[H_2/NH_3]$ ratio of 10^7) is not very large and the observed temperature ($\sim 54 \pm 12$ K) may be accounted for by heating from the O6 ZAMS star that ionizes the cometary HII region. A comparison of the kinematics of the water masers with the kinematics of the molecular gas at the head of the HII region shows that both have a velocity gradient in the same direction with the blueshifted components to the south and the redshifted to the north. However, the gradient derived from the water masers is nearly two orders of magnitude larger than that derived from other molecular lines suggesting that the kinematics of the water masers do not have a gravitationally bound nature.

Chapter 4

VLA H92α and H53α Radio Recombination Line Observations of M82

Rodríguez-Rico, C. A., Viallefond. F., Zhao, J. H., Goss, W. M., Anantharamaiah, K. R.

Resumen

M82 es un excelente candidato para investigar las condiciones físicas de una galaxia con brote de formación estelar ya que es uno de los objetos más cercanos ($\sim$3 Mpc) y brillantes de su clase. Una gran cantidad de gas ionizado en esta galaxia se encuentra en regiones que contienen grandes cantidades de polvo: en M82 la extinción en magnitudes visibles, A_V, puede alcanzar $\sim$ 15 mag. Las observaciones en longitudes de onda de radio, que no son afectadas por oscurecimiento por polvo, juegan un papel clave en la determinación de

las propiedades físicas del gas ionizado en galaxias con brote de formación estelar. M82 ha sido observada en el radiocontinuo en un amplio rango de frecuencias (Kronberg, Biermann & Schwab 1985; McDonald et al. 2002) y a través de observaciones con resolución angular < 0.″2 (McDonald et al. 2002) se sabe que es huésped de una población de fuentes compactas. El número total de fuentes compactas decrece a 20 cm (comparado con observaciones a 2 cm); este resultado ha sido interpretado como debido a absorción libre-libre por gas ionizado en regiones HII compactas. De las 46 fuentes compactas identificadas por McDonald et al. (2002), ~ 35% fueron clasificadas como regiones HII basandose en sus espectros de continuo.

La distribución y cinemática del gas ionizado en los parsecs centrales de M82 se han estudiado con anterioridad usando RRLs. Las primeras detecciones de RRLs de M82 (Seaquist & Bell 1977; Chaisson & Rodríguez 1977) fueron un gran logro que condujeron a posteriores investigaciones de RRLs extragalácticas. Las observaciones con el VLA de RRLs a frecuencias de hasta 8 GHz por Anantharamaiah et al. (1990) hacia NGC 253 fueron una gran motivación para realizar más observaciones interferométricas de RRLs a la misma frecuencia (Anantharamaiah et al. 1993; Zhao et al. 1996; Mohan et al. 2002) así como a frecuencias más altas (Zhao et al. 2001; Anantharamaiah et al. 2000) hacia galaxias con brote de formación estelar. Usando la emisión integrada total, se hicieron estimaciones globales de las propiedades del gas ionizado en M82 (Seaquist, Bell & Bignell, 1985). Roelfsema (1987) obtuvo el campo de velocidades de M82 a una resolución angular moderada (~ 13″), usando observaciones de la RRL H166α (a 1.4 GHz) obtenidas con el Westerbork Synthesis Radio Telescope. Estas observaciones muestran la rotación del gas ionizado en los 600 pc centrales, con rotación de cuerpo rígido dentro de un radio de ~ 170 pc o 8″. El campo de velocidades fue obtenido también usando la línea de [Ne II] en el mediano IR con resolución angular de 2″ (Achtermann & Lacy 1995). Los campos de velocidades obtenidos de las observaciones de H166α y [Ne II] no son consistentes, especialmente para la mitad lcalizada hacia el SW de M82. Sin embargo, las diferentes resoluciones angulares con que se llevaron a cabo la observaciones de cada línea impide una comparación directa. Las observaciones de RRLs con alta resolución angular fueron necesarias para entender la cinemática del gas ionizado. Seaquist et al. (1996) observaron la línea H41α con resolución angular de 4″ y, además de la rotación normal, mostraron la presencia de peculiaridades cinemáticas con desviaciones de hasta 150 km s^{-1}. A partir de observaciones de las líneas de ^{12}CO, ^{13}CO y ^{18}CO, Weiss et al. (1999) y Matsushita et al. (2000) reportaron evidencia de una superburbuja expandiendose en el lado SW del

núcleo de M82.

El alto nivel de actividad de formación estelar en el centro de M82 podría haber sido iniciado debido a la interacción cercana con la galaxia vecina M81 y la presencia de una barra que llevaría el gas hacia el centro para alimentar el brote de formación estelar. A partir de observaciones de la morfología y la cinemática de los diferentes contituyentes en la parte interna de M82, se ha sugerido la presencia de orbitas x1 y x2 para indicar la existencia de una barra (Achtermann & Lacy 1995; Wills et al. 2000; Greve et al. 2002). En este escenario, el gas ionizado se encuentra principalmente a lo largo de las orbitas x2 i.e. altamente confinado cerca del centro. Las observaciones de rayos-X también sugieren la presencia de un AGN de baja luminosidad (Matsumoto & Tsuru 1999).

La interpretación de las RRLs no es directa ya que el mecanismo de emisión de línea involucra tres contribuciones diferentes: emisión espontanea así como emisiones internamente y externamente estimulada. La emisión de radiocontinuo en las regiones con brote de formación estelar tiene contribuciones de radiación libre-libre (térmica) y sincrotrón (no térmica), lo cual también hace compleja la interpretación de las observaciones. Anantharamaiah et al. (2000) desarrollaron un modelo, basado en la emisión de radiocontinuo y RRL, que consiste de grupos de regiones HII para determinar las propiedades físicas del gas ionizado en Arp 220. Estos autores fueron capaces de reproducir las observaciones en un rango el frecuencias 0.15 − 113 GHz y dedujeron la existencia simultanea de regiones HII extendidas (~5 pc) de baja densidad (~10^3 cm^{-3}) así como de regiones HII compactas (~0.1 pc) de alta densidad (~10^5 cm^{-3}).

En este capítulo presentamos resultados de observaciones hechas con el VLA, con alta resolución angular (1″), de RRLs H92α (3.6 cm) y H53α (7 mm) hacia la galaxia con brote de formación estelar M82. Se identificaron 58 fuentes de radiocontinuo a 8.3 GHz de las cuales 19 no tenían contraparte en catálogos previamente publicados. A 43 GHz identificamos 18 fuentes, no resueltas a una resolución angular de 0″6 de las cuales 5 eran desconocidas anteriormente. La distribución espacial de la línea H92α es inhomogenea; identificamos 27 fuentes con emisión de línea, cerca de la mitad están asociadas con fuentes de emisión de continuo. Sus tamaños están en rangos típicos de 2 a 10 pc. Aunque se observó con baja razón de señal a ruido, se detectó la línea H53α. Se modeló la emisión de RRL y radiocontinuo para diferentes distancias desde el núcleo usando un modelo que consta de diferentes familias de regiones HII. Las observaciones pueden ser interpretadas, usando observaciones previas de radiocontinuo hechas con alta resolución angular para restringir los modelos, a través de dos componentes de gas ionizado con diferente densidad.

Las regiones HII compactas tienen una densidad de $\sim 4 \times 10^4$ cm^{-3}. Sin embargo, la mayor parte de la ionización se lleva a cabo en regiones con densidades típicas que son un factor de 10 más bajas.

La cinemática del gas, usando la línea H92α, confirma la presencia de un gradiente de velocidad pronunciado (26 km s^{-1} arcsec^{-1}) en la región central, como había sido reportado con anterioridad, en particular a partir de observaciones de la línea de [Ne II] a 12 μm. Este gradiente tiene aproximadamente la misma amplitud en ambos lados del núcleo. Ya que este gradiente se observa no solamente en el eje mayor sino también a distancia grandes a lo largo de una banda con P.A. de $\sim 150°$, la interpretación en términos de orbitas x2 orientadas a lo largo del eje menor de la barra, que sería observada a un ángulo cercano a la inclinación del disco principal, parece inadecuada. La cinemática observada no puede ser modelada usando un modelo simple que consiste de orbitas circulares observadas con diferentes ángulos de inclinación. Se deben introducir movimientos radiales *Ad-hoc* para reproducir el patrón observado del campo de velocidades. Se hace evidente la existencia de diferentes familias de órbitas ya que detectamos una característica especial en la cinemática en la transición entre los dos "plateaus" observados en la distribución de luz en el IR cercano. Estos datos de H92α también revelan la base del flujo en donde ocurre la inyección de gas hacia el halo en el lado norte. El flujo tiene un efecto significativo en la cinemática observada, y está presente en el disco aún a distancias cercanas al núcleo. El patrón en la cinemática sugiere una conexión entre el gas que fluye en el plano de M82 hacia el centro; este comportamiento muy probablemente se origina debido a la presencia de la barra y el flujo que sale del plano.

Abstract

We present high angular resolution (0″.6) observations made with the Very Large Array (VLA) of the radio continuum at 8.3 and 43 GHz as well as H92α and H53α radio recombination lines (RRLs) from the nearby (~3 Mpc) starburst galaxy M82. In the continuum we identify 58 sources at 8.3 GHz from which 19 have no counterparts in catalogs published at other frequencies. At 43 GHz we identify 18 sources, unresolved at 0″.6 resolution, from which 5 were unknown previously. The spatial distribution of the H92α line is inhomogeneous; we identify 27 features, about half of them are associated with continuum emission sources. Their sizes are typically in the range 2 to 10 pc. Although observed with poorer signal to noise ratio, the H53α line is detected. The line and continuum emission are modeled using a collection of HII regions at different distances from the nucleus. The

observations can be interpreted assuming a single-density component but equally well with two components, if constraints originating from previous high-resolution continuum observations are used. The high-density component has a density of $\sim 4 \times 10^4$ cm^{-3}. However, the bulk of the ionization is in regions with densities which are typically a factor 10 lower.

The gas kinematics, using the H92α line, confirms the presence of steep velocity gradient (26 km s^{-1} arcsec^{-1}) in the nuclear region as previously reported, in particular from observations of the [Ne II] line at 12 μm. This gradient has about the same amplitude on both sides of the nucleus. As this steep gradient is observed not only on the major axis but also at large distances along a band of PA of $\sim 150°$, the interpretation in terms of x2 orbits elongated along the minor axis of the bar, which would be observed at an angle close to the inclination of the main disk, seems inadequate. The observed kinematics cannot be modeled using a simple model that consists of a set of circular orbits observed at different tilt angles. *Ad-hoc* radial motions must be introduced to reproduce the pattern of the velocity field. Different families of orbits are indicated as we detect a signature in the kinematics at the transition between the two plateaus observed in the NIR light distribution. These H92α data also reveal the base of the outflow where the injection towards the halo on the Northern side occurs. The outflow has a major effect on the observed kinematics, present even in the disk at distances close to the nucleus. The kinematical pattern suggests a connection between the gas flowing in the plane of M82 towards the center; this behavior most likely originates due to the presence of a bar and the outflow out of the plane.

4.1 Introduction

M82 is an excellent candidate to investigate the physical conditions of a starburst galaxy because it is one of the nearest ($\sim$3 Mpc) and brightest objects of this class. The bulk of the ionized gas in this galaxy is located in regions that are surrounded by large amounts of dust: in M82 the extinction in visual magnitudes, A$_V$, ranges from a few to about 15 mag. Radio-wavelength observations, which are not affected by dust obscuration, can play a key role in the determination of the physical properties of the ionized gas in starburst galaxies.

M82 has been observed in the radio continuum over a wide range of frequencies (Kronberg, Biermann & Schwab 1985; McDonald et al. 2002) and is known to host a population of compact sources as observed at angular resolutions $< 0.\!''2$ (McDonald et al. 2002 and references therein). The total number of compact sources decreases at 20 cm as compared to 2 cm; this result has been interpreted as due to free-free absorption by ionized gas in

compact HII regions. Of the 46 compact sources identified by McDonald et al. (2002), ~ 35% were classified as HII regions based on their continuum spectra.

The distribution and kinematics of the ionized gas in the central kiloparsec of M82 have been previously studied using radio recombination lines (RRLs). The first detections of RRLs from M82 (Seaquist & Bell 1977; Chaisson & Rodríguez 1977) were a major achievement that led to further investigations of extragalactic RRLs. VLA observations of RRLs up to 8 GHz by Anantharamaiah et al. (1990) toward NGC 253 motivated further interferometric observations of RRLs at the same frequency (Anantharamaiah et al. 1993; Zhao et al. 1996; Mohan et al. 2002) and higher frequencies (Zhao et al. 2001; Anantharamaiah et al. 2000) toward starburst galaxies. Using the total integrated line emission, global estimates were made for the properties of the ionized gas in M82 (Seaquist, Bell & Bignell, 1985). Using the Westerbork Synthesis Radio Telescope, Roelfsema (1987) obtained the velocity field at moderate angular resolution (~ 13″) using the H166α RRL (at 1.4 GHz). These observations show the rotation of the ionized gas in the central 600 pc, with solid body rotation within a radius of ~ 170 pc or 8″. The velocity field has also been obtained using the [Ne II] line in the mid IR with 2″ angular resolution (Achtermann & Lacy 1995). The velocity fields obtained from the H166α and the [Ne II] line observations are not consistent, specially in the SW half. However, the different angular resolutions achieved for each line prevent a direct comparison. Higher angular resolution observations of RRLs were necessary to understand the kinematics of the ionized gas. Seaquist et al. (1996) observed the H41α line with angular resolution of 4″ and, in addition to the normal rotation, they showed the presence of kinematical features with velocity deviations up to 150 km s^{-1}. From observations of the ^{12}CO, ^{13}CO and ^{18}CO lines, Weiss et al. (1999) and Matsushita et al. (2000) reported evidence for an expanding supershell on the SW side of the nucleus of M82.

The high level of star formation activity at the center of M82 could have been triggered due to the close interaction with the neighboring galaxy M81 and the presence of a bar that would drive the gas inwards to feed the starburst. From observations of the morphology and the kinematics of the different constituents in the inner part of M82, the presence of x1 and x2 orbits has been suggested to indicate the existence of a bar (Achtermann & Lacy 1995; Wills et al. 2000; Greve et al. 2002). In this scenario, the ionized gas is mainly found along the x2 orbits i.e. highly confined near the center. X-ray observations also suggests the presence of a low luminosity AGN in M82 (Matsumoto & Tsuru 1999).

The interpretation of the RRLs is not straightforward since the line emission mechanism

could involve three different contributions: spontaneous as well as internal and external stimulated emission. The radio continuum emission in the starburst regions has contributions from free-free (thermal) and synchrotron (non-thermal) radiation, which also leads to complexity in the interpretation of the observations. Using the radio continuum and RRL observations, Anantharamaiah et al. (2000) developed a model that consists of a collection of HII regions in order to determine the physical properties of the ionized gas in Arp 220. These authors have been able to reproduce the observations in the frequency range 0.15 – 113 GHz and the simultaneous existence of both low density ($\sim 10^3$ cm^{-3}) extended ($\sim$5 pc) HII regions and high-density ($\sim 10^5$ cm^{-3}) ultra-compact ($\sim$0.1 pc) HII regions was deduced.

In this chapter, using the Vey Large Array (VLA) of the National Radio Astronomy Observatory (NRAO), we present observations toward M82 of the radio continuum at 8.3 and 43 GHz and the H92α (3.6 cm) and H53α (7 mm) RRLs. With an angular resolution of 0.''6 ($\sim$9 pc), we can obtain detailed information of the spatial distribution and kinematics of the ionized gas within the central starburst region. In particular we search for continuum emission sources associated with the H92α and H53α line emitting regions.

4.2 Observations

4.2.1 8.3 GHz data

Observations and calibration

The observations of the H92α line (ν_{rest} =8309.3832 MHz) were conducted in the C (April 22, 1996), CnB (Feb 13, 2000) and B (May 05 and 11, 2001) VLA configurations. The maximum angular resolution achieved is $\sim$ 0.''6. The observations made in the C array have been acquired from the VLA archive database. The 31 spectral channels mode was used with a total bandwidth of 25 MHz, corresponding to a velocity coverage of $\sim$850 km s^{-1}, centered at a heliocentric velocity of 200 km s^{-1}. The flux density scale was determined by observing 3C286 (5.3 Jy at 3.6 cm). The phase calibrator was 1044+719, with a flux density of 1.5 Jy. The bandpass calibration was made using the calibrator 3C48 with a flux density of 3.2 Jy. Bandpass calibration is critical in these observations because the line-to-continuum ratios are $\leq$ 1%. The data were Hanning-smoothed offline to improve the signal-to-noise ratio (S/N) and minimize the Gibbs effect. The effective velocity resolution is 56 km s^{-1} (806 kHz). Each of the databases were self-calibrated in phase using the

continuum channel; the solutions were then applied to the spectral line data. The data sets taken at different epochs were combined into a single data set. The self-calibration process was further used on this data set to correct for small phase offsets between the individual observations. The AIPS task UVLSF was used to estimate the continuum level by fitting a linear function through the spectral channels free of line emission, and then subtracted from each visibility record. The observational parameters for the H92α line are listed in Table 4.1.

Imaging

The use of a natural weighting scheme for the data in the C configuration relative to those in the B configuration produces a synthesized beam with prominent wings (at the level of 2%). In order to correct this problem, we use a technique that consists of re-weighting the data in the u,v plane so as to produce a gaussian beam in the image. After the re-weighting process, if necessary, the image is deconvolved using the CLEAN algorithm. Because the u,v plane is properly sampled in the inner region, the deconvolution is not required when producing images at an angular resolution of 2″ FWHM. For the images made at angular resolutions of 0.″6 and 0.″9 (section 4.3), a deconvolution is required. In these cases the 2″ angular resolution image is used as an input for regularization in the process of deconvolution. The quality of the final images is limited by errors due to the imperfect continuum subtraction. These errors appear as weak fluctuations over a scale of one arcmin. These fluctuations have a typical correlation length of about 4 MHz along the spectral axis. This behavior results in systematic errors which limit the quality of the "baselines" ($\sim$ 2%) in the spectra produced from different regions of M82 for our data analysis.

4.2.2 43 GHz data

Observations and calibration

The observations of the H53α line (ν_{rest} =42951.9714 MHz) were carried out in the C array of the VLA on April 13, 2000. The VLA correlator is limited to a bandwidth of 50 MHz ($\sim$350 km s^{-1} at 7 mm). At 43 GHz three adjacent spectral windows, each of them with 15 channels, are required to cover the velocity range of the RRL ($\sim$600 km s^{-1}). The windows were centered at 42185.1, 42214.9 and 42235.1 MHz. The amplitude, phase and bandpass calibrators used were 3C286 (1.47 Jy), 0954+658 (0.87 Jy) and 1226+023 (19.4 Jy), respectively. The flux density calibrator was observed only for the central LO

window (42214.9 MHz). The flux densities of the phase and bandpass calibrators in the adjacent LO windows (42185.1 and 42235.1 MHz) were assumed to have the same values as those determined from the central LO window. The phase calibrator was observed at time intervals of 10 min. The on-source integration time was ~2 hrs for each frequency window. The bandpass response of the instrument is different for each frequency window; the observation of both the bandpass and the phase calibrator must be interleaved between the different overlapping frequency windows required to observe the complete line. This method removes the offsets ($\leq$ 5%) between the frequency windows. In order to correct for phase decorrelation that may be present for time intervals <8 min, a phase calibration was performed initially followed by a second calibration step applied to both phase and amplitude. Phase correction is more important at these frequencies since the troposphere introduces phase offsets that may affect the coherence of the data. The line-to-continuum ratio for this line is 10 – 20% in the brightest region of M82. Table 4.1 shows the details of the observations for the H53α line.

Imaging

In order to produce the H53α line image, the contribution of the continuum emission must be removed and the three frequency windows combined. The method uses two *a priori* constraints on the source model that are not independent. The first constraint is set by assuming that the emission in the lowest spatial frequencies is mostly continuum emission, allowing us to clip the data for the shortest spacings in the u,v plane. The second constraint is based on the fact that the projected velocity of the gas in M82 varies across the image due to the rotation of the galaxy. Hence, if we include *a priori* information on the rotational properties of M82, for each position in the image, we can maximize the number of line-free channels in each LO setting to reduce the uncertainties when removing this contribution. As a result this second method involves the following steps for each LO setting: (1) filter out part of the emission present at the lowest spatial frequencies, (2) produce an undeconvolved 3-dimensional image, (3) determine the level of remaining continuum for each position, (4) determine the offsets by comparing these levels from one LO setting to the other for each position, (5) refine the determination of this remaining continuum by including the line-free channels of the adjacent LO settings for each position, (6) subtract the determined continuum contribution and (7) average the three spectral windows to make the single 3-dimensional line image. It is not necessary to deconvolve the results after step 6 because the signal-to-noise ratio for the line emission is between 2 and 5.

Table 4.1: Parameters of the VLA observations of M82

	H92α (8.3 GHz)	H53α (43 GHz)
Right ascension (B1950)	$09^h51^m42\overset{s}{.}38$	$09^h51^m42\overset{s}{.}51$
Declination (B1950)	$69°54'59\overset{''}{.}2$	$69°55'00\overset{''}{.}0$
Total observing duration (hr)	32	13
Bandwidth (MHz)	25	50×2
Number of spectral channels	31	15×2
Center V_{Hel} (km s^{-1})	200	160
Velocity coverage (km s^{-1})	700	350×2
Velocity resolution (km s^{-1})	56	44
Amplitude calibrator	3C286	3C286
Phase calibrator	1044+719	0954+658
Bandpass calibrator	3C48	1226+023
RMS line noise per channel (mJy beam^{-1})	0.07	1.3-2.0
RMS, continuum (mJy beam^{-1})	0.04	0.5
Configuration	C+CnB+B	C

In order to produce the 43 GHz continuum image we carried out the following steps: (1) produce a raw 3-dimensional image for each LO setting, (2) subtract the line contribution as derived above in each LO setting, (3) determine the mean continuum level for each position in each LO setting, (4) average the three 2-dimensional images obtained in step 3 and also average the three synthesized beams and (5) finally deconvolve this averaged image.

The undeconvolved images were generated using the AIPS IMAGR program applying the suitable u,v tapers to obtain images at different angular resolutions. They were further processed in the GIPSY environment to perform all the subsequent steps. The data were Hanning-smoothed offline and a final spectral resolution of 44 km s^{-1} was achieved.

4.3 Results

Globally, from the 8.3 GHz data, we obtain a total integrated continuum flux density of 2.6±0.1 Jy and a H92α line flux density of 2.9±0.1 Jy km s^{-1}. At 43 GHz the total continuum flux density is in this case 0.82±0.16 Jy and the H53α line flux density is 3.0±0.2 Jy km s^{-1}. Images at three different resolutions are produced to analyze the data. The high angular resolution (0$\overset{''}{.}$6) images are suitable to investigate the compact bright features. Using the intermediate resolution images (0$\overset{''}{.}$9), it is possible to study the weak extended features with sufficient angular resolution. The low angular resolution images (2$''$) provide information on the overall distribution of the ionized gas.
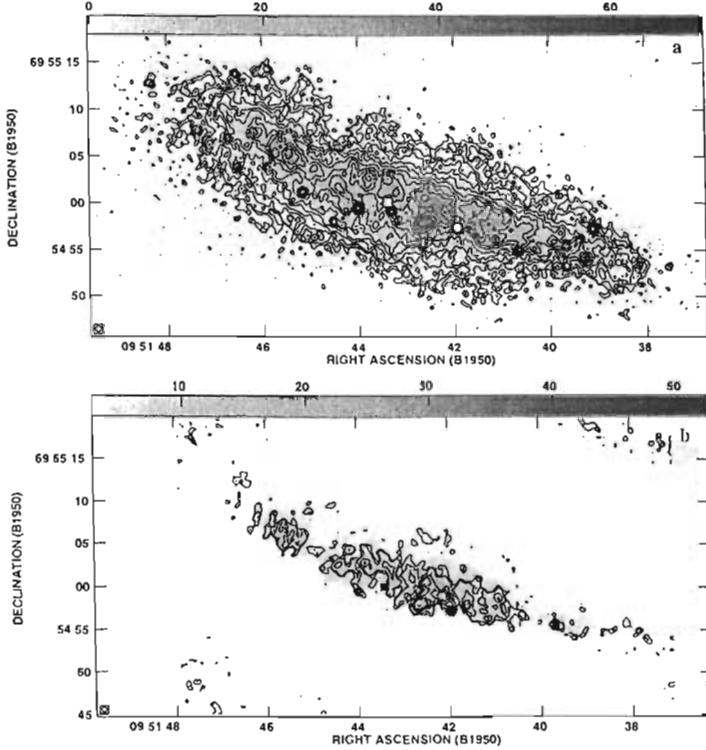
Figure 4.1: a) Radio continuum images at 8.3 GHz made with the VLA in the B and C arrays. Contour levels are drawn at -3, 3, ..., 269 times the rms noise of 0.07 mJy beam^{-1} at steps of $2^{1/2}$. The gray scale covers the range from 0 to 70 mJy beam^{-1}. b) Radio continuum images at 43 GHz made in the C array of the VLA. Contour levels are -3, 3, 4, 6, 8, 10 times 0.4 mJy beam^{-1}, the rms noise in the central regions. The gray scale image covers the range from 3 mJy beam^{-1} to 53 mJy beam^{-1}. In both images, the radio continuum made with high angular resolution of 0.''6 (contours) is superposed on the radio continuum image with low angular resolution of 2'' (gray scale). The square shows the position of the 2.2 μm peak (Lester et al. 1990) and the circle marks the position of the SNR G41.95+57.5.

4.3.1 Radio continuum at 8.3 and 43 GHz

A correction for the primary beam was applied to the images at 8.3 GHz and 43 GHz. In the images at 8.3 GHz this correction does not exceed ~2%, while for the 43 GHz images this correction is a factor of 1.2 at the extreme edges of M82. The radio continuum images at 8.3 and 43 GHz are shown in Fig. 4.1a and Fig. 4.1b, respectively; the high angular resolution images (contours) are shown overlaid on their corresponding low angular resolution images (gray scale) at each frequency.

A number of previous high angular resolution (≤ 0.1'') studies carried out over the range 408 MHz to 15 GHz have revealed the existence of a population of compact sources classified as HII regions or SNRs (Kronberg, Biermann, & Schwab (1985), Huang et al. 1994,

Muxlow et al. 1994, Wills et al. 1997, Allen & Kronberg 1998, McDonald et al. 2002). In order to study the small scale continuum features at 8.3 GHz, the underlying extended emission was filtered out by restricting the lower uv-baseline range (to u,v distances larger than 50 kλ) so that no structures larger than 4″ are present. At 43 GHz an iterative procedure is used to determine and remove the spatially extended continuum emission. Figures 4.2a and 4.2b show the resulting spatial distribution of these features at 8.3 and 43 GHz, respectively. In these images we are able to identify ∼ 85% of the previously known compact sources. The remaining 15% of compact sources were not detected because their peak flux density is below the level of the local diffuse emission. On the other hand, these images reveal 21 new features (19 of these sources are detected at both frequencies and two sources only at 43 GHz) not detected in previous studies. Several of these sources are relatively more extended (> 0″.5) and they could not be identified in the previous high angular resolution images. Including our new detections, a total of 60 sources are detected toward M82, 58 features at 8.3 GHz and 18 at 43 GHz.

In Table 4.2 we list the parameters of these 60 compact features:

- The first column lists the galactic names for each source assigned based on their positions measured from previous higher angular observations. For each feature we measure its spatial position, its deconvolved angular size and flux density. The measurements at 8.3 GHz are summarized in columns 2, 3 and 4 and those at 43 GHz in columns 5, 6 and 7, respectively. For the 21 newly detected features a super-script "a" is used. The uncertainties in flux densities correspond to a 1 σ_{rms} noise in the least-squares fitting procedure. For features not detected, we provide an upper limit of 3 σ_{rms} for the flux densities.

- From the measured flux densities (columns 4 and 7) we derive the spectral index (column 8) between 8.3 and 43 GHz. This value can be compared with the spectral index previously reported in the literature (column 9) using different frequency ranges (e.g. 0.408 to 15 GHz).

- In column 10 we list identifications for the sources based on the radio recombination line emission images. The associations are made with the H92α line features observed at 0″.9 (see section 4.3.2). At an angular resolution of 0″.6, only four H92α compact line features are detected with signal-to-noise ratio > 3 (see section 4.3.2 and Fig 4.3).

- In the last column, the classification is given (HII regions or SNR). The sources previously identified as HII regions by McDonald et al. (2002) were classified based on
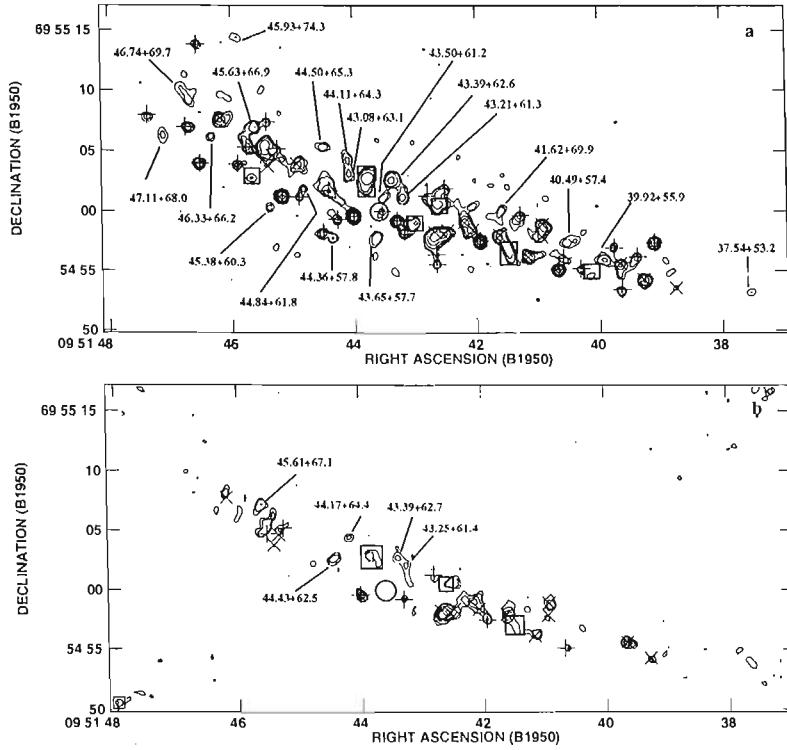
Figure 4.2: Radio continuum images after subtracting the background local emission. (a) 8.3 GHz image (B and C arrays). Contour levels are -3, 3, 6, 12, 24, 48, 96 times the rms noise of 0.04 mJy beam^{-1}. (b) 43 GHz image (C array). Contour levels are drawn at -3, 3, 4, 6, 8, 10 times the rms noise of 0.4 mJy beam^{-1}. Both images have angular resolution of 0."6. The crosses (+) indicate the position of SNRs, while the rotated crosses (X) indicate the HII regions (McDonald et al. 2002). The empty squares show the position of sources previously observed, for which the spectral index has not been determined. The empty circle marks the position of the 2.2 μm peak (Lester et al. 1990). The newly detected features are labeled according to their positions (e.g. 39.92+55.9).

their spectral indexes, α, which in these cases are inverted ($S_\nu \propto \nu^\alpha$, $\alpha > 0$) between 5 and 15 GHz (column 9). We confirm the classification for all the HII regions previously reported, as they have a spectral index that is consistent with optically thin free-free emission between 8.3 and 43 GHz (column 8). We assign tentatively an HII type to four more features, because between 8.3 and 43 GHz, 43.21+61.3 and 45.63+66.9 have flat spectra and 44.17+64.4 and 44.43+62.5 have inverted spectra. For the sources previously identified as SNRs, our results show non-thermal spectra between 8.3 and 43 GHz (see column 8) as expected from the spectral index computed between 5 and 15 GHz. In addition to those features previously classified as SNRs, based on the upper limits obtained from the spectral index between 8.3 and 43 GHz, we can ten-
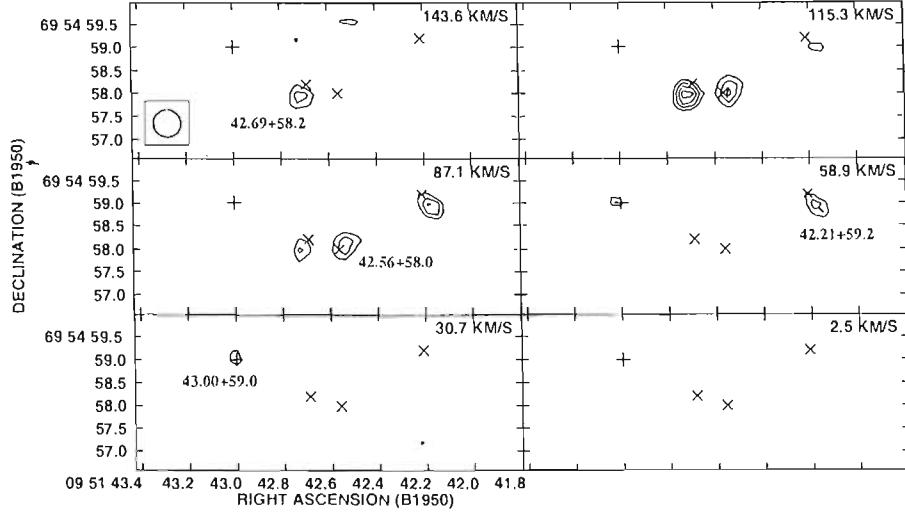
Figure 4.3: High angular resolution images of the H92α line emission (contours) throughout the velocity region where emission was observed in the central region of M82. The beam size is 0."6, shown in the bottom left corner of the first image. The contour levels are -3, 3, 4, 5, 6 times the rms noise of ~0.12 mJy beam^{-1}. The central heliocentric velocity is given above each image. The cross (+) indicates the position of the compact source 43.00+59.0, classified in this work as SNR (see discussion in section 4.5), and the rotated crosses (X) indicate the HII regions; all of these are compact sources observed in the continuum (McDonald et al. 2002; Huang et al. 1994) and coincide with features observed in the H92α line.

tatively consider 39.92+55.9, 40.49+57.4, 43.00+59.0, 44.11+64.3 and 46.74+69.7 as SNRs. It is noted that three SNRs, 41.29+59.7, 43.00+59.0 and 45.79+65.2, exhibit H92α RRL emission; this issue will be discussed in § 4.5.2.

4.3.2   Radio Recombination Lines H92α and H53α

Figure 4.3 shows the high-resolution (0."6) H92α line images in the region where H92α RRL emission is detected; in these images four sources are clearly identified. The center of this region is located ~4" W of the 2.2 μm peak (Lester et al. 1990) and corresponds to the brightest area observed in the H92α line in M82 on a larger scale. All four line emitting sources are spatially associated with compact continuum sources previously identified by McDonald et al. (2002). No other line features are detected outside this region at this resolution. For Figure 4.4 we show the velocity-channels at an intermediate angular resolution of 0."9 (top) and an image of the total integrated H92α line emission (bottom). In this case 27 line features can be identified and those associated with continuum sources are listed in column (10) of Table 4.2. In these images, the position of the HII regions (crosses) and

SNRs (stars) are shown as reported by McDonald et al. (2002). In this comparison the SNRs are mainly located at the periphery of the line emitting regions while the HII regions are clearly associated with the RRL emission. Because these HII regions are the compact continuum sources which have inverted spectra between 5 and 15 GHz (section 4.3), we have direct evidence that this population of compact objects is associated with the more extended HII regions which produce the H92α recombination line emission. Figure 4.5 (top) shows the H92α line velocity-channels at a low angular resolution of 2″ (top) for the overall distribution of the integrated H92α line emitting regions (bottom).

Figures 4.6a and 4.6b show the low-resolution images of the integrated H92α and H53α line emission (contours) overlaid on the low-resolution images of radio continuum at 8.3 and 43 GHz (gray scale), respectively. To produce these images for the integrated line emission only the regions with line emission > $3\sigma_{rms}$ were selected. There is a clear correspondence between the spatial distribution of the line and the continuum emissions. In both cases the distribution of the total line emission is characterized by a pair of concentrations on each side of the center defined by the 2.2 μm peak (Lester et al. 1990). However, the sources located on the E side are fainter compared with their counterpart on the W side. This asymmetry has also been observed in [Ne II] and for several molecules (Achtermann & Lacy 1995). Figure 4.6c shows the velocity integrated line emission of the H53α line (contours) overlaid on the corresponding image of the H92α line (gray scale). A good correspondence between the spatial distributions for the two lines is observed. Both lines cover an angular size of about 30″ (480 pc) along the major axis and the main peak is ∼ 4″ W of the 2.2 μm peak. However, we note that the H92α line emission may be more extended than the H53α line emission (∼ 4″) on the extreme NE side of M82. More sensitive H53α line observations would be required to verify this possible difference. In order to characterize the physical properties of the ionized gas in M82 (section 4.4), we define five regions (E1, E2, C, W1 and W2) as indicated by the rectangular boxes in Figure 4.6c. Regions E1, W1 and W2 have been labeled according to peaks observed in [Ne II] emission (Achtermann & Lacy 1995). The comparison of the distribution of the H92α line emission with the distribution of other tracers of the ionized gas is discussed in § 4.5.2.

Figure 4.7 shows the spatially integrated H92α and H53α spectra for four distinct regions (E1, E2, W1 and W2); the spectrum for region "C" is not shown since H53α line emission is not detected above $3\sigma_{rms}$. The area for the integration of line and continuum emission are defined by the first contour (57 Jy beam^{-1} m s^{-1}) of the H53α distribution. The H92α and H53α line parameters derived from the fits of gaussian profiles (Figure 4.7)

are given in Table 4.3. Columns (2), (3) and (4) of Table 4.3 list the parameters obtained for the RRL H92α and column (5) the continuum flux density at 8.3 GHz. Columns (6), (7) and (8) list the parameters obtained for the RRL H53α, column (9) the continuum flux density at 43 GHz, column (10) the maximum filling factor for the high-density component explained in § 4.4 and column (11) the continuum flux density at 5 GHz (personal communication, A. Pedlar). These measurements form the basis for the models discussed in § 4.4.

The global properties for the five regions identified in Figure 4.6c are given in Table 4.4, the total H92α line emission integrated over each rectangular box (column 2) and the corresponding line (H92α) to continuum (at 8.3 GHz) ratio (column 3). Inside these four regions a number of sub-regions have been identified in the H92α line image (see Table 4.4). For each of these sub-regions (labeled in column 4), Table 4.4 lists the spatial coordinates (column 5), the velocity-integrated line emission (column 6), the FWHM angular size deconvolved to correct for the 0″9 beam broadening (column 7), the peak flux density (column 8), centroid velocity (column 9) and the spectral width (column 10). The angular size of each sub-region is based on fits of 2D gaussians in the appropriate spectral channels; the spectral line parameters were obtained fitting a gaussian profile along the spectral axis for the spatially integrated emission in each of these sub-regions. For each region the sum of the line flux densities of the sub-regions is also given and can be compared with the total line flux density in column 2, determined from the low angular resolution image. For all regions, essentially all the line flux density arises from these sub-regions. Thus, any diffuse emission is ≤ 10%.

The velocity field determined using the H92α line image at 2″ angular resolution is shown in Figure 4.8a. In this image, the major and minor axis are indicated for a disk with a diameter of 40″ as observed at an inclination of 81°, and position angle (PA) of 68° relative to the observer. The intersection of these two axes is set at the position of the 2.2 μm peak (Dietz et al. 1986), which also coincides with the center of the hole in Fig. 5b. The position of the center of the ring fitted by Achtermann & Lacy (1995), assumed to be the kinematic center, is indicated by a cross. The important features in this velocity field are the following: *a)* The major axis corresponds to the line of nodes which gives the maximum velocity gradient for the outer regions, *b)* in the central region there is a significant tilt of the iso-velocities relative to the PA of the minor axis, *c)* this velocity field is dominated by an axisymmetric pattern and the position of the center of symmetry appears to have a small offset (~ 1″5) relative to the position of the 2.2 μm peak, *d)* Some areas show significant

Table 4.2: CONTINUUM FLUX DENSITIES, COMPACT FEATURES.

Source ID[1]	Coordinates[1]	Size[2] ('')	$S_{8.3}$ (mJy)	Coordinates[1]	Size[2] ('')	S_{43} (mJy)	Spectral index 8.3-43 GHz	Spectral index Low freq.	RRL feature	Type
(1)	(2)	(3)	(4)	(5)	(6)	(7)	(8)	(9)	(10)	(11)
37.54+53.2	37.54+53.2[a]	0.5[g]	0.43±0.03	–	–	<1.5	<0.74	–	--	
38.76+53.4	38.75+53.5[b]	0.5[g]	0.24±0.07	–	–	<1.5	<1.1	0.54±0.27[d]	–	HII[f]
39.10+57.3	39.11+57.3[b]	u	3.81±0.04	–	–	<1.5	< -0.55	-0.53±0.09[d]	–	SNR[f]
39.29+54.2	39.27+54.1[b]	0.4	3.6±0.1	39.25+54.1[b]	0.5	3.5±0.3	-0.02±0.02	1.64±0.16[d]	–	HII[f]
39.40+56.1	39.43+55.9[b]	0.5	1.9±0.1	–	–	<1.5	< -0.14	-1.04±0.22[d]	–	SNR[f]
39.64+53.4	39.65+53.2[b]	u	1.0±0.05	–	–	<1.5	<0.24	-0.20±0.05[c]	–	SNR[f]
39.68+55.6	39.67+55.3[b]	0.4	3.9±0.2	39.66+55.4[b]	0.5	3.6±0.5	-0.05±0.09	1.03±0.09[d]	–	HII[f]
39.77+56.9	39.78+56.9[b]	0.4	0.7±0.05	–	–	<1.5	<0.45	-0.50±0.06[c]	–	SNR[f]
39.92+55.9	39.92+55.9[a]	0.7	2.7±0.1	–	–	<1.5	< -0.35	–	–	SNR?[e]
40.10+55.0	40.15+54.5[b]	0.7	0.6±0.05	–	–	<1.5	<0.54	–	–	
40.32+55.1	40.33+55.1[b]	0.4	0.8±0.04	–	–	<1.5	<0.37	-0.23±0.21[d]	--	SNR[f]
40.49+57.4	40.49+57.4[a]	1.0	2.7±0.1	–	–	<1.5	< -0.35	–	–	SNR?[e]
40.62+56.0	40.63+56.0[b]	0.5	1.7±0.1	–	–	<1.5	< -0.01	-0.72±0.25[d]	–	SNR[f]
40.66+55.2	40.67+55.1[b]	0.4	5.6±0.1	40.65+55.1[b]	0.5	2.7±0.1	-0.43±0.05	-0.54±0.08[d]	–	SNR[f]
40.95+58.8	40.93+58.7[b]	0.5	4.5±0.4	40.92+58.7[b]	0.5	3.9±0.2	-0.09±0.06	0.44±0.13[d]	W2h	HII[f]
40.96+57.9	40.96+57.8[b]	u	2.3±0.2	40.96+57.6[b]	0.5	1.8±0.1	-0.15±0.05	>1.2[d]	–	HII[f]
41.17+56.2	41.17+56.1[b]	0.4	5.4±0.2	41.16+56.2[b]	0.7	4.9±0.4	-0.06±0.03	0.87±0.14[d]	W2f	HII[f]
41.29+59.7	41.33+59.2[b]	0.7	3.0±0.2	–	–	<1.5	< -0.41	-0.47±0.09[d]	W2e	SNR[f]
41.62+59.9	41.62+59.9[a]	0.5	1.6±0.1	–	–	<1.5	< -0.04	–	–	
41.95+57.5	41.95+57.4[b]	u	13.6±0.4	41.95+57.5[b]	0.7	5.0±0.1	-0.60±0.02	-0.80±0.05[c]	–	SNR?[f]
42.08+58.4	42.11+58.3[b]	0.4	4.0±0.2	42.09+58.3[b]	0.5	3.6±0.2	-0.06±0.04	1.32±0.17[d]	–	HII[f]
42.21+59.0	42.20+59.0[b]	0.5	6.7±0.1	42.21+59.0[b]	0.7	6.5±0.3	-0.02±0.03	1.16±0.13[d]	W1f	HII[f]
42.67+55.6	42.67+55.5[b]	u	0.92±0.04	–	–	<1.5	<0.29	-1.3±0.2[d]	–	SNR[f]
42.69+58.2 ⌈								⌉ 1.04±0.13[d]	W1c	HII[f]
42.56+58.0 ⎢	42.64+57.9[b]	~1.4	32.4±0.7	42.64+57.9[b]	~1.2	16.2±0.8	-0.41±0.2	⎢ 0.88±0.14[d]	W1c	HII[f]
42.48+58.4 ⌊								⌋ >1.2[d]	W1c	HII[f]
43.00+59.0	43.02+58.9[b]	0.4	3.9±0.2	–	–	<1.5	< -0.56	–	W1a	SNR?[e]
43.18+58.3	43.17+58.3[b]	u	5.5±0.1	–	–	<1.5	< -0.77	-0.44±0.08[d]	–	SNR[f]
43.21+61.3	43.21+61.3[a]	0.8	4.3±0.1	43.25+61.4[a]	1.3	4.0±0.3	-0.04±0.05	–	–	HII?[e]
43.31+59.2	43.29+59.0[b]	u	8.0±0.2	43.30+59.2[b]	0.4	2.0±0.2	-0.83±0.06	-0.65±0.07[d]	–	SNR[f]
43.39+62.6	43.39+62.6[a]	0.7	7.0±0.2	43.39+62.7[a]	0.8	3.9±0.2	-0.34±0.14	–	Cd	
43.50+61.2	43.50+61.2[a]	0.5	2.2±0.1	–	–	<1.5	< -0.23	–	.	
43.55+60.0	43.57+59.8[b]	0.4	0.77±0.05	–	–	<1.5	<0.40	–	–	
43.65+57.7	43.65+57.7[a]	0.7	2.3±0.1	–	–	<1.5	< -0.25	–	–	
44.01+59.6	44.02+59.5[b]	0.4	19.5±0.2	44.01+59.5[b]	0.4	4.5±0.4	-0.87±0.05	-0.38±0.06[d]	–	SNR[f]
44.08+63.1	44.08+63.1[a]	0.8	4.1±0.1	–	–	<1.5	< -0.60	–	–	

44.11+64.3	44.11+64.3^a	0.5	2.1±0.1	–	–	<1.5	< −0.20	–	–	SNR?^e
44.17+64.4	–	–	< 0.24	44.17+64.4^a	0.8	4.1±0.2	> 1.74	–	–	HII^e
44.29+59.3	44.28+59.3^b	u	2.3±0.1	–	–	<1.5	< −0.25	−0.72±0.12^d	–	SNR^f
44.36+57.8	44.36+57.8^a	0.4	1.5±0.1	–	–	<1.5	<0.0	–	–	
44.43+62.5	–	–	< 0.24	44.43+62.5^a	0.9	5.5±0.2	> 1.91	–	E1b	HII^e
44.50+65.3	44.50+65.3^a	0.5	1.4±0.1	–	–	<1.5	<0.0	–	–	
44.52+58.1	44.52+58.0^b	0.4	2.1±0.05	–	–	<1.5	< −0.20	−0.15±0.17^d	–	SNR^f
44.84+61.8	44.84+61.8^a	u	0.95±0.05	–	–	<1.5	<0.27	–	–	
44.91+61.1	44.89+61.2^b	u	1.2±0.1	–	–	<1.5	<0.13	−0.45±0.18^d	–	SNR^f
44.93+63.9	44.92+63.7^b	0.7	3.6±0.1	–	–	<1.5	< −0.52	>1.1^d	E2f	HII^f
45.17+61.2	45.19+61.1^b	0.4	6.7±0.1	–	–	<1.5	< −0.89	−0.52±0.07^d	–	SNR^f
45.38+60.3	45.38+60.3^a	0.4	1.1±0.05	–	–	<1.5	<0.19	–	–	
45.44+67.3	45.44+67.3^b	0.4	1.47±0.06	–	–	<1.5	<0.0	–	–	
45.63+66.9	45.63+66.9^a	0.8	5.8±0.2	45.61+67.1^a	0.9	5.5±0.4	−0.04	–	E2c	HII^e
45.70+62.9	45.66+62.8^b	0.4	0.78±0.05	–	–	<1.5	<0.39	–	–	
45.79+65.2	45.74+65.5^b	0.5	5.9±0.2	–	–	<1.5	< −0.81	−0.55±0.13^d	E2b	SNR^f
45.91+63.8	45.88+63.7^b	0.4	1.28±0.05	–	–	<1.5	<0.01	−0.38±0.11^d	–	SNR^f
45.93+74.3	45.93+74.3^a	1.0	1.4±0.1	–	–	<1.5	<0.01	–	–	
46.17+67.6	46.17+67.6^b	0.8	4.6±0.1	46.21+67.8^b	0.8	4.5±0.3	−0.02±0.04	0.66±0.16^d	E2a	HII^f
46.33+66.2	46.33+66.2^a	u	0.93±0.05	–	–	<1.5	<0.28	–	–	
46.52+63.8	46.53+63.9^b	0.4	2.1±0.1	–	–	<1.5	< −0.20	−0.35±0.11^d	–	SNR^f
46.56+73.8	46.57+73.7^b	u	0.76±0.05	–	–	<1.5	<0.40	−0.60±0.05^c	–	SNR^f
46.74+69.7	46.74+69.7^a	1.4	4.3±0.2	–	–	<1.5	< −0.63	–	–	SNR?^e
46.75+67.0	46.69+66.9^b	0.4	1.8±0.1	–	–	<1.5	<0.11	−0.80±0.05^c	–	SNR^f
47.11+66.3	47.11+66.3^a	0.5	1.12±0.05	–	–	<1.5	<0.17	–	–	
47.37+68.0	47.37+67.8^b	0.4	0.7±0.05	–	–	<1.5	<0.45	−0.60±0.07^c	–	SNR^f

[1] Relative to $\alpha(B1950)= 09^h 51^m 00^s$, $\delta(B1950) = 69°54'00''$.

[2] Deconvolved angular size from the 0.6″ HPBW. With this resolution the sources which appear unresolved are indicated by "u".

[a] Sources newly identified in this work.

[b] From Kronberg et al. (1985), Bartel et al. (1987), Huang et al. (1994), Muxlow et al. (1994), Wills et al. (1997), McDonald et al. (2002).

[c] Spectral index ($S \propto \nu^\alpha$) between 1.4, 5 and 8.4 GHz (Wills et al. 1997).

[d] Spectral index ($S \propto \nu^\alpha$) between 5 and 15 GHz (McDonald et al. 2002).

[e] Source type obtained in this work based on the spectral index in column 8.

[f] Source type given by McDonald et al. (2002).
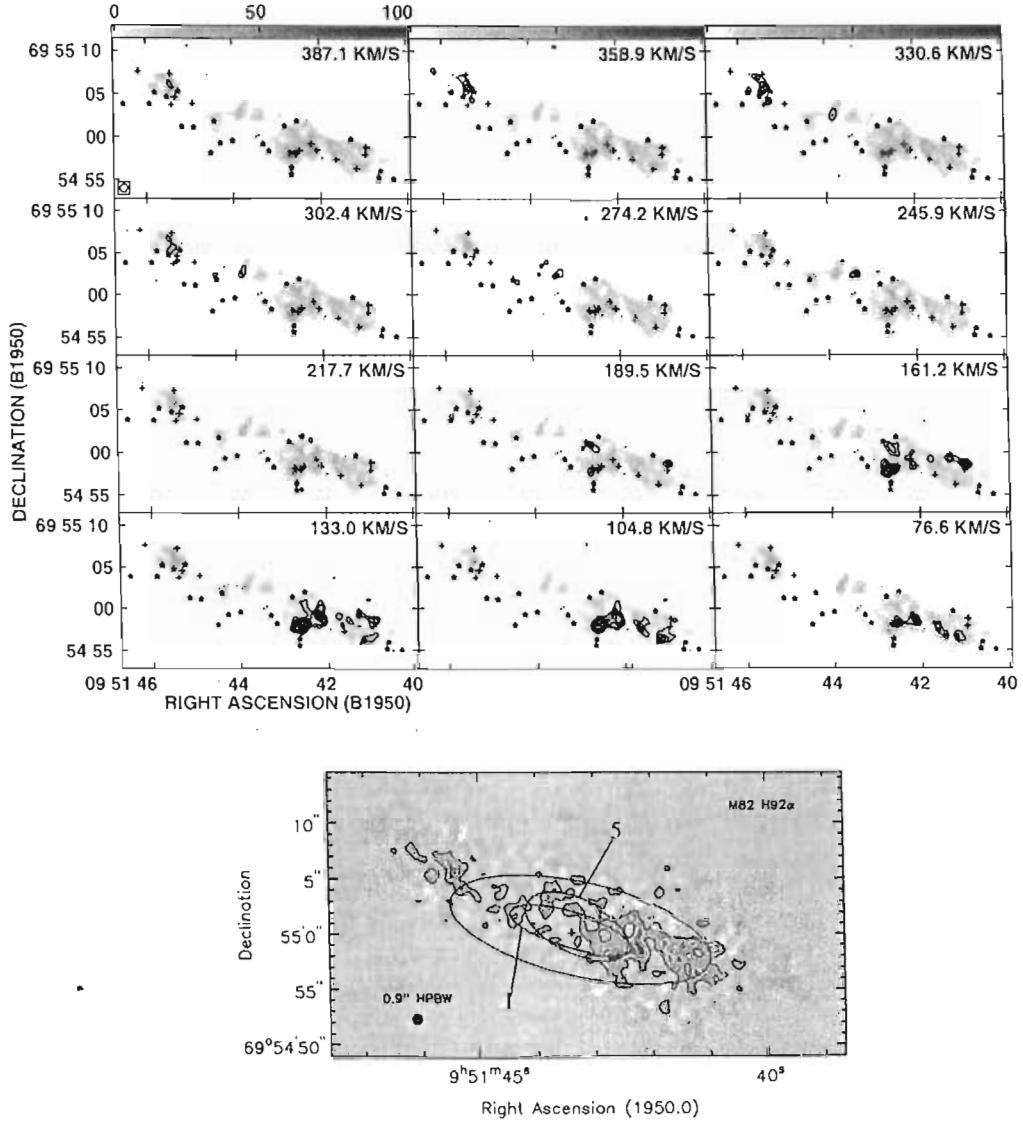
Figure 4.4: Top) Contour images of the H92α line intensity throughout the velocity region where emission was observed at intermediate-resolution (0″9). The contour levels are −3, 3, 4, 5, 6, 7, 8, 9 times the rms noise of ~0.07 mJy beam^{-1}. The integrated line emission obtained from the low-resolution (2″) line images is shown in gray scale. The gray scale image covers the range from 0 to 6 Jy beam^{-1} m s^{-1}. The marks indicate the position of the HII regions (crosses) and the SNRs (stars). The central heliocentric velocity is given above each image. The beam size is shown in the bottom left corner of the first image. Bottom) Integrated H92α line emission at 0″9 angular resolution toward M82. Contour levels are 0.4, 0.8, 1.2, 1.6, 2.0 mJy beam^{-1} km s^{-1}. The cross indicates the 2.2 μm peak (Lester et al. 1990). The outer ellipse shows the extension of the inner 2.2 μm plateau. The ellipses shown correspond to models of Table 4.6 in row 1 and 5, respectively.
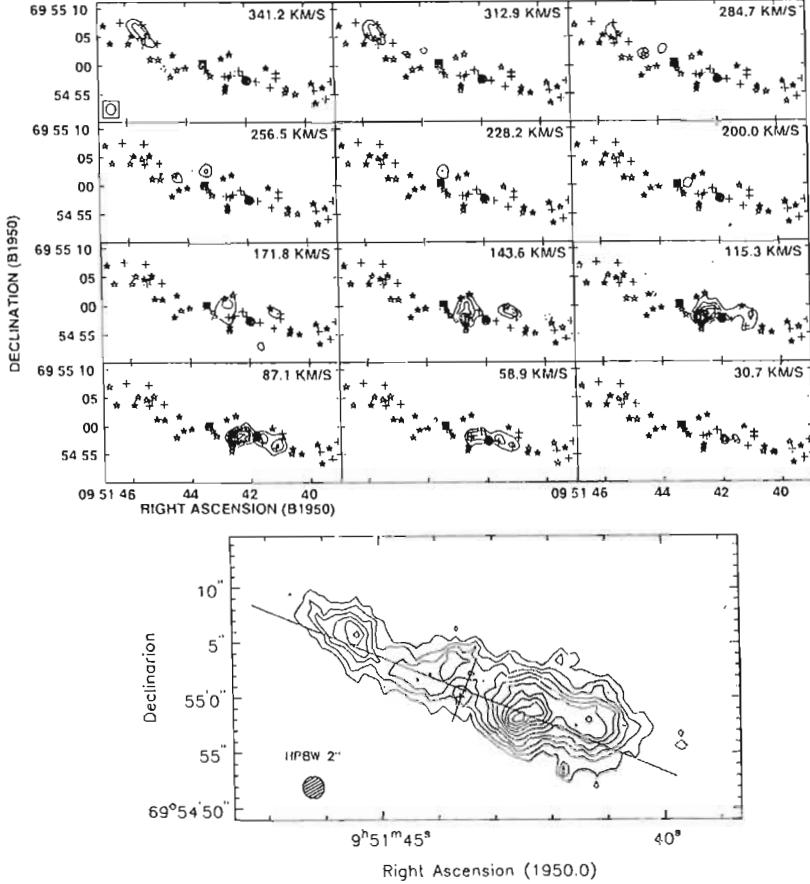
Figure 4.5: Top) Contour images of the H92α line at low angular resolution (2″). The contour levels are −3, 3, 5, 7, 9, 11, 13, 15, 17, 19 times the rms noise of ∼0.07 mJy beam⁻¹. The filled circle shows the position of G41.95+57.5 and the filled square the peak at 2.2 μm (Lester et al. 1990). The beam size is shown in the bottom left corner of the first image. Bottom) Integrated H92α line emission at 2″ angular resolution toward M82. Contour levels are from 15.82 up to 158.2 by increment of 15.82 mJy beam⁻¹ km s⁻¹. The two line segments show the minor and major axis of a thin disk which would be observed with an inclination of 81° and centered at the position of the 2.2 μm peak (Dietz et al. 1986). The cross indicates the 2.2 μm peak (Lester et al. 1990).

deviations relative to this general pattern, in particular in the region near $9^h51^m43^s5$, +69° 55′04″, where the velocities are ∼ 40 km s⁻¹ larger than expected. The kinematics of the ionized gas are discussed in § 4.5.3. The spatial distribution of the velocity dispersion is shown in Figure 4.8b. One important feature in this image is the presence of a band ∼ 1″5 wide with a PA of ∼ 150°, close to the minor axis, where the spectra are systematically narrower. This feature is analyzed in section 4.5.3.
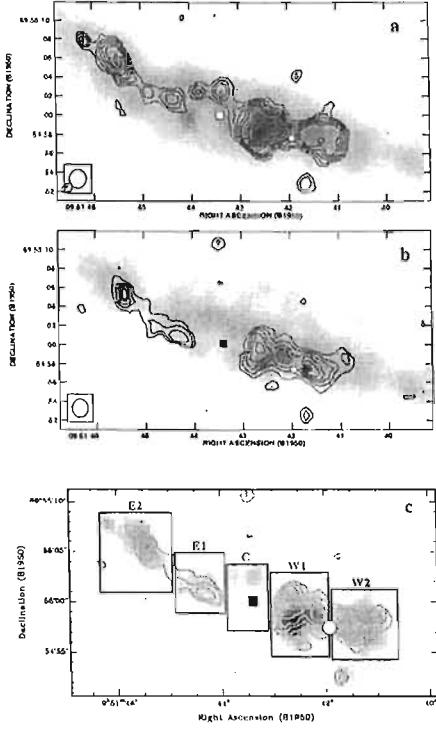
Figure 4.6: a) The integrated H92α line emission (contours) superposed on the radio continuum at 8.3 GHz (gray-scale) at 2″ angular resolution. Contour levels are drawn at 18 through 148 mJy beam^{-1} km s^{-1} in steps of 26 mJy beam^{-1} km s^{-1}. The gray scale for the continuum covers the range from 5.4 to 55 mJy beam^{-1}. b) The integrated H53α line emission (contours) superposed on the radio continuum image of M82 at 43 GHz (gray-scale) at 2″ angular resolution. Contour levels are at 57, 114, 171, 228, 285 Jy beam^{-1} km s^{-1}. The gray scale for the continuum covers the range from 2.3 to 34 mJy beam^{-1}. c) Integrated intensity of H92α line (gray-scale) and integrated intensity image of the H53α line (contours). Contour levels are 57, 114, 171, 228 Jy beam^{-1} km s^{-1}. The gray scale covers the range from 8.4 to 196 mJy beam^{-1} km s^{-1}. The square marks the position of the 2.2 μm peak (Lester et al. 1990) and the circle marks the position of the SNR G41.95+57.5.

4.4 Models with multiple HII regions

In three starburst galaxies (Arp 220, M83, NGC 2146) a model consisting of a collection of HII regions has been used successfully to explain the observations of RRLs and the radio continuum (Anantharamaiah et al. 1993, Zhao et al. 1996, Anantharamaiah et al. 1996, Anantharamaiah et al. 2000). The ionized gas distribution in the center of M82 is inhomogeneous as observed in the RRLs H92α and H53α. Thus, a model that consists of a collection of HII regions seems appropriate to explain the RRL and radio continuum emission from this galaxy. Based on this model we can derive the physical parameters of the
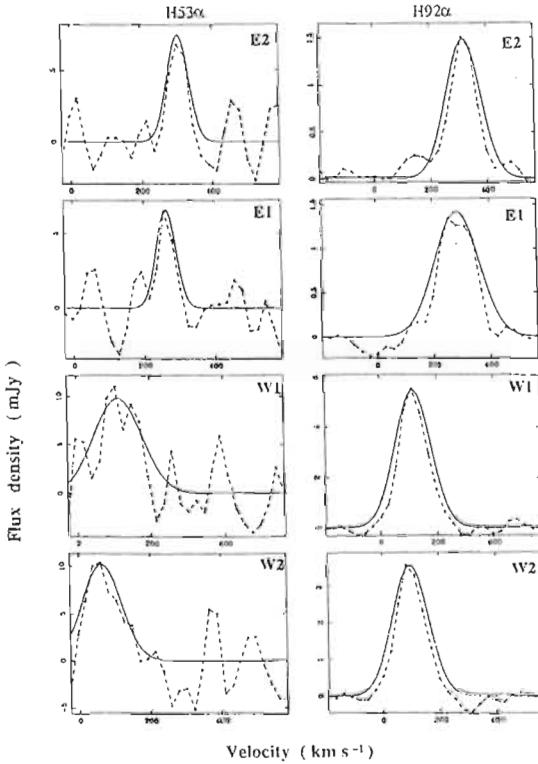
Figure 4.7: H92α and H53α spectra toward the regions labeled in Figure 4.6c. The dashed curves are the observed intensities and the solid lines represent the fitted gaussians as a function of heliocentric velocity.

HII regions (e.g. electron temperature and volume density). The model must reproduce both the observations of the line and continuum emission as a function of frequency. For M82, observations at 2″ angular resolution of RRLs are available at two different frequencies (8.3 and 43 GHz) and observations of radio continuum at three frequencies (5, 8.3 and 43 GHz). The 5 GHz flux densities are listed in column 11 of Table 4.3.

The gas is ionized by young massive stars (types O and/or B) radiating large amounts ($\geq 10^{49}$ s^{-1}) of Lyman continuum photons. The number of Lyman continuum photons determines the size, l, of each HII region depending on the electron density. Since these models are constructed to obtain average values for the physical properties of the ionized gas, we have assumed: (1) Each ionizing massive star emits the same number of Lyman continuum photons ($N_{Lyc} = 10^{49}$ s^{-1}) and (2) N_{Lyc} is related to the electron density and the size of each HII region by $N_{Lyc} \propto n_e^2 l^3$; this relation implies that for each density value, l will be determined and then l is not a free parameter in the model, providing a constraint. Since massive stars have a relatively short lifetime on the main sequence, the derived number of
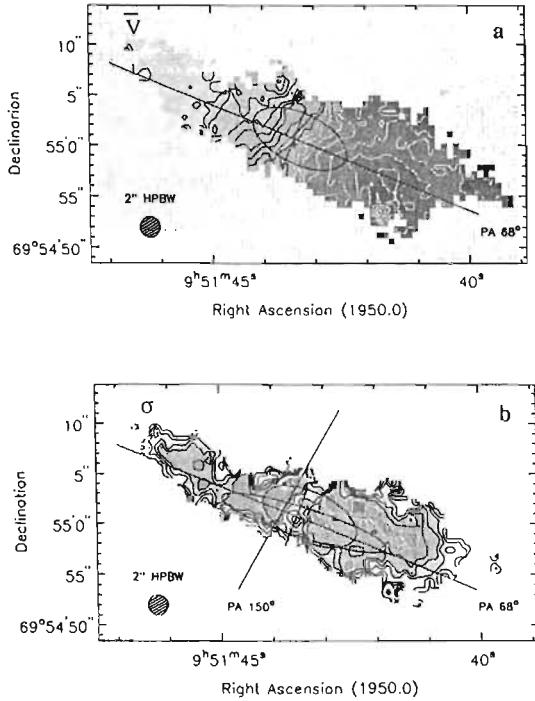
Figure 4.8: a) H92α velocity field at 2″ angular resolution. Contour intervals are 16 km s^{-1}, the iso-velocity contours ≥ 200 km s^{-1} are in black. b) Spatial distribution for the velocity dispersion of the H92α profiles. The contours from 15 to 35 km s^{-1} are in black and above this level in white. The contour interval is 5 km s^{-1}. The most elongated ellipse is a fit to a ridge with minimum velocity dispersion which corresponds to the transition between the inner and outer plateau in the 2.2 μm brightness distribution. In both images, the less elongated ellipse corresponds to the model of row 5 (Table 4.6). The two perpendicular line segments are the same as in Figure 4.5 (bottom). The cross indicates the center of the ring fitted by Achtermann & Lacy (1995).

Lyman continuum photons can be related to the star formation rate (SFR) of O and B stars if the absorption of Lyman continuum photons by dust inside the HII regions is neglected.

This model consists of HII regions located in front of a diffuse mixture of thermal and non-thermal emission (S_{Cbg}). The HII regions radiate free-free emission and recombination lines. Background non-thermal emission and free-free emission that arise inside each HII region may stimulate the emission of RRLs in the HII regions. Thus, the line emission from each HII region has three different contributions: (i) spontaneous, (ii) internally stimulated and (iii) externally stimulated emission. Each HII region is characterized by an electron temperature T_e (K), electron density n_e (cm^{-3}), and linear size l (pc). The thermal continuum flux density, S_{C-TH}, is given by,
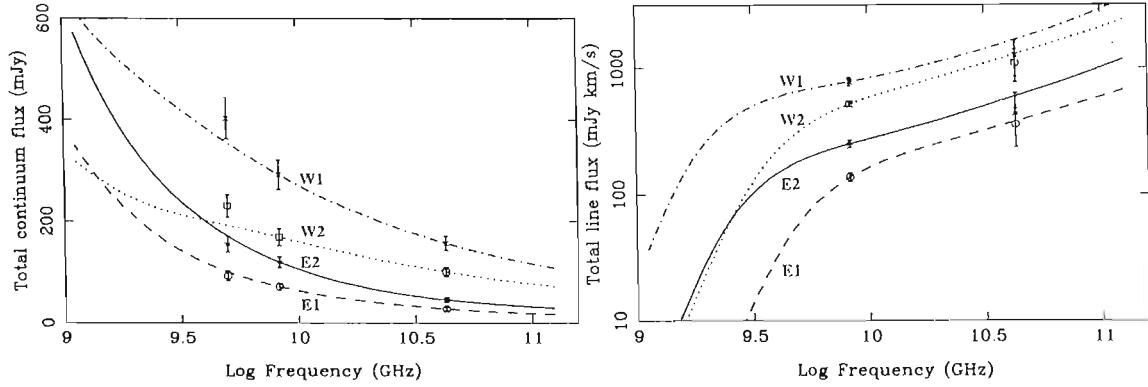
Figure 4.9: Expected variation of radio continuum (left) and integrated line flux density (right) for four of the regions identified in Fig. 4.6c. The continuum flux density has been computed using the model of multiple HII regions with a single component plus non-thermal emission arising from SNR. The integrated line emission curves correspond to the single-density models of Table 4.5.

$$S_{C-TH} = \Omega_{HII} B_\nu (1 - e^{-\tau_c}) \, mJy, \tag{4.1}$$

where Ω_{HII} is the solid angle subtended by each HII region, B_ν is the black-body emission (mJy) and τ_C is the continuum optical depth, which depends on frequency ν_L as follows (Bell & Seaquist 1978):

$$\tau_C = 3.01 \times 10^{-2} \nu^{-2} T_e^{-1.5} ln\left(\frac{4.95 \times 10^{-2} T_e^{1.5}}{\nu_L}\right) EM_C, \tag{4.2}$$

where $EM_C = n_e^2 l$ is the emission measure for each HII region. The line flux density, S_L (mJy), arising from each HII region is calculated using

$$S_L = \frac{2k\nu^2}{c^2} \Omega_{HII} T_e \left[\frac{b_n \tau_L^* + \tau_c}{\tau_L + \tau_c}(1 - e^{-\tau_L + \tau_c}) - (1 - e^{\tau_c})\right] + S_{Cbg} e^{-\tau_c}(e^{-\tau_L} - 1) \, mJy. \tag{4.3}$$

The spontaneous and the internally stimulated emission are represented by the first term in Eq. 4.3 and the externally stimulated emission is represented by the second term. k is the Boltzmann constant, c is the speed of light, τ_L^* is the peak line optical depth under LTE conditions, $\tau_L = b_n \beta_n \tau_L^*$ is the peak line optical depth corrected for non-LTE effects, b_n is the departure coefficient, n is the quantum number, and $\beta_n = 1 - (kT_e/h\nu_L)dlnb_n/dn$. For a given combination of parameters T_e and n_e, we compute the corresponding values of b_n and β_n (Salem & Brocklehurst 1979) which are used to calculate the integrated line flux density
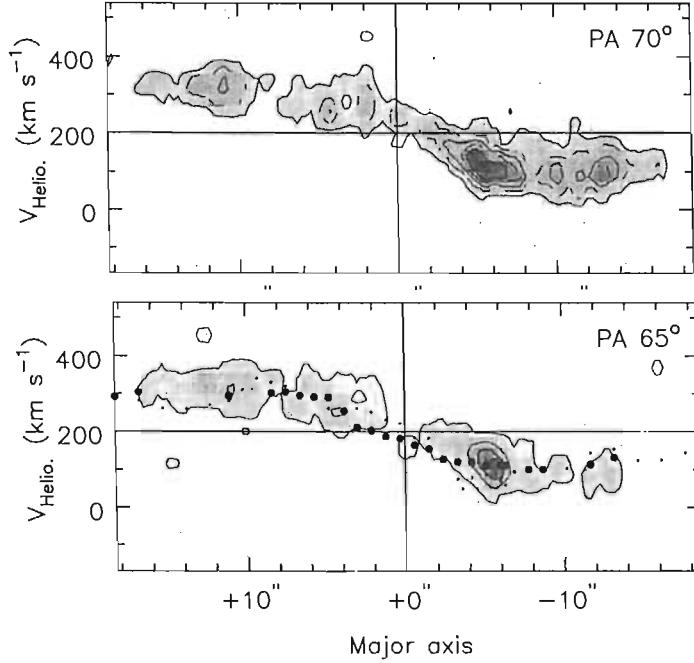
Figure 4.10: H92α position-velocity diagram summed over the minor axis (angular resolution 0."9), along: top) the main axis of the stellar bar with PA=70°. Contours are from 0.3 to 3.0 in steps of 0.6 mJy beam^{-1}, and bottom) the major axis of M82 determined on larger scales with PA=65°. Small circles marks the velocity of the stars as determined from [Ca II] line (McKeith et al. 1993) and big circles show the velocity of the gas determined in Pa(10) line (McKeith et al. 1993). Contours are 0.1, 0.4 and 1.5 mJy beam^{-1}. The beam is 2."5 × 0."9. The gray scales follow the contours. The slices were centered at α=09^{h}51^{m}43.^{s}6, δ=69°55′00″.

of a single HII region using Eq. 4.3. The line optical depth is given by $\tau_L^* = \tau_c S_L / S_{C-TH}$ where the line to thermal continuum ratio in LTE is defined as,

$$\frac{S_L}{S_{C-TH}} = 2.33 \times 10^4 \left(\frac{\Delta \nu_L}{kHz}\right)^{-1} \left(\frac{\nu_L}{GHz}\right)^{-2.1} \left(\frac{T_e}{K}\right)^{-1.15} \frac{EM_L}{EM_C}, \qquad (4.4)$$

where EM_L is the emission measure from hydrogen and EM_C is the emission measure from all ions (cm^{-6} pc). In these models, $EM_L/EM_C = 1$; for simplicity we do not consider the presence of ionized He.

Single-density (SD) models, consisting of a number of HII regions with the same physical properties, have been used to reproduce the observations. Additionally, following Anantharamaiah et al. (2000), two-density (TD) models that consist of both low- and high-density HII regions were used to reproduce the observed values (listed in Table 4.4) for

four regions (E1, E2, W1, W2); in region 'C' the H53α line emission is not detected (see Figure 4.6c). The following constraints have been imposed: (i) the predicted thermal radio continuum flux densities should not exceed the radio continuum flux density observed at 43 GHz, (ii) the area filling factor should be ≤ 1, (iii) the peak line emission from the model should not be larger than the corresponding observations, (iv) the spectral index of the background radiation has been limited to be not steeper than -1.5, (v) the continuum computed from the model must reproduce all continuum observations at 6 cm, 3.6 cm and 7 mm, and (vi) the area filling factor for the high-density component has an upper limit imposed by observations of compact continuum sources at high angular resolution (McDonald et al. 2002). For the two-density models the constraint (vi) is based on the additional assumption that the high-density HII regions are coincident with compact sources previously identified as HII regions. Using the emission measure given in Table 4 of McDonald et al. (2002), we compute the angular sizes and the maximum filling factor for the HII regions that form the high-density component. The models that are consistent with these constraints were accepted as valid solutions.

The number of HII regions for the single-density model is computed by dividing the observed integrated line flux density by the integrated line flux density from a single HII region. In the case of the model with two-density components, the number of HII regions with high-density gas (N_{HII-HD}) is computed dividing the area filling factor derived above by the area filling factor that a single high-density HII region can occupy (following $n_e \propto l^{-3/2}$). Once we know the contribution of the high-density component to the line and continuum emission, the number of HII regions in the low-density component (N_{HII-LD}) can be estimated (see Table 4.5) .

For both the single-density and the two-density models, the contribution from the background emission is computed as the difference between the observed radio continuum at 8.3 GHz and the value predicted by the models for the thermal emission at this frequency. The spectral index value (α), determined for this background emission, is obtained by minimizing the difference between the observed and the predicted values of the thermal continuum flux density at 43 GHz.

Since we have assumed that each HII region is being excited by stars that emit $N_{Lyc} = 10^{49}$ photons per second, the total rate of emission of ionizing photons, $N_{Lyc-tot}$, is,

$$N_{Lyc-tot} = N_{Lyc}N_{HII},$$

(4.5)

Table 4.3: LINE PARAMETERS AT LOW ANGULAR RESOLUTION USED IN THE MODELS.

| | H92α | | | | H53α | | | | | |
Region	Peak Flux (mJy)	V_{HEL} (km/s)	ΔV (km/s)	S_{CB} (mJy)	Peak Flux (mJy)	V_{HEL} (km/s)	ΔV (km/s)	S_{C43} (mJy)	ff^b (10^{-3})	S_{CS} (mJy)
E2	2.2±0.1	315±2	106±5	106±10	7.5±1.5	305±5	55±12	46±17	1.3	152
E1	1.0±0.1	269±3	130±8	72±10	6.7±1.5	264±5	50±13	28±15	--	93
W1	6.4±0.1	119±1	116±3	292±15	9.8±2.0	113±12	120±29	157±20	3.2	403
W2	4.2±0.1	100±2	112±4	169±15	10.2±2.0	66±9	100±22	101±19	6.8	230

Note.– Note that the integrated line flux density for each region is lower than that given in Table 4.4 (col. [2]) since the regions for which we have integrated here are defined by the lowest contour in the H53α integrated line emission image.
[b] Area filling factor computed using Table 4 from McDonald et al. (2002).

where $N_{HII} = N_{HII-LD} + N_{HII-HD}$. Another way to estimate $N_{Lyc-tot}$ is using (Schraml & Mezger 1969, Rodriguez et al. 1980),

$$\left[\frac{N_{Lyc-tot}}{s^{-1}}\right] = 9.0 \times 10^{43}\left(\frac{S_{C-TH}}{mJy}\right)\left(\frac{Te}{10^4\,K}\right)^{0.35}\left(\frac{\nu}{4.9\,GHz}\right)^{0.1}\left(\frac{D}{kpc}\right)^2, \qquad (4.6)$$

where we can use the flux density from thermal emission, S_{C-TH}, at any frequency (if $\tau_C \ll 1$) and D, the distance to the galaxy. In the case of optically thin emission at 43 GHz, both estimates of N_{Lyc} give similar values. However, the model is based on a number of assumptions. On the other hand, the number of Lyman continuum photons is proportional to the radio continuum at 43 GHz and does not depend on extinction estimation as occurs for the near-infrared case. Thus, the determination of the number of Lyman continuum photons from the continuum at 43 GHz is the most reliable way to estimate the Lyman continuum photons production. If the gas is optically thick (which may be the case for a high-density component) at 43 GHz, then the estimation of the total number of ionizing photons using Eq. 4.5 is a lower limit. The total SFR can be derived from the Lyman continuum luminosity following Anantharamaiah et al. (2000).

4.4.1 Results from the models

The parameters T_e and n_e were considered to lie in the ranges $5000 - 10,000$ K (Garay & Rodríguez 1983) and 500-10^6 cm^{-3}, respectively. The low-density component was defined to consist of HII regions with electron density, n_e in the range $100-10^4$ cm^{-3}, while the high-density component was defined as composed of HII regions with n_e in the range $2 \times 10^4 - 10^6$ cm^{-3}. In Table 4.5 we list the range of physical parameters estimated using the models for each identified complex of HII regions (see Fig. 4.6c). For each identified complex of HII regions, Table 4.5 lists: the size of each HII region, number of HII regions, factor of area covered by each density component, number of ionizing photons, star forma-

tion rate, line and continuum opacity at 8.3 GHz, the departure coefficients for the H92α line, the spectral index of the background emission and the total mass of ionized gas. Figure 4.9 shows the expected variation of radio continuum and the integrated RRL strength as a function of frequency for regions E1, E2, W1 and W2. The models shown in Figure 4.9 correspond to the mean values based on the models listed in Table 4.5.

The single-density models reproduce the observed line and continuum flux densities for all regions considered. However, these results only provide a rough estimate for the physical properties of the ionized gas. As we know from previous studies (McDonald et al. 2002), there are compact HII regions in which higher density gas ($> 10^3$ cm^{-3}) could be present. Using the area filling factor constraint in the two-density models (see section 4.4), we obtain valid solutions for regions E2, W1 and W2. These two densities are a few 10^3 cm^{-3} and 10^4 cm^{-3} as listed in Table 4.5. For the region E1, there is no evidence of any compact high-density HII regions (McDonald et al. 2002). Since for region E1 we do not have an area filling factor constraint, an estimate of the physical properties of the high-density ionized gas was not computed.

Based on these models the area filling factor from all HII regions, including the cases where the high-density component is taken into account, is ~ 0.3. We consider that the number of HII regions (obtained from the models) in the compact features is an upper limit. As listed in Table 4.5, the low-density ionized gas has an electron density of ~ 5×10^3 cm^{-3}. McDonald et al. (2002) found that the turnover in the spectrum of SNRs at 1.4 GHz requires foreground emission measures of ~ 10^7 pc cm^{-6}, consistent with our model. However, it is likely that there is also ionized gas in a diffuse component with lower electron densities. McKeith et al. (1995) estimated the electron density to be typically 1.5×10^3 cm^{-3} in the plane of M82 near the center of the galaxy. In order to explain observations in the far infrared (made at an angular resolution of 80''), Colbert et al. (1999) presented a model which is a combination of HII regions with n_e ~ 0.25×10^3 cm^{-3} and photo-dissociated regions (PDRs) with n_e ~ 2×10^3 cm^{-3}. High resolution observations of RRLs of higher quantum number (e.g. H116α), with an angular resolution similar to the H92α data presented here, are required to constrain the models to account for the gas at lower density.

Assuming that the relative number of high-density HII regions compared to the number of low-density HII regions is an age indicator of recent star formation activity, based on the two-density models, we infer that the region W2 is the youngest. Another age indicator for the starburst in each region is the spectral index α: the steeper the spectral index the more

evolved the star formation activity, which is true if we assume that each region has formed stars at a constant rate, at least during the last few 10^6 yr. Using this criteria E2 would then be the most evolved starburst. Observations of low quantum number RRLs (e.g. H43α) tracing the dense gas are required to better constrain the recent star formation history.

The number of Lyman continuum photons required to ionize all four complexes, $\sim 16 \times 10^{52}$ s^{-1}, is a factor three lower than the value estimated by Achtermann & Lacy (1995). The sum of the H92α line flux densities from the four modeled regions represents only $\sim$50% of the total line flux density; our analysis is thus restricted to the areas where the H53α line is detected. Considering this fact, the Lyman continuum rate obtained from the models is a lower limit for the total Lyman continuum rate emission in the center of M82. Then, we conclude that our results are in reasonable agreement with previous results.

M82 differs from Arp 220 in the sense that very high-density HII regions are not required to explain the line and continuum emission from the center of M82. The SFR depends on the initial mass function and mainly on the upper limit used for the mass of the stars that are formed. Using the Miller-Scalo IMF and mass limits of 1 and 100 M$_\odot$, the total SFR derived for Arp 220 is $\sim$ 240 M$_\odot$ yr^{-1} (Anantharamaiah et al. 2000), whereas that for M82 is $\sim$ 100 times lower ($\sim$ 3 M$_\odot$ yr^{-1}). Another estimate of the SFR for M82 using the same mass limits, the same IMF and assuming that all the radio continuum emission is thermal gives an upper limit of 46 M$_\odot$ yr^{-1} (Kronberg, Biermann, & Schwab 1985). If the Salpeter IMF is used then the total SFR in M82 would be $\sim$ 3 times larger. The present mass of gas in the central region of M82 (160 pc) is estimated to be $\sim$ 2 $\times$ 10^8 M$_\odot$, a factor 30 lower compared to Arp 220.

4.5 Discussion

4.5.1 Radio Continuum and RRLs H92α and H53α

There are two possible reasons that could explain why some continuum features were detected only at 8.3 GHz: (i) the features are HII regions and the higher noise level at 43 GHz limits the detection, (ii) the features are SNR with non-thermal spectrum ($\alpha < 0$, $S_\nu \propto \nu^\alpha$) and flux density at 43 GHz $< 3\sigma_{rms}$. For all the features identified as SNR, the spectral index value determined from our observations is in good agreement with a non-thermal spectra. From 17 sources identified as HII regions, 13 sources have spectral index values in agreement with a thermal spectrum (8.3 − 43 GHz). The compact sources 42.69+58.2,

42.56+58.0 and 42.48+58.4 are observed in a larger complex region; because this complex region is embedded in a more extended emission region with a similar flux density level, we were not able to determine the continuum flux densities for each of them individually. The spectral index from this complex region is not in agreement with a thermal spectra; the contribution of synchrotron emission from the SNR at 8.3 GHz may explain this result. Due to the lower angular resolution of our observations, the flux densities of some features are larger than previously reported measurements at 3.6 cm based on higher angular resolution data (Huang et al. 1994, Allen & Kronberg 1998). The larger measured flux densities arise from extended features that were resolved out by the higher angular resolution observations. There are three compact sources that have been classified as SNRs and have detectable RRL emission. The H92α line emission that seems to arise from SNRs may be accounted for if a group of HII regions is located along the same line of sight as the SNR. The RRL emission that arise in the foreground ionized gas could even be stimulated by the external emission arising from the SNR. Quite possibly the externally stimulated emission plays an important role in these lines of sight. For the source 41.95+57.5, the flux density at 8.3 GHz is 13.6±0.4 mJy using observations made in 2001. Allen & Kronberg (1998) at 8.4 GHz determined a value of 26.76±0.5 mJy in 1994-1995. The implied decay rate of this radio supernova is in good agreement with the estimates (8.8% yr^{-1}) of Allen & Kronberg (1998).

4.5.2   Comparison with other tracers of ionized gas

As observed at an angular resolution of 2″, the structure of M82 is very similar in the H92α line (Fig. 4.5) and the [Ne II] line (Fig. 1 of Achtermann & Lacy 1995). In both cases the most prominent source is W1 (see Fig. 4.6), located ~ 5″ E of the 2.2 μm peak. In the H92α line images (Fig. 5), a quasi-circular "hole" with a FWHM deconvolved size of ~ 2″ is observed. The center of this hole is located at $\alpha = 09^h51^m43^s5$, $\delta = +69°55'00''4$, which is close to the 2.2 μm peak determined by Dietz et al. (1986) at $\alpha = 09^h51^m43^s5$, $\delta = +69°55'00''7$ and shifted from the one determined by Lester et al. (1990) at $\alpha = 09^h51^m43^s6$, $\delta = +69°55'00''1$ by 1″5 in RA and by 0″3 in Dec. The position of this peak needs to be confirmed to definitively conclude if this hole as observed in H92α is, in fact, centered on this peak. The regions E1 and W1 are connected by a faint ridge of emission on the N side of this hole (see Figure 4.6). Based on the [Ne II] observations, Achtermann & Lacy (1995) have suggested the presence of an ionized ring with a projected axial ratio

Table 4.4: PARAMETERS FOR REGIONS OBSERVED IN H92α RRL

Region	$\int S_L dV$ (mJy km s^{-1})	S_L/S_C^a ($\times 10^{-2}$)	Features	Coordinates[b]	$\int S_L dV$ (mJy km s^{-1})	Size[c] ('')	Peak Flux (mJy)	V_{HEL} (km/s)	ΔV_{FWHM}^d (km/s)
(1)	(2)	(3)	(4)	(5)	(6)	(7)	(8)	(9)	(10)
E2	604	1.7±0.1	E2a	46.20+67.7	81	1.3	0.57±0.03	316±16	121±37
			E2b	45.79+65.3	65	1.4	0.82±0.05	315±5	48±11
			E2c	45.54+66.3	165	1.6	1.54±0.14	320±8	84±19
			E2d	45.43+65.6	96	0.8	0.82±0.05	311±5	95±11
			E2e	45.32+64.2	69	0.9	0.61±0.05	314±5	90±11
			E2f	45.05+63.5	32	0.4	0.26±0.06	302±7	102±16
			E2a+E2b+...+E2f		508				
E1	300	1.2±0.1	E1a	44.39+61.8	98	1.4	0.87±0.07	264±8	90±18
			E1b	44.10+62.7	56	1.6	0.56±0.05	321±10	76±24
			E1c	44.02+60.3	39	1.4	0.59±0.05	231±10	24±24
			E1a+E1b+E1c		193				
C	320	1.0±0.1	Ca	43.84+62.4	70	0.9	0.63±0.05	300±5	88±11
			Cb	43.77+63.2	137	1.2	0.61±0.05	286±5	205±11
			Cc	43.79+63.9	16	0.6	0.30±0.05	470±5	52±11
			Cd	43.39+62.3	75	1.3	1.00±0.05	239±4	44±9
			Ca+Cb+Cc+Cd		298				
W1	1067	1.6±0.1	W1a	42.95+59.2	85	1.9	0.72±0.10	165±8	96±4
			W1b	42.62+60.3	196	2.1	1.85±0.10	148±3	83±8
			W1c	42.61+58.0	291	1.7	2.88±0.07	117±2	77±3
			W1d	42.32+61.5	57	1.1	0.56±0.10	191±8	78±4
			W1e	42.21+59.9	147	1.3	1.05±0.07	125±2	120±3
			W1f	42.19+58.8	177	1.6	2.01±.10	100±3	61±8

Low angular resolution | Intermediate resolution

			W1a+W1b+...+W1f		953				
W2	878	2.0±0.1	W2a	41.75+59.0	113	1.4	0.76±0.07	114±12	128±32
			W2b	41.62+57.8	141	u	1.43±0.07	79±12	69±32
			W2c	41.51+58.6	81	1.2	0.68±0.07	113±3	96±6
			W2d	41.47+56.6	69	1.6	0.80±0.08	76±5	57±12
			W2e	41.27+59.2	65	1.1	0.69±0.11	135±5	68±10
			W2f	41.12+56.4	113	1.8	1.19±0.08	86±5	69±12
			W2g	41.07+61.0	36	1.3	0.23±0.07	84±3	133±6
			W2h	40.97+58.5	112	1.4	1.14±0.09	129±4	73±9
			W2a+W2b+...+W2h		730				

[a] The S_C and S_L values are listed in Table 3.

[b] Relative to (B1950) $09^h 51^m + 69° 54'$.

[c] Deconvolved angular size from $0.''9$ synthesized beam, u is given when the source is unresolved.

[d] Deconvolved line width from 56 km^{-1}, the spectral resolution achieved in the H92α line.

of about three, a major axis of $11''$ at a position angle of $70°$ and centered at $\alpha = 09^h 51^m 43^s.4$, $\delta = +69°55'00''.1$. Since the emission of H92α line is not affected by extinction, the lack of emission on the S side indicates that the ionized gas is not uniformly distributed along this ring. In agreement with the conclusions of Achtermann & Lacy (1995), the observed brightness of E1 and W1 cannot be explained simply by a limb brightening effect.

At $0''.9$ resolution (Fig. 4.4) the spatial distribution of the H92α line is quite patchy. The region W1 is clearly decomposed into two main components: the group composed of W1b and W1c is the brightest and is located at the SE side and the group composed of W1e and W1f is located at the NW side. These two groups would be located on the S and the N side (respectively) of the major axis (PA $70°$) of the ring proposed by Achtermann & Lacy (1995). These two groups, as observed in the $Br\gamma$ (2.17 μm) line, are separated by a ridge of extinction that extends along the major axis of M82 (Larkin et al. 1994). Since the H92α line is not affected by extinction, the lack of emission between these two groups on the W side of the 2.2 μm peak is not due to dust extinction. On the E side, as observed in the H92α line, E1 appears relatively more diffuse than W1, with the same extension as the $Br\gamma$ line. This region is located on the S edge of a ridge of extinction that extends along the major axis of M82. As we do not detect significant H92α line emission on this ridge, the distribution of $Br\gamma$ line emission for the region E1 does not seem to be significantly affected by dust extinction. The extinction derived from the Brγ line was used to determine the orientation of M82. However, the distribution of the $Br\gamma$ line emission is not severely affected by dust extinction. Thus, the fact that the brightest $Br\gamma$ sources appear on the S side cannot be used as a reliable indicator to determine the orientation of the galaxy (Larkin et al. 1994).

4.5.3 Kinematics of the ionized gas

The kinematics in the central part of M82 have been extensively studied using observations of molecular lines, HI in absorption and the infrared lines $Br\gamma$ and [Ne II]. From these studies a picture emerges in which there is an inner ring of ionized gas $\sim 11''$ ($\sim$ 200 pc) in diameter possibly surrounded by a ring of molecular gas. An alternate model for the molecular distribution with two lobes has also been proposed by Larkin et al. (1994). The presence of a stellar bar, about one kiloparsec in length, is suggested by the 2.2 μm light distribution (Lester et al. 1990). The ring of ionized gas could be related to x2 orbits at the center of the galaxy; observationally it is unclear if this ring is circular or has an oval

Table 4.5: MODELS BASED ON THE H92α AND H53α LINES

Parameter	Region E2		Region E1	Region W1		Region W2	
	SD[d]	TD[d]	SD[d]	SD[d]	TD[d]	SD[d]	TD[d]
$T_e \times 10^3$ (K)	7±2	7.5±2.5 / 6±1	7.5±2.5	6±0.5	7.5±2.5 / 5±0.5	7.5±2.5	7.5±2.5 / 6±1
$n_e \times 10^3$ (cm^{-3}) ..	9±8	40±20 / 5±4	26±25	4±3	30±10 / 4.0±2.5	15±13	30±10 / 5.5±4.0
Size (pc).........	0.81±0.59	0.14±0.05 / 0.85±54	0.75±0.65	0.72±0.34	0.15±0.04 / 0.73±33	0.52±0.36	0.15±0.04 / 0.69±0.38
$N_{HII} \times 10^3$	2.5±1.0	0.56±0.35 / 2.4±1.1	1.7±0.88	5.8±1.1	1.6±0.7 / 4.6±0.3	6.8±3.8	2.4±1.0 / 4.6±2.6
f^a	0.29±0.28	0.0013 / 0.29±0.27	0.27±0.26	0.31±0.24	0.0032 / 0.30±0.23	0.37±0.35	0.0068 / 0.40±0.37
Log N_{Ly} (s^{-1})	52.36±0.19	51.64±0.32 / 52.33±0.21	52.16±0.25	52.75±0.09	52.15±0.2 / 52.67±0.03	52.75±0.27	52.34±0.2 / 52.58±0.27
SFR^b (M$_\odot$ year^{-1})	0.37±0.13	0.10±0.07 / 0.45±0.19	0.21±0.11	1.64±0.13	0.29±0.13 / 0.86±0.05	0.63±0.51	0.45±0.19 / 0.86±0.48
τ_c (8.3 GHz)	0.27±0.26	0.032±0.023 / 0.14±0.13	0.51±0.50	0.10±0.08	0.015±0.007 / 0.09±0.07	0.35±0.32	0.015±0.007 / 0.14±0.12
τ_L (8.3 GHz)	−0.13 ± 0.10	−0.050±0.048 / −0.095±0.068	−0.16 ± 0.13	−0.09 ± 0.05	−0.032±0.027 / −0.085±0.042	−0.14 ± 0.11	−0.051±0.047 / −0.095±0.068
b_n (H92α)	0.97±0.02	0.92±0.03 / 0.96±0.02	0.97±0.03	0.97±0.02	0.91±0.025 / 0.97±0.014	0.98±0.02	0.91±0.025 / 0.97±0.02
β_n (H92α)	−20±15	−23±8.1 / −22±13	−20±16	−19±9	−26±5 / −20±8	−18±12	−26±5 / −20±11
α^c	0.95±0.20	1.0 ± 0.24	1.00±0.30	0.50±0.03	0.52 ± 0.026	0.91±0.5	0.62 ± 0.19
$M_{HII} \times 10^4$ (M$_\odot$) .	2.5±2.6	0.041±0.008 / 3.0±2.6	1.5±1.4	6.6±4.5	0.16±0.02 / 6.1±4.0	5.6±5.1	0.25±0.03 / 6.1±5.4

^{a} Area covering factor.

^{b} Star formation rate using the formulae given by Anantharamaiah et al. (2000).

^{c} Spectral index between 8.3 and 43 GHz.

^{d} Results from single-density models are listed in columns SD and results from two-density models are listed in columns labeled TD.

Table 4.6: MODELS FOR A NUCLEAR RING.

Ring center[b]	PA[b] (deg.)	Maj[b] (arcsec)	Min[b]	Vsys[b]	Vrot[b] (km s^{-1})	Vexp[b]	σ_{fit}	Line
9^{h}51^{m}43^{s}40, 69°55'0"1[b]	70	11.4	3.3	200	112	-16		[Ne II][a]
9^{h}51^{m}43^{s}40, 69°55'0"1[b]	70	11.4	3.3	193	94	-13.5	7.47	H92α
9^{h}51^{m}43^{s}40, 69°55'0"4[b]	70	11.4	3.3	196	96	-15	7.27	H92α
9^{h}51^{m}43^{s}19, 69°55'0"6	70	11.4	3.3	191	102	-13	7.35	H92α
9^{h}51^{m}43^{s}28, 69°55'0"6	66	11.4	5.6	195	103	-14	4.82	H92α

[a] Results in the first row are from Achtermann & Lacy (1995).
[b] The fixed parameters are given in bold face and free
parameters estimated from the fit in normal face.

distortion, since M82 is viewed highly inclined (i=80°). Achtermann & Lacy (1995) have shown that their data are consistent with a simple circular ring of about 150 pc diameter with a rotation velocity of ~ 112 km s^{-1} and possibly an associated outflow. They also present a model involving x1 orbits with an almost end-on view of elliptical x2 orbits.

Along the major axis of M82 the 2.2 μm light distribution is characterized by two plateaus, an inner plateau extending over ~ 20" and an outer one extending over one arcmin; the outer plateau has been interpreted as a possible evidence for a stellar bar (Telesco et al. 1991). Using images of M82 at the I, J, K and L' bands, Larkin et al. (1994) inferred that a dust lane is in front of the stellar population to the W of the nucleus, lying behind the stars to the E. This geometry is consistent with a stellar bar with leading dust lanes. Greve et al. (2002), based on extinction and polarization arguments, suggested that M82 is observed from below.

The presence of a stellar bar

The total H92α line distribution extends over ~ 35" along the major axis of M82 (Fig. 4.5), covering the inner plateau and also the inner edges of the outer plateau. Since the resulting velocity field provides the average velocity value of the gas at each position, we have used the data cube to search for the steepest velocity gradient in the center of M82. The steepest velocity gradient is determined from terminal velocities (~ 36 km s^{-1} arcsec^{-1}) and is found along a PA of ~ 57°. Only two regions, separated by ~ 7".8, define this velocity gradient: one of these regions is Ca and the other is a region located 0".4 from W1c. The center defined by these two regions is located 1".7 E from the 2.2 μm peak determined by Dietz et al. (1986). The velocity gradient could be alternatively defined between the region Ca and a region located near the center of E1a; in this case a velocity gradient of

~ 27 km s^{-1} arcsec^{-1}, at a PA of $\sim 68°$ is obtained. This PA agrees with the major axis of M82 determined on large scale. The position at mid-distance between these two regions (separated by $\sim 10''$) has an offset of $\Delta_\alpha = -1''5$, $\Delta_\delta = 0''4$ relative to the 2.2 μm peak (Dietz et al. 1986). This offset corresponds approximately to the distance between the 2.2 μm peak and the center of the inner plateau observed in the 2.2 μm profile (see Fig. 2 of Larkin et al. 1994). This asymmetry, with a truncation of the inner bar on the E side of the 2.2 μm profile, has already been noticed by Larkin et al. (1994) and could reveal the presence of ionized gas in two lobes; this suggestion is supported by our H92α observations since the regions Ca and E1a appear as the only significant features in the channels at 313 and 284 km s^{-1}. Although different velocity gradients are obtained using the regions near E1a and W1c, both regions are located on the ridge of extinction determined by Larkin et al. (1994). In any case, the center position defined by these two regions is very close to the location of maximum extinction along this ridge. Dust lanes are expected to be present at the intersection of x1 and x2 orbits. This result suggests the presence of elongated x2 orbits. Assuming that the PA of the x1 orbits corresponds to the outer plateau is $\sim 70°$ (Telesco et al. 1991), the major axis of the x2 orbits would be close to an end-on view.

The position-velocity (p-v) diagram, using the integrated flux density along the minor axis direction by taking slices at a PA of 70°, is shown in Figure 4.10 (top). This PA was used in order to compare with results from [Ne II] and Brγ observations (Achtermann & Lacy 1995, Larkin et al. 1994). In the H92α line image there is emission at "forbidden" velocities (near $-1''8$ at 215 km s^{-1}), inconsistent with purely circular motions. If non-circular motions are present, additional velocity components are observed. This feature is also observed in the Brγ line images (Fig. 5 of Larkin et al. 1994). In [Ne II], there is also emission at "forbidden" velocities but this is distributed in a symmetrical fashion about 200 km s^{-1} around the 2.2 μm peak. The agreement of the H92α p-v image is closer to the Brγ (Larkin et al. 1994) p-v images than to the [Ne II] p-v image.

Figure 4.10 (bottom) shows the p-v image constructed along the major axis using the PA of 65°. In this case the profiles are in general relatively narrower when they are compared with those in Fig. 4.10 (top); the binning along the minor axis is over a smaller region of $\sim 1''5$ as compared with 9''. However, the spectra remain relatively broad except near 8'' on the W side and 10'' on the E side. These two regions are located at the transition zones between the inner and outer 2.2 μm plateaus. The asymmetry observed at 2'' angular resolution, relative to the position of the 2.2 μm peak, is still present for this PA=65°, suggesting that the asymmetry is very likely to arise in the bar itself. In this case, there

is no emission at "forbidden" velocities, indicating that the orbits must be confined to a relatively thin plane not observed edge-on. By comparing with optical measurements (McKeith et al. 1993, Greve et al. 2002), we observe systematic effects: in the inner part ($\leq 6''$) the terminal H92α velocities are close to the optical velocities only on the W side. Neither the gas nor the stars, as observed in the optical, have velocities near ~ 325 km s^{-1} from $+1''$ to $+6''$. On the other hand, there are no optical velocities near ~ 200 km s^{-1} from $-1''$ to $-6''$. Beyond $\pm 11''$, on the outer 2.2 μm plateau, the optical velocities are systematically closer to the low velocity component of the H92α profiles. These results would indicate that for the regions located in the outer plateau, the gas as well as the stellar emission observed in the optical comes preferentially from the leading edge of the bar in the x1 orbits (see Fig. 2 of Greve et al. 2002).

The symmetry observed in the terminal velocities of the H92α line would indicate that the component of the ionized gas that we observe is not only in the x1 orbits but also in x2 orbits ($\leq \pm 3''$) and/or with some "spraying" (at radial distances from $3''$ to $6''$). The result of gas shocking in the intersection of x1 and x2 orbits is named by some authors as "spray" orbits (e.g. Downes et al. 1996). The encounter of gas moving in these two orbits breaks the flow along the x1 orbit into a spray that traverses interior of the bar until it reaches the far side of the bar. A schematic diagram for these spray orbits is shown by Downes et al. (1996). In this context it is difficult to explain why the optical velocities are close to the H92α terminal velocities only on the W side. One possibility would be that the gas observed in the optical does not spray on the E side and the gas emitting the H92α line has orbits with radii which extend relatively closer to the nucleus. An alternate possibility would be that the x2 orbits are in a plane closer to 81° inclination than the x1 orbits, the far side of the x2 orbits emitting in the optical being more severely affected by the extinction from dust in the plane of the x1 orbits.

There is a thin transition edge between the inner and outer plateaus not only observed in the p-v images made along the major axis (Fig. 4.10) but also in the velocity dispersion image (Fig. 4.8b). In Figure 4.8b an ellipse (fitted through the regions with local minima) is shown. This ellipse is centered at the same position as the ring found by Achtermann & Lacy (1995), with a major axis of $17''$ at a PA of 72° and the same axial ratio of ~ 3.5. This result agrees with the 2.2 μm light distribution for the inner plateau, consistent with a picture in which the inner and outer plateaus correspond to different families of orbits.

The inner ring

A description in terms of elongated x1 and x2 orbits is not the only model that can explain the observed kinematics in M82. The observed velocities distribution is not consistent with a rotating disk unless it consists of a set of rings with different tilt angles which may be contracting. Different methods to fit a ring in the center of M82 were used; the results are listed in Table 4.6. Row 1 of Table 4.6 lists the results of Achtermann & Lacy (1995), column 1 lists the central position of the ring, column 2 the position angle of the major axis, columns 3 and 4 the angular size of the major and minor axis, column 5 the systemic velocity, column 6 the rotation velocity, column 7 the expansion velocity, column 8 the dispersion about the model and column 9 the spectral line used to obtain the parameters of the ring. Achtermann & Lacy (1995) fixed the geometry of the ring based on the physical appearance of the distribution of the [Ne II] line emission and then fitted the velocity pattern along that ring, assuming that the ring lies in the plane of the galaxy, centered on the kinematical center. Row 2 is the result obtained from the H92α velocity pattern (Fig. 4.10a), using the same morphological parameters listed in row 1. Following the same procedure for the H92α line emission, the ellipse fitted by Achtermann & Lacy (1995) would need to be shifted ∼ 0.″3 to the N (Fig. 4.4) to coincide with the ridge of emission. In row 3, this shift of 0.″3 has been applied. In row 4, the position of the center is a free parameter. Finally, row 5 lists the parameters of the ring (shown in Fig. 4.4) obtained without imposing any morphological constraints; this procedure gives the solution with the lowest residual dispersion.

Based on the spatial distribution of the line emission, the existence of the ring is not obvious in any of the models presented in Table 4.6. According to the ring model of Achtermann & Lacy (1995) and the one described by row 5 (Table 4.6), the rotation velocity V_{rot} has a first maximum at a radius of ∼ 5″ − 6″. In the model of Achtermann & Lacy (1995) the ring surrounds a region devoid of ionized gas, in contrast with the model presented here (the best fit to the velocity pattern). Both models require not only a contraction velocity but also that the inclination angle of the rings is different than the inclination of the plane of the outer part of M82 (i=81°). The major axis of these rings is very close to the PA determined from the large scale morphology (68°).

In the velocity dispersion image (Fig. 4.8b), a well defined band at a PA of ∼ 150° is observed with systematically narrower line profiles. The length of this band is not restricted to the extent of the minor axis of the ring with axial ratio of ∼ 3.5 (Achtermann
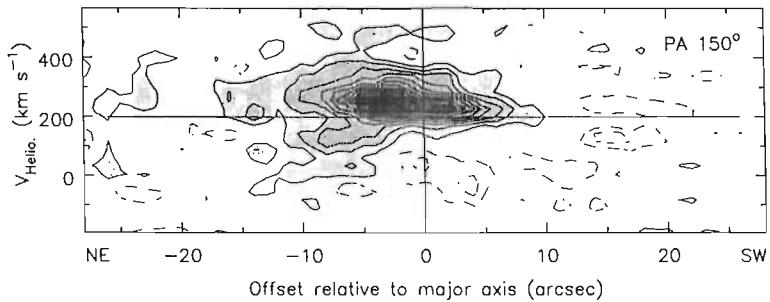
Figure 4.11: Position-velocity image along the E ridge of broad profiles (see Fig. ??) at 150°. The angular resolution is 0.″9. The offsets are relative to the major axis, NW to the left and SE to the right, the origin being at α =09^{h}51^{m}43^{s}81, δ =69°55′1.″1. Contours are -0.1, -0.05 mJy beam^{-1} (dashed) and from 0.05 to 0.5 mJy beam^{-1} in steps of 0.05 mJy beam^{-1}.

& Lacy 1995); in addition this band covers the extent of the velocity pattern along that direction. On both sides of this band, there is a ridge in which the broadest profiles are observed. These regions of large velocity dispersions are explained by the terminal velocities V_t with $|V_t - V_{sys}| \simeq 120$ km s^{-1}, along with a second velocity component in the spectra with velocities closer to V_{sys}, $|V_t - V_{sys}| \simeq 50$ km s^{-1}. Figure 4.11 shows the p-v diagram along the E ridge. The regions where $V_t \geq +300$ km s^{-1} are not restricted to the range $\leq \pm 1.″7$, which corresponds to the regions associated with the ring of axial ratio of ~3.5 (see Table 4.6). Outside the range $-5''$ to $+3''$, *i.e.* beyond the ring of axial ratio 2 (see Table 4.6), the bright component remains confined near ~ 250 km s^{-1}. We conclude that, if gas in x2 orbits and/or a fast rotating nuclear ring (spray between the x1 and x2 orbits) is responsible for $V_t > +300$ km s^{-1}, it cannot be confined in a thin plane which would give this axial ratio of ~ 3.5.

Outflow in the halo

Fig. 4.11 shows that for offsets larger than $-5''$ there is emission at two different velocities, one component emerging near ~ 150 km s^{-1} and the second one near ~ 350 km s^{-1}. At ~ $-10''$ the emission is detected in the range ~ 250 km s^{-1} and ~ 30 − 100 km s^{-1}. These results agree with the optical measurements (McKeith et al. 1993) in the lines of [SII], [NII], Hα. A more detailed view of the radial velocities of the outflow, observed in Hα, are shown in Figure 10 of Shopbell & Bland-Hawthorn (1998). The H92α observations reveal the base of the outflow into the halo. On the N side of M82 there are two velocity components: the

ionized gas on the far side of the cone (component I) has radial velocities ~ 250 km s^{-1} and on the near side of the cone (component II) the gas has radial velocities in the range ~ 30 to 100 km s^{-1}. On the S side ($\sim +5''$), the velocities are confined to ~ 200 km s^{-1} (component IV), again in agreement with the optical measurements (Shopbell & Bland-Hawthorn 1998). The geometry of the outflow and description of these four components are shown in Figure 5 of McKeith et al. (1995).

Due to the high inclination of M82, it is difficult to distinguish between an *ad-hoc* model of circular motions with radial contraction *vs* elliptical x1/x2 orbits. The ring models indicate contraction instead of expansion velocities (Table 4.6). The presence of different velocity components in the H92α line emission along a PA of 150° indicates that the ionized gas near the nucleus has already been perturbed by the outflow. A barred potential seems to provide the mechanism to bring gas from the outer parts of the disk of M82 into the central part. In this way, the gas flowing into the center of M82 would be consumed in the starburst with some gas outflow into the halo.

4.5.4   Existence of an AGN

The presence of an AGN in the center of M82 has been proposed by Matsumoto & Tsuru (1999) based on X-ray data. These authors suggest that there is an under-luminous AGN in the center of M82, comparable to Sgr A*. In the continuum at 8.3 GHz (Fig. 2a), we observe a source located near the 2.2 μm peak (Lester et al. 1990). In the continuum at 43 GHz, we do not detect this source above the $3\sigma_{rms}$ level. Muxlow et al. 1994, using MERLIN observations at 5 GHz with angular resolution of 50 mas, report a compact source (43.55+60.0) that was identified as a young supernova remnant with shell-like structure. Thus, no clear evidence has been found for the existence of a compact radio source that can be associated with an AGN in the center of M82 within our 8.3 GHz $3\sigma_{rms}$ limit of 0.12 mJy beam^{-1}.

4.6   Conclusions

We have presented high angular resolution ($< 1''$) VLA observations of radio continuum emission from M82 at 8.3 and 43 GHz and of the H92α and H53α RRLs. In the radio continuum images, we identified 19 new compact sources at 8.3 GHz and five at 43 GHz. Of these newly identified sources, four are SNRs, four are HII regions and the nature of the remaining 13 is uncertain. Three SNRs show the presence of H92α RRL emission

which can be interpreted as line emission produced by HII regions along the line of sight. No compact source is observed near the position of the derived kinematic center. Thus, in agreement with Muxlow et al. (1994), we find that there is no compelling evidence for the existence of an AGN at the center of M82.

We have modeled the line and continuum emission using a collection of HII regions. We have considered models with a single density as well as models with two density components. The H53α RRL mainly traces the high-density ionized gas. Models with multiple HII regions were used to reproduce the observations in the continuum at 5, 8.3 and 43 GHz as well as the H92α and H53α RRL emission from four separate HII complexes. The two-density model is considered to be more appropriate to model the line and continuum emission since compact continuum sources have been identified already as HII regions. However, as the two-density model is based on previous identification of thermal compact sources, the emission from region E1 (no compact thermal sources have been identified) has been modeled using only the single-density model. In general the low-density component is characterized by HII regions with sizes of ~0.8 pc and an average electron density of $\sim 5 \times 10^3$ cm^{-3} and the high-density component is characterized by HII regions with typical sizes of ~ 0.15 pc and an average electron density of $\sim 3.5 \times 10^4$ cm^{-3}. From the two-density model, we can infer that the starburst in the region W1 is the youngest. The derived mass of ionized gas in the central region of M82 is $\sim 2 \times 10^8$ M$_\odot$, 30 times lower than for Arp 220 (Anantharamaiah et al. 2000). Based on the models, it has been inferred that M82 has a star formation rate of ~ 3 M$_\odot$ year^{-1}, a factor ~ 100 lower compared with the merging system Arp 220. For a more accurate determination of the properties of the ionized gas over a complete density range, high-resolution observations of RRLs at additional higher and lower frequencies are required.

The H92α line emission extends over $\sim 35''$. The steep velocity gradient, measured at PA of 68°, is 26 km s^{-1} arcsec^{-1} in the inner ~100 pc of M82. At a distance of ~80 pc from the kinematic center, the gas has a maximum radial velocity of ~150 km s^{-1}, implying an enclosed total dynamical mass of $\sim 10^8$ M$_\odot$. From the p-v diagram of the H92α line, we observe deviations from circular motions. The observed velocity pattern cannot be due to pure circular motions; apparently the orbits in the inner parts of M82 are more face-on than in the outer parts. In the velocity dispersion image, the H92α line traces the base of a large scale outflow into the halo. This outflow is observed only on the N side. We find the PA of the axis of the outflow to be 150°. Along this axis, the widths of the profiles are narrow, suggesting collimated flow with small opening angle in the regions within the

disk. Within the disk, the steepest gradient ($\sim$ 36 km s^{-1} arcsec^{-1}), is measured from the terminal velocities. This gradient is observed at a PA of $\sim$ 57°, in a direction perpendicular to the axis of the outflow into the halo. This direction is not parallel to the PA of the large scale major axis of M82 ($\sim$ 65°) nor the PA of the 2.2 μm bar ($\sim$ 70°).

The best fit with an *ad hoc* model of circular orbits leads to a contracting ring that has its kinematic center shifted $\sim$ 1″ W of the 2.2 μm peak and located approximately in the middle of the 2.2 μm inner plateau. The nodes characterizing this ring coincide with the dust lanes; this coincidence could represent additional evidence of gas in x2 orbits of a bar potential. Due to the presence of the outflow, the kinematics observed in the H92α line provide possible evidence for the presence of x2 orbits originating from a bar potential. The inner and outer 2.2 μm plateaus correspond to two different families of orbits; the transition zone between the two plateaus has a signature in the kinematics in the form of a reverse in the velocity gradient that has been observed near the major axis.

Chapter 5

VLA H53α Radio Recombination Line Observations of Arp 220

Rodríguez-Rico, C. A., Goss, W. M., Viallefond. F., Zhao, J. H., Gómez, Y.,
Anantharamaiah, K. R.

Resumen

Arp 220 (IC 4553/4; UGC 9913; IRAS 15327+2340) tiene una luminosidad en el infrarrojo de $\sim 1.5 \times 10^{12}$ L$_\odot$, como fue determinado de observaciones de IRAS $25 - 100\,\mu$m (Soifer et al. 1984), y por lo tanto está clasificada como una ULIRG. A una distancia de ~ 70 Mpc (H$_o$ = 75 km s^{-1} Mpc^{-1}), Arp 220 se caracteriza en el óptico por la presencia de unas colas de marea, interpretadas como debidas a un proceso de fusión de galaxias (Surace, Sanders & Evans 2000). La gran extinción en el visible hacia Arp 220, que puede ser A$_V$ > 100 mag (González-Alfonso et al. 2004), impide la observación de las regiones

nucleares a frecuencias ópticas y aún del infrarrojo. Observaciones en radiofrecuencias no sufren de extinción por polvo, proveyendo una herramienta poderosa para investigar la cinemática, morfología y propiedades físicas del gas en las regiones oscurecidas por polvo de Arp 220. Las observaciones en radio revelan un sistema con dos núcleos separados por ~1″ (~ 350 pc) como se observa en CO y HI (Sakamoto et al. 1999; Mundell et al. 2001). La existencia de un número de supernovas luminosas en radio (RSN) hacia la región central de Arp 220 sugiere que su principal fuente de energía es a través del brote de formación estelar (Smith et al. 1998). Sin embargo, la emisión compacta de maser de OH y de rayos-X sugiere la presencia de actividad tipo AGN en el núcleo oeste (Norris et al. 1985; Lonsdale et al. 1998; Clements et al. 2002).

Las observaciones de alta resolución angular (0″5) de CO llevadas acabo por Sakamoto et al. (1999) sugieren que los dos núcleos están rotando en sentidos contrarios uno respecto a otro y que estan embebidos en un disco de gas con tamaño aproximado de un kiloparsec, que rota alrededor de su centro dinámico. La rotación en sentido contrario de estos núcleos, observada también en absoción de HI a alta resolución angular (0″22), muestra que la rotación no es coplanar. A partir de estas observaciones de HI, Mundell et al. (2001) proponen un modelo en el que los dos núcleos se encuentran en la etapa final de fusión. La rotación de estos dos núcleos (en sentidos contrarios) podría proveer el mecanismo para liberarse de momento angular, una condición necesaria para su fusión. Los sentidos de los gradientes de velocidad, determinado de las observaciones de emisión maser (Rovilos et al. 2003), son consistentes con las observaciones de emisión de CO y absorción de HI (Sakamoto et al. 1999; Mundell et al. 2001).

Arp 220 es el sistema más lejano en el que se han observado RRLs (Zhao et al. 1996; Anantharamaiah et al. 2000). Se han reportado observaciones en longitudes de onda centimétricas de RRL H92α por Zhao et al. (1996) y Anantharamaiah et al. (2000) con resolución angular de 4″ y 1″, respectivamente. Anantharamaiah et al. (2000), usando un telescopio de plato sencillo (IRAM 30m), detectaron la emisión de RRLs en longitudes de onda milimétricas H42α, H40α, y H31α y con el VLA establecieron límites superiores para la emisión de las RRLs H167α y H165α. Anantharamaiah et al. (2000) construyeron un modelo usando tres componentes de gas ionizado con diferentes densidades para reproducir las intensidades observadas de RRL y radiocontinuo, obteniendo una tasa de formación estelar (SFR) en Arp 220 de ~ 240 $M_\odot$ año^{-1}. La existencia de una componente de gas ionizado de alta densidad, deducida de estos modelos, fue interpretada como evidencia de formación estelar reciente en Arp 220. En particular, la RRL H53α puede ser usada como

un trazador de gas ionizado térmico de alta densidad ($\sim 10^5$ cm^{-3}). La tasa de formación estelar en este sistema podría estar soportado por múltiples brotes de formación estelar con una tasa de formación estelar alta.

En este capítulo presentamos observaciones de alta resolución angular ($0\rlap{.}''7$) hechas con el VLA de la RRL H53α así como de emisión de radiocontinuo a 43 GHz hacia la galaxia ultraluminosa en el infrarrojo (ULIRG) Arp 220. La emisión de continuo a 43 GHz muestra una estructura compacta ($\sim 2''$) con dos picos separados por $\sim 1''$, las componentes este (E) y oeste (W), que corresponden a cada núcleo galáctico del sistema en fusión. Los índices espectrales para ambas componentes la E y W, usando las imágenes de radiocontinuo a 8.3 y 43 GHz son típicas de emisión sincrotrón ($\alpha \sim -1.0$). Nuestras observaciones de continuo a 43 GHz y de línea H53α confirman las densidades de flujo predichas por los modelos propuestos por Anantharamaiah et al. (2000). Esta concordancia con los modelos implica la presencia de regiones HII compactas (~ 0.1 pc) de alta densidad ($\sim 10^5$ cm^{-3}) en Arp 220. La emisión integrada de línea H53α es más fuerte hacia los picos de radiocontinuo no térmicos, que también coinciden con los picos de emisión molecular del H$_2$CO. La coincidencia entre la emisión integrada de línea H53α y la emisión maser de H$_2$CO sugiere que las regiones de formación estelar recientes, trazadas por el gas de alta densidad, están localizadas principalmente en regiones cercanas a los dos picos de radiocontinuo. Un gradiente de velocidad de ~ 0.30 km s^{-1} pc^{-1} en la RRL H53α se observa hacia la componente E y un segundo gradiente de velocidad de ~ 0.15 km s^{-1} pc^{-1} es detectado hacia la componente W. La orientación de estos gradientes de velocidad concuerda con observaciones previas de CO, HI y OH. La cinemática del gas ionizado de alta densidad trazado por la línea H53α es consistente con dos discos que rotan en sentidos contrarios como se había sugerido a partir de observaciones de CO y HI.

Abstract

We present high angular resolution ($0\rlap{.}''7$) observations made with the Very Large Array (VLA) of the radio recombination line (RRL) H53α and radio continuum emission at 43 GHz from the ultraluminous infrared galaxy (ULIRG) Arp 220. The 43 GHz continuum emission shows a compact structure ($\sim 2''$) with two peaks separated by $\sim 1''$, the East (E) and West (W) components, that correspond to each galactic nucleus of the merger. The spectral indices for both the E and W components, using radio continuum images at 8.3 and 43 GHz are typical of synchrotron emission ($\alpha \sim -1.0$). Our 43 GHz continuum and H53α line observations confirm the flux densities predicted by the models

proposed by Anantharamaiah et al. (2000). This agreement with the models implies the presence of high-density ($\sim 10^5$ cm^{-3}) compact HII regions (~ 0.1 pc) in Arp 220. The integrated H53α line emission is stronger toward the non-thermal radio continuum peaks, which are also coincident with the peaks of molecular emission of the H_2CO. The coincidence between the integrated H53α and the H_2CO maser line emission suggests that the recent star forming regions, traced by the high density gas, are located mainly in regions that are close to the two radio continuum peaks. A velocity gradient of ~ 0.30 km s^{-1} pc^{-1} in the H53α RRL is observed toward the E component and a second velocity gradient of ~ 0.15 km s^{-1} pc^{-1} is detected toward the W component. The orientations of these velocity gradients are in agreement with previous CO, HI and OH observations. The kinematics of the high-density ionized gas traced by the H53α line are consistent with two counter rotating disks as suggested by the CO and HI observations.

5.1 Introduction

Arp 220 (IC 4553/4; UGC 9913; IRAS 15327+2340) has an infrared luminosity of $\sim 1.5 \times 10^{12}$ L$_\odot$, as determined from IRAS $25 - 100$ μm observations (Soifer et al. 1984), and therefore is classified as an ULIRG. At a distance of ~ 70 Mpc (H$_o = 75$ km s^{-1} Mpc^{-1}), Arp 220 is characterized in the optical by tidal tails interpreted as the signature of a merging process (Surace, Sanders & Evans 2000). The large visual extinction toward Arp 220, which could be A$_V > 100$ mag (González-Alfonso et al. 2004), precludes observations of the nuclear regions at optical and even at infrared frequencies. Radio frequency observations do not suffer from dust extinction, providing a powerful tool to investigate the kinematics, morphology and physical properties of the gas in the dust-obscured regions of Arp 220. Radio observations reveal a double-nucleus system separated by ~1″ (~ 350 pc) as observed in CO and HI (Sakamoto et al. 1999; Mundell et al. 2001). The existence of multiple luminous radio supernovae (RSN) in the nuclear regions of Arp 220 suggests that it is mainly starburst-powered (Smith et al. 1998). However, compact OH maser and X-ray emission suggest the presence of AGN activity in the W nucleus (Norris et al. 1985; Lonsdale et al. 1998; Clements et al. 2002).

High angular resolution (0″5) CO observations carried out by Sakamoto et al. (1999) suggest that the two nuclei are counter-rotating with respect to each other and are embedded in a kiloparsec-size gas disk, which rotates around their dynamical center. The counter-rotation is also observed in higher angular resolution (0″22) observations of HI ab-

sorption (Mundell et al. 2001), which show that the rotation is not coplanar and proposed a model in which the two nuclei are in the final state of merging. Counter-rotation may provide the mechanism to get rid of angular momentum, a condition for the two nuclei to merge. The senses of the velocity gradients, as determined from OH maser emission observations (Rovilos et al. 2003), are consistent with CO molecular emission and HI absorption observations (Sakamoto et al. 1999; Mundell et al. 2001).

Arp 220 is the most distant system from which radio recombination lines (RRLs) have been observed (Zhao et al. 1996; Anantharamaiah et al. 2000). VLA observations of the centimeter wavelength RRL H92α have been reported by Zhao et al. (1996) and Anantharamaiah et al. (2000) with angular resolutions of 4″ and 1″, respectively. Anantharamaiah et al. (2000), using a single dish telescope (IRAM 30m), detected the emission of the millimeter wavelength RRLs H42α, H40α, and H31α and with the VLA established upper limits for the RRLs H167α and H165α. Anantharamaiah et al. (2000) constructed a model using three density components of ionized gas in order to reproduce the observed RRL and radio continuum intensities, obtaining a star formation rate (SFR) in Arp 220 of ~ 240 $M_\odot$ yr^{-1}. The existence of a high-density component of ionized gas, as deduced from these models, has been interpreted as evidence for recent star formation in Arp 220. In particular, the RRL H53α can be used as a tracer of thermal high-density gas ($\sim 10^5$ cm^{-3}). The star formation in this system may be supported by multiple starbursts with a high star formation rate.

In this chapter we present VLA observations of Arp 220 in the millimeter regime of the RRL H53α (7 mm) as well as the radio continuum at 43 GHz with subarcsecond (0.″7) angular resolution.

5.2 VLA Observations of the H53α line

The RRL H53α (43 GHz) was observed with the VLA in the C configuration on October 13 and 25, 2002. The flux density scales were determined using observations of J1331+305 (1.49 Jy). The fast-switching mode was used in order to track the phase variations induced by the troposphere using cycles of 230 s on Arp 220 and 40 s on the phase reference source J1540+147 ($\sim$ 1 Jy). The bandpass response of the instrument is frequency dependent and observations of a bandpass calibrator were required for each frequency window. This bandpass response was corrected using observations of J1229+020 (17.5 $\pm$ 0.5 Jy). Five frequency windows, each of these with 15 spectral channels ($\sim$ 22 km s^{-1} each), were used

to observe the broad RRL. The total velocity coverage is ~1000 km s^{-1}. The different frequency windows were centered at 42114.9, 42135.1, 42164.9, 42185.1 and 42214.9 MHz. The on-source integration time was ~2 hrs for each frequency window. To avoid possible phase decorrelation at 7 mm, the calibration of the data was performed correcting for the phases in a first step and subsequently correcting for both amplitude and phase. The spectral line data were further calibrated by applying the solutions obtained from the self-calibration performed on the continuum channel (which contains the average of the central 75% of the bandpass) of each frequency window. The spectral line observations of the second day were not combined with those of the first day since the variable content of water vapor in the troposphere caused decorrelation of phases in the second and third frequency windows. A critical step in the reduction of the data is to determine the bandpass shape by normalizing the bandpass using the channel 0 data. Five line images, one for each frequency window of the first day, were produced using a weighting scheme intermediate between natural and uniform to obtain a circular beam of 0."7. The five line cubes were regridded in frequency and combined into a single line cube in the GIPSY environment. The method used to combine different windows is described by Rodríguez-Rico et al. (2004). The data were then Hanning-smoothed to minimize the Gibbs effect and a final velocity resolution of ~ 44 km s^{-1} was achieved. The parameters of the observations are given in Table 5.1. The resulting line cube was further processed using IMLIN from AIPS to subtract the continuum emission. A first order polynomial fit was used for the line-free channels, two on the low-velocity edge and five on the high velocity-edge of the bandpass. Previous Arp 220 observations of the RRL H42α (Anantharamaiah et al. 2000), CO(2-1) emission line (Sakamoto et al. 1999) and HI absorption (Mundell et al. 2001), show that the full width at zero intensity expected for the H53α line is in the range from ~ 5000 to 5700 km s^{-1}. The velocity range covered by the H53α line observations is $5100 - 6100$ km s^{-1}, consequently loosing the continuum that corresponds to the blueshifted side of the line. We performed a test using the line-free channels on the blueshifted side of the line as a baseline. We have determined that if weak H53α line emission with intensity < 3 mJy (3σ) is present in the velocity range of $5000 - 5100$ km s^{-1} the full width at half maximum (FWHM) is not affected. The fit for the H53α line is in agreement with the fit obtained using the continuum for the low velocity edge of the bandpass. The H53α (43 GHz) data have been compared with the RRL H92α (8.3 GHz) observations taken by Anantharamaiah et al. (2000) with the VLA in the B array.

Table 5.1: OBSERVATIONAL PARAMETERS FOR Arp 220

Parameter	H53α RRL (43 GHz)
Right ascension (J2000)	15 34 57.28
Declination (J2000)	23 30 11.9
Angular resolution	0."7
Total observing duration (hr)	13
Bandwidth (MHz)	150
Number of spectral channels	45
Center V_{Hel} (km s^{-1})	5500
Velocity coverage (km s^{-1})	1000
Velocity resolution (km s^{-1})	44
Amplitude calibrator	J1331+305
Phase calibrator	J1540+147
Bandpass calibrator	J1229+020
RMS line noise per channel (mJy beam^{-1})	1
RMS, continuum (mJy beam^{-1})	0.3

5.3   Results

5.3.1   Radio continuum

Figure 5.1 shows the continuum image of Arp 220 at 43 GHz superposed on the continuum image at 8.3 GHz, both images with an angular resolution of 0."7. In this image, the two continuum peaks (E and W) are clearly resolved at both frequencies. Using the task IMFIT in AIPS we estimated the properties of these two components. The physical parameters at 8.3 and 43 GHz were obtained integrating over equivalent areas in order to estimate the spectral index α ($S_\nu \propto \nu^\alpha$) of each component.

Table 5.2 lists the physical parameters of the continuum components E and W determined at 43 GHz. The total measured 43 GHz continuum flux density of Arp 220 is 44 ± 4 mJy. The E and W components have continuum flux densities of $\sim$ 17 and $\sim$ 21 mJy, respectively. There is also a contribution of $\sim$ 6 mJy to the total flux density from extended emission that was determined using the task IRING in the AIPS environment by integrating the flux density over an angular scale of 3" to 8". This total continuum flux density at 43 GHz is in agreement with the value obtained by interpolating from previous observations at 32 GHz and 97 GHz (Downes & Solomon 1998, Anantharamaiah et al. 2000). The continuum physical parameters at 8.3 GHz of both the E and W components in Arp 220 are listed in Table 5.3. The positions of each continuum peak are coincident at 8.3 and 43 GHz. The two radio nuclei of Arp 220 are separated by $0."9 \pm 0."1$ at a position angle of 95° (E
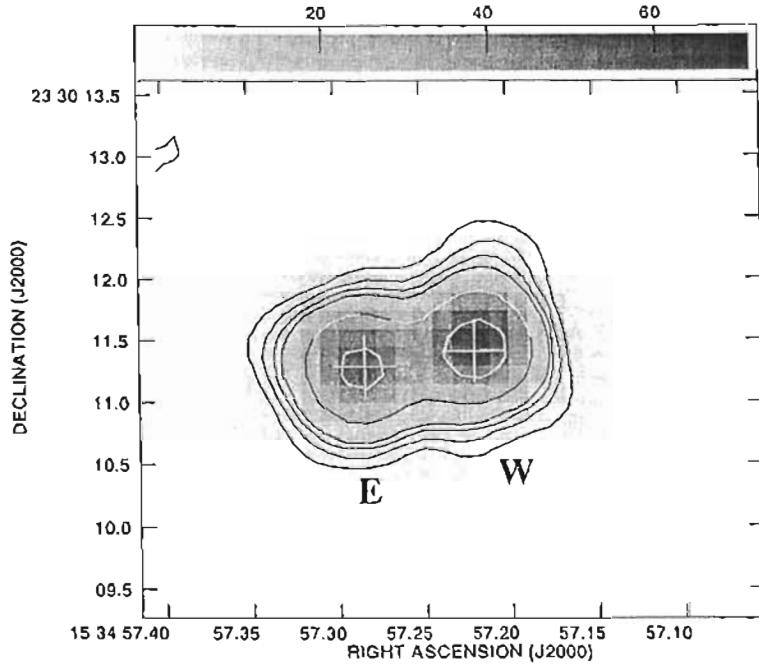
Figure 5.1: Radio continuum image of Arp 220 at 43 GHz (contours) made using VLA observations in the C array superposed on the continuum image at 8.3 GHz (gray scale) using the VLA in the B array, both images made with angular resolution of 0."7. The contour levels (43 GHz) are drawn at -3, 3, 5, 7, 9, 18, and 36 times the rms noise 0.3 mJy beam^{-1}. The gray scale (8.3 GHz) ranges from 0.15 to 70 mJy beam^{-1}. The crosses mark the peak positions (given in Table 5.2) of the 43 GHz continuum. The size of the crosses are 0."5, which is about five times the error position of the radio continuum peaks.

Table 5.2: CONTINUUM COMPONENTS OF ARP 220 AT 43 GHZ.

Feature	RA (J2000)	DEC (J2000)	Size^a, P.A.	S_c (mJy)
Arp 220 E	15^{h}34^{m}57^{s}28 ± 0^{s}01	23°30'11."3 ± 0."1	0."5 × 0."3, 89°	17 ± 2
Arp 220 W	15^{h}34^{m}57^{s}22 ± 0^{s}01	23°30'11."4 ± 0."1	0."4 × 0."2, 114°	21 ± 2

^{a} Deconvolved angular size.

with respect to N). The spectral index between these two frequencies for the E component is -0.96 ± 0.08 and for the W component is -0.97 ± 0.07. These spectral indices are typical of non-thermal emission.

5.3.2   Radio Recombination Line H53α

We detected H53α RRL emission (> 3 mJy) toward both components, E and W, of Arp 220 in the velocity range 5130 to 5600 km s^{-1}. The velocity range over which the H53α line

Table 5.3: CONTINUUM COMPONENTS OF ARP 220 AT 8.3 GHZ[a].

Feature	RA (J2000)	DEC (J2000)	Size[b], P.A.	S_C (mJy)[c]
Arp 220 E	$15^h34^m57\overset{s}{.}29 \pm 0\overset{s}{.}01$	$23°30'11\overset{''}{.}3 \pm 0\overset{''}{.}1$	$0\overset{''}{.}5 \times 0\overset{''}{.}4, 88°$	77 ± 1
Arp 220 W	$15^h34^m57\overset{s}{.}22 \pm 0\overset{s}{.}01$	$23°30'11\overset{''}{.}5 \pm 0\overset{''}{.}1$	$0\overset{''}{.}5 \times 0\overset{''}{.}3, 107°$	89 ± 1

[a] Observations at 8.3 GHz made by Anantharamaiah et al. (2000).
[b] Deconvolved angular size.
[c] Continuum flux densities were measured in the same area as the 43 GHz continuum flux densities listed in Table 5.2.

emission is observed agrees with observations of the RRLs H40α, H42α, and H92α (Anantharamaiah et al. 2000) and the CO(2-1) line (Sakamoto et al. 1999). Figure 5.2 shows the VLA spectral channel images of H53α line emission observed over the central ∼ 500 pc of Arp 220. Figure 5.3 shows the velocity-integrated line emission (moment 0) of the H53α line superposed on the moment 0 of the H92α line. The peaks in the moment 0 of the H53α line emission are nearly coincident ($< 0\overset{''}{.}5$) with the two radio continuum nuclei. The moment 0 of the H92α line emission (shown in gray scale) exhibits two peaks that are close to the continuum peaks and are coincident with the H53α peaks within $0\overset{''}{.}2$.

The total integrated spectrum over the region with detectable H53α line emission is shown in Figure 5.4 along with the E and W spectra obtained by integrating over each of these components. A single Gaussian fit was carried out for each line profile. The results from the H53α line fits are listed in Table 5.4. The peak line flux density in column (2), The FWHM of the line is given in column (3), the heliocentric velocity of the line center in column (4) and the integrated line emission in column (5). Based on the fit parameters for the E and W components, the peak H53α line flux density for the W component is approximately 30% stronger than the E component. The H53α line widths and central velocities are similar for the E and W components. The H53α and H92α line widths and central velocities determined for the total integrated line emission over Arp 220 are in good agreement with each other. Figure 5.5 shows the results from radio continuum and RRL emission models taken from Anantharamaiah et al. (2000). The measurements for the total integrated 43 GHz continuum and H53α line emission are shown in Figure 5.5a and 5.5b, respectively.

Figure 5.6 shows the H53α line velocity field (moment 1) for the ionized gas in Arp 220. Based on this H53α velocity field, two velocity gradients are observed toward the E and W components. The velocity gradient on the E component is ∼ 0.30 ± 0.10 km s^{-1} pc^{-1}, oriented along a P.A. of ∼ 30°. The velocity gradient on the W component has been marginally
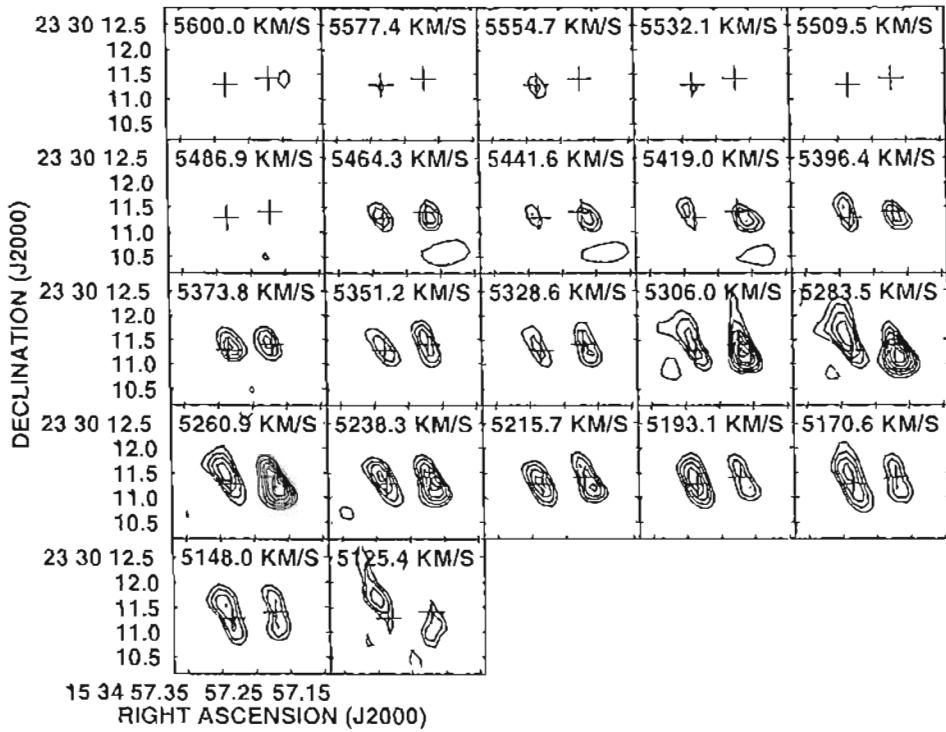
Figure 5.2: H53α continuum subtracted channel images from Arp 220 labeled according to the central heliocentric velocity of each channel. Contours are -3, 3, 4, 5, 6, 7, 8, 9, 10 and 11 times 1 mJy beam^{-1}, the rms noise. The crosses show the position of the two 43 GHz continuum peaks. The synthesized beam is 0".7 FWHM.

detected ($\sim 0.15 \pm 0.10$ km s^{-1} pc^{-1}) along a P.A. of $\sim 260°$. Due to the lower velocity resolution of the H92α line (230 km s^{-1}), compared to the velocity resolution of the H53α line (44 km s^{-1}), a detailed comparison of the H53α and the H92α velocity fields is not possible.

Table 5.4: RESULTS FROM GAUSSIAN FITTING TO THE H53α LINE EMISSION OF ARP 220.

| Feature	S_P (mJy)	ΔV_{FWHM} (km s^{-1})	V_{Helio} (km s^{-1})	$1.07\,(S_P\,\Delta V_{FWHM})$ (W m$^{-2} \times 10^{-23}$)
Arp 220 E ...	6 ± 1	235 ± 20	5240 ± 10	220 ± 40
Arp 220 W ..	8 ± 1	265 ± 30	5270 ± 10	320 ± 50
Arp 220 E+W	16 ± 2	230 ± 20	5250 ± 10	560 ± 80
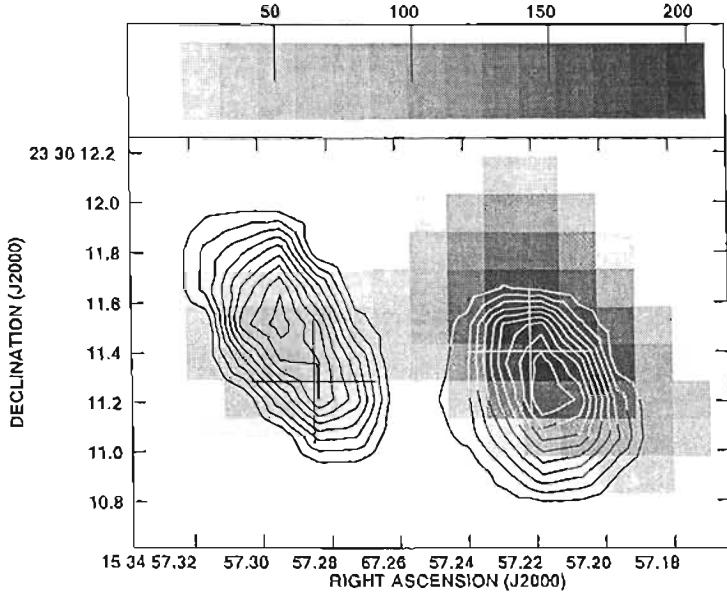
Figure 5.3: Integrated H53α line emission (moment 0) from Arp 220 in contours with integrated H92α line emission (moment 0) superposed in gray scale. Contour levels are 10, 30, 50, 70, and 90% of the peak (1.3 Jy beam^{-1} km s^{-1}). The gray scale covers the range 0 − 200 Jy beam^{-1} km s^{-1}. The crosses show the position of the two 43 GHz continuum peaks. The synthesized beam for both RRLs is 0."7 FWHM.

5.4 Discussion

The measured separation between the two continuum peaks (0."9 ± 0."1 ≃ 320 pc) and the P.A. of their separation (95°) at 43 GHz are in good agreement with previous measurements (~ 350 pc) at 5, 15 and 23 GHz (Norris et al. 1988) and 4.8 GHz (Baan & Haschick 1995). The peak positions at 8.3 and 43 GHz agree at the level of 0."1. The spectral index for Arp 220, determined using the radio continuum flux density of ~ 170 mJy measured at 8.3 GHz and the measurement at 43 GHz of ~ 44 mJy, is α ~ −1.0. On the other hand, the spectral index determined using the radio continuum flux density of ~ 49 mJy measured at 32 GHz (Baan, Gusten & Haschick 1986) and the measurement at 43 GHz (this work) of ~ 44 mJy, is α ≃ 0.36 (±0.05). Anantharamaiah et al. (2000) estimated that the thermal radio continuum flux density at 5 GHz is ~ 32 mJy. Using a spectral index value α = −0.1 for the thermal free-free emission the expected thermal flux density at 43 GHz is ~ 25 mJy, which is ~ 60% of the total measured continuum flux density at 43 GHz (see Figure 5.5). The flattening of the spectral index, a value of α closer to zero when the 32 and 43 GHz measurements are used, indicates that the ratio between the thermal emission and non-
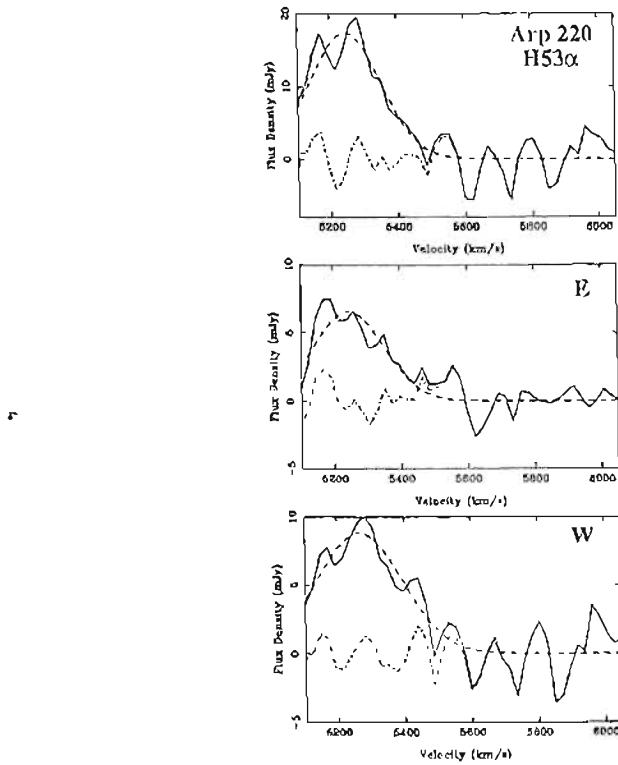
Figure 5.4: H53α recombination line profiles in Arp 220 observed using the VLA integrated over the region shown in contours in Figure 1 (top), over the E component (middle) and over the W component (bottom). The dashed line shows the resulting Gaussian fit to the data and the dashed-dotted line indicates the residuals from the Gaussian fit.

thermal emission is larger at 43 GHz than at 8.3 GHz.

Anantharamaiah et al. (2000) modeled the emission of radio continuum and RRL observations at different frequencies. In these models Anantharamaiah et al. (2000) used three thermally ionized gas components (A1, B1 and D) and non-thermal emission. Components A1 and D are characterized by electron densities of 10^3 cm^{-3}, while component B1 has a larger electron density of 2.5×10^5 cm^{-3}. All parameters for each of these components are listed in Table 9 of Anantharamaiah et al. (2000). Figure 5.5 shows the model results from Anantharamaiah et al. (2000) including the measurements of the H53α line ($\sim 510 \times 10^{-23}$ W m^{-2} or 3.7 Jy km s^{-1}) and the continuum flux density at 43 GHz (~ 44 mJy). The H53α line and 43 GHz continuum flux densities are in agreement with the values predicted in the Anantharamaiah et al. (2000) models, confirming the presence of a high-density ionized gas component ($\sim 10^5$ cm^{-3}) composed of compact HII regions
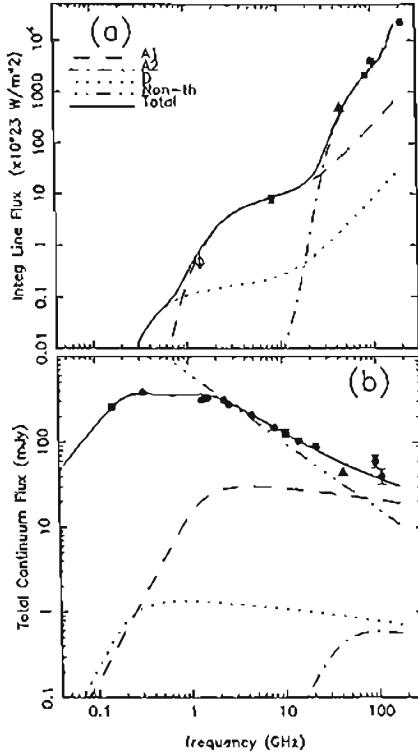
Figure 5.5: Continuum and RRL model results for three ionized gas components (A1, A2, and D) in Arp 220 by Anantharamaiah et al. (2000). The recombination line and continuum flux densities are shown in (a) and (b), respectively. The contribution from the different components are shown and the parameters for each component are given in Table 9 of Anantharamaiah et al. (2000). The observed line data points are listed in Table 2 and 4 of Anantharamaiah et al. (2000). The filled triangles indicate the velocity integrated H53α line flux density in (a) and the 43 GHz continuum flux density in (b) obtained in the current observations. The size of the triangles represent the 1σ error for the measured values.

with ~ 0.1 pc diameter. According to these models the contribution from the dense gas to the H92α line emission is negligible and the contribution from the lower density gas to the H53α line is < 10%.

On the other hand, the models of Anantharamaiah et al. (2000) indicate that ~ 50% of the H53α line emission in the high-density ionized gas is due to internal stimulated line emission. The spatial distribution of the H53α and the H92α lines is similar toward the E component as can be seen in Figure 5.3. However, a remarkable difference is observed toward the W component where the H92α line emission is more extended than the H53α line emission. Near the continuum peaks, the spatial distribution of the H53α and H92α RRLs emission suggests that the recent star formation is taking place mostly in two regions.
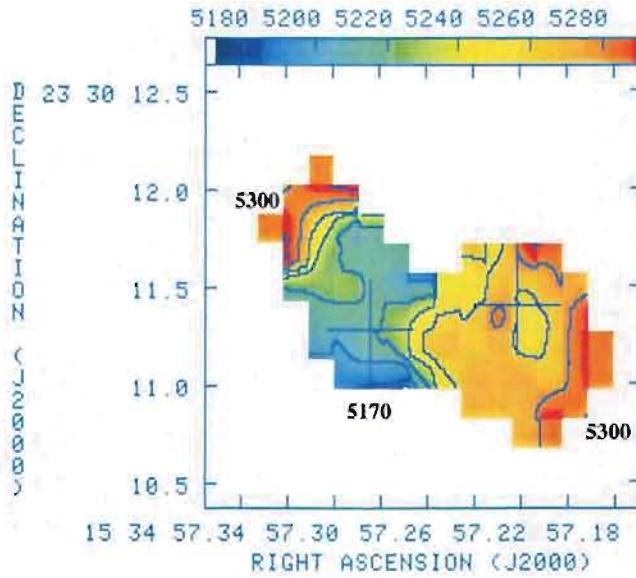
Figure 5.6: Velocity field of Arp 220 as observed in the RRL H53α with the VLA. The color scale shows the velocity field in the range from 5170 to 5370 km s^{-1}. Contour levels are 5180, 5200, ..., 5360 km s^{-1} in steps of 20 km s^{-1}. The crosses show the position of the two 43 GHz continuum peaks. The synthesized beam is 0.″7 FWHM.

These two regions of line emission are slightly displaced from the respective continuum peaks: the W line peak is 0.″2 ± 0.″1 to the S of its associated continuum peak and the E line peak is 0.″3 ± 0.″1 to the N of its associated continuum peak. According to the integrated H53α line emission (see Figure 5.3), the bulk of high-density ionized gas is concentrated in these two regions. This result is supported by the spatial correlation between the two velocity-integrated H53α line emission peaks and the peaks of the formaldehyde (H_2CO) molecular emission (Baan & Haschick 1995).

The models of Anantharamaiah et al. (2000) derived a SFR in Arp 220 of 240 $M_\odot$ yr^{-1}, assuming a mass range of 1 − 100 $M_\odot$ in the Miller-Scalo initial mass function (IMF). According to these models, the SFR could be as low as 90 $M_\odot$ yr^{-1} if the upper mass limit in the IMF is reduced to 60 $M_\odot$ and the Salpeter IMF is used. Given that the radio continuum and the velocity-integrated line flux density are in agreement with the values expected from the models of Anantharamaiah et al. (2000), the value for the SFR could be in the range of 90 to 240 $M_\odot$ yr^{-1} and the mass of high-density ionized gas ($\sim 10^5$ cm^{-3}) is

between 10^3 and 10^4 M$_\odot$.

The orientations of the H53α velocity gradients in Arp 220, with P.A. $\sim$ 30° in the E component and P.A. $\sim$ 260° in the W component agree with the CO and HI observations (Sakamoto et al. 1999; Mundell et al. 2001). Based on the P.A. of these two velocity gradients, the CO(2-1) line observations were interpreted by Sakamoto et al. (1999) as evidence of two counter-rotating disks in Arp 220. An alternative model that consists of a warped gas disk that resulted from a merger of two spiral galaxies was also proposed by Eckart & Downes (2001). The angular resolution achieved in the H53α line observations (0.″7) is insufficient to discern between these two models. The velocity structure of the ionized gas based on the H53α data show two velocity gradients in the two components of Arp 220. On the E component the H53α velocity gradient is $\sim$ 0.30 km s^{-1} pc^{-1}. The HI velocity gradient on the E component is 1.01 ± 0.02 km s^{-1} pc^{-1} (Mundell et al. 2001) and the OH velocity gradient is 0.32 ± 0.03 km s^{-1} pc^{-1} (Rovilos et al. 2003).

The velocity gradient on the E component implies a virial mass of $\sim 8 \times 10^7$ ($sin^{-2}i$) M$_\odot$ in a disk of radius $\sim$180 pc (i is the inclination). The total mass calculated from OH observations, for a disk of radius $\sim$ 80 pc, is $\sim 10^7$ M$_\odot$ (Rovilos et al. 2003). The value derived from the OH observations is consitent with the H53α line observations when the different sizes are taken into account. Based on HI and CO (Sakamoto et al. 1999; Mundell et al. 2001) observations, the estimates of the total mass are $\sim 10^9$ M$_\odot$. The total mass estimated using CO and HI observations is two orders of magnitude larger than the total mass calculated from these H53α line observations. The smaller estimates obtained from the H53α line and OH observations are explained if the molecular CO and neutral HI gas are distributed over a larger region compared to the ionized gas. In the direction of the W component, the H53α velocity gradient is a factor of 10 less than observed in HI absorption and OH maser emission (Mundell et al. 2001; Rovilos et al. 2003). However, the orientation and sense of the velocity gradient in H53α are consistent with those determined from the CO, HI and OH observations (Sakamoto et al. 1999; Mundell et al. 2001; Rovilos et al. 2003).

5.5   Conclusions

We have observed the RRL H53α and radio continuum at 43 GHz toward the ULIRG Arp 220 with high angular resolution (0.″7) using the VLA. The 43 GHz radio continuum and the RRL H53α have been compared with observations of the 8.3 GHz radio continuum

and H92α line (Anantharamaiah et al. 2000).

- The total 43 GHz radio continuum flux density of Arp 220 is 44 ± 4 mJy. The morphological characteristics observed in the radio continuum at 43 GHz agree with previous radio observations made in the range from 1.4 to 23 GHz. In the radio continuum at 43 GHz, Arp 220 exhibits a double-nucleus system that has been clearly resolved with a separation of the two radio continuum peaks of $\sim 1''$ at P.A. of 95°.

- We have determined the spectral indices for both the E and W components, using radio continuum flux densities at 8.3 and 43 GHz. Both components have spectral indices typical of synchrotron emission ($\alpha \sim -0.9$), as expected from extrapolation from the centimeter wavelength range.

- Based on 43 GHz VLA data, we confirm the predictions of the models made by Anantharamaiah et al. (2000) for RRLs. The integrated H53α line flux density is about a factor of ~ 50 times larger than the integrated H92α line flux density, in agreement with the predictions of Anantharamaiah et al. (2000). Thus, the H53α line traces the high-density ($\sim 10^5$ cm^{-3}) compact HII regions (~ 0.1 pc) in Arp 220.

- The spatial distributions of the H53α and the H92α line emission are similar in the direction of the E component. On the W component the low density ($\sim 10^3$ cm^{-3}) ionized gas component is more extended than the high density ($\sim 10^5$ cm^{-3}) component.

- The kinematic and spatial distribution behavior as observed in the RRL H53α is in agreement with results reported from CO and HI observations (Sakamoto et al. 1999; Mundell et al. 2001), supporting the counter-rotation of two disks in Arp 220 at smaller scales.

Chapter 6

VLA observations of H53α and H92α RRLs toward the starburst galaxy NGC 253

Rodríguez-Rico, C. A., Goss, W. M., Viallefond. F., Zhao, J. H., Gómez, Y., Anantharamaiah, K. R.

Resumen

NGC 253 es una de las galaxias con brote de formación estelar más cercana ($\sim$ 2.5 Mpc) y brillante, catalogada como una galaxia SAB(s)c (de Vaucouleurs et al. 1976). Esta galaxia tiene una inclinación de $\sim$ 79° con respecto a la línea de visión con el eje mayor localizado a un ángulo de posición (P.A.) de 51°, y que posee también una estructura de barra inclinada 18° con respecto al eje mayor (Pence 1981). Las observaciones de NGC 253 han sido

llevadas acabo en longitudes de onda de radio (Turner & Ho 1985; Ulvestad & Antonucci 1997; Mohan, Anantharamaiah, & Goss 2002; Mohan, Goss, & Anantharamaiah 2005; Boomsma et al. 2005) infrarrojo (Engelbracht et al. 1998), óptico (Forbes et al. 2000; Arnaboldi et al. 1995) y rayos-X (Weaver et al. 2002). Las observaciones de radio, que no son afectadas por absorción por polvo, son una herramienta excelente para estudiar la estructura y cinemática de la región nuclear de NGC 253. Las observaciones en la línea de 21-cm (Boomsma et al. 2005) revelan movimientos del HI fuera del plano que ocurren a escalas grandes de hasta 12 kpc. Las observaciones de radiocontinuo con alta resolución angular (Ulvestad & Antonucci 1997) han revelado un número (> 60) de fuentes compactas en los 300 pc centrales de esta galaxia, reforzando el escenario de un episodio de formación estelar masiva ocurriendo en el centro de NGC 253. Aproximadamente la mitad de estas fuentes compactas de continuo están dominadas por emision térmica de radio de regiones HII (Turner & Ho 1985; Antonucci & Ulvestad 1988; Ulvestad & Antonucci 1997). La emisión de radiocontinuo y de línea de recombinación en radio, observadas con alta resolución angular hacia NGC 253, han sido modeladas usando diferentes componentes de densidad para el gas ionizado (Mohan, Goss, & Anantharamaiah 2005). Los modelos de emisión sugieren la existencia tanto del gas ionizado de baja densidad ($\sim 10^3$ cm^{-3}) como de gas ionizado de alta densidad (> 10^4 cm^{-3}) en la región central de NGC 253. Por otro lado, la fuente más luminosa de radio (5.79-0.39) no está resuelta (< 1 pc) a 22 GHz sugiriendo la existencia de un AGN en el centro de ésta galaxia (Ulvestad & Antonucci 1997). Las observaciones de la línea ancha de emisión maser de H_2O ($\geq$ 100 km s^{-1}) cerca de ésta fuente de radiocontinuo se ha propuesto también como evidencia de la presencia de un objeto masivo en NGC 253 (Nakai et al. 1995). Mohan, Anantharamaiah, & Goss (2002) modelaron la emisión de radiocontinuo y de RRLs para la región nuclear de NGC 253 y favorecen un AGN como la fuente principal de ionización. Las observaciones de emisión de rayos-X duros hacia el núcleo de NGC 253 fueron también interpretados como evidencia de la actividad de un AGN (Weaver et al. 2002).

La estructura de barra hacia NGC 253, observada en el cercano infrarrojo, cubre la región interna ($\sim$ 150″ de la galaxia (Scoville et al. 1985; Forbes & Depoy 1992). La existencia de una barra estelar esta respaldada por la morfología observada a frecuencias ópticas y del mediano infrarrojo (Forbes & Depoy 1992; Piña et al. 1992). Una contraparte de la barra estelar en NGC 253 ha sido encontrada en CO (Canzian, Mundy, & Scoville 1988), HCN (Paglione, Tosaki, & Jackson 1995) y CS (Peng et al. 1996). Las observaciones en la RRL H92α (Anantharamaiah & Goss 1996) a una resolución angular de $\sim$ 1″4 revelan un

campo de velocidades que discrepa del observado en CO, CS y HCN. Anantharamaiah & Goss (1996) propusieron que la cinemática observada en la RRL H92α podría resultar de una fusión de dos galaxias. Los campos de velocidades observados en la RRL H92α y la línea de CO fueron modelados por Das, Anantharamaiah & Yun (2001) usando un potencial de barra para NGC 253. Los resultados concuerdan con el campo de velocidades de la RRL H92α, sin embargo, no se pueden reproducir simultaneamente los campos de velocidades observados en la RRL H92α, CO y CS. Dedido a las discrepancias entre los campos de velocidades del gas ionizado y los observados en CO y CS, Das, Anantharamaiah & Yun (2001) propusieron que la acreción de un objeto masivo ($\sim 10^6$ M$_\odot$) hace $\sim 10^7$ años podría explicar las diferencias observadas. Paglione et al. (2004) observaron la emisión de CO a una resolución angular de 3″ para la región interna y modelaron la cinemática del gas molecular usando un potencial de barra, concluyendo que los movimientos del gas de CO en los 150 pc centrales son consistentes con un potencial de barra y reportan evidencia que apoya la existencia de una resonancia interna de Linblad (ILR).

En este capítulo presentamos observaciones hechas con el VLA hacia NGC 253 de la RRL H53α (43 GHz) con una resolución angular de 1″.5 × 1″.0. La emisión libre-libre a 43 GHz se estima que es $\sim$ 100 mJy, implicando una tasa de formación estelar de $\sim$ 1.3 M$_\odot$ año^{-1} en la región nuclear de esta galaxia con brote de formación estelar. Se hizo un re-análisis de observaciones reportadas previamente de la RRL H92α, llevadas acabo con resolución angular de 1″.5 × 1″.0 (Anantharamaiah & Goss) y 0″.36 × 0″.21 (Mohan et al.). Basados en modelos de emisión de línea y de continuo para las observaciones con resolución angular de 1″.5 × 1″.0, la RRLs H53α y H92α trazan el gas ionizado de alta densidad ($\sim 10^5$ cm^{-3}) y de baja densidad ($\sim 10^3$ cm^{-3}) en NGC 253, respectivamente. Los campos de velocidad observados en las líneas H53α y H92α (1″.5 × 1″.0) son consistentes. Los gradientes de velocidad en la región central de la componente NE ($\sim$ 18 pc), como se observa en las líneas H53α y H92α, están en dirección opuesta al gradiente de velocidad determinada de las observaciones de CO. La masa de virial contenida, como se dedujo del gradiente de velocidad de la línea H53α en la componente NE, es $\sim$ 5 × 10^6 M$_\odot$ en la región central ($\sim$ 18 pc). Las observaciones de la RRL H92α con alta resolución angular (0″.36 × 0″.21) revelan un gradiente de velocidad mayor, a lo largo de un P.A.$\sim$ −45° en la componente NE, de $\sim$ 110 km s^{-1} arcsec^{-1}. La masa dinámica estimada usando los datos de alta resolución angular de H92α ($\sim$ 7 × 10^6 M$_\odot$) apoya la existencia de un objeto masivo acretado en la región nuclear de NGC 253.

Abstract

We present new Very Large Array (VLA) observations toward NGC 253 of the recombination line H53α (43 GHz) at an angular resolution of $1.''5 \times 1.''0$. The free-free emission at 43 GHz is estimated to be ~ 100 mJy, implying a star formation rate of $\sim 1.3\ M_\odot\ yr^{-1}$ in the nuclear region of this starburst galaxy. A reanalysis is made for previously reported H92α observations carried out with angular resolutions of $1.''5 \times 1.''0$ (Anantharamaiah & Goss) and $0.''36 \times 0.''21$ (Mohan et al.). Based on the line and continuum emission models used for the $1.''5 \times 1.''0$ angular resolution observations, the RRLs H53α and H92α are tracers of the high-density ($\sim 10^5$ cm^{-3}) and low-density ($\sim 10^3$ cm^{-3}) ionized gas components of ionized gas in NGC 253, respectively. The velocity fields observed in the H53α and H92α lines ($1.''5 \times 1.''0$) are consistent. The velocity gradient in the central ~ 18 pc of the NE component, as observed in both the H53α and H92α lines, is in the opposite direction to the velocity gradient determined from the CO observations. The enclosed virial mass, as deduced from the H53α velocity gradient over the NE component, is $\sim 5 \times 10^6\ M_\odot$ in the central ~ 18 pc region. The H92α line observations at high angular resolution ($0.''36 \times 0.''21$) reveal a larger velocity gradient, along a P.A.$\sim -45°$ on the NE component, of ~ 110 km s^{-1} arcsec^{-1}. The dynamical mass estimated using the high angular resolution H92α data ($\sim 7 \times 10^6\ M_\odot$) supports the existence of an accreted massive object in the nuclear region of NGC 253.

6.1 Introduction

NGC 253 is one of the nearest (~ 2.5 Mpc) and brightest starburst galaxies, catalogued as an SAB(s)c galaxy (de Vaucouleurs et al. 1976). This galaxy has an inclination of $\sim 79°$ with respect to the line-of-sight with major axis located at a position angle (P.A.) of $51°$, also containing a bar-like feature tilted by $18°$ with respect to the major axis (Pence 1981). Observations of NGC 253 have been carried out in the radio (Turner & Ho 1985; Ulvestad & Antonucci 1997; Mohan, Anantharamaiah, & Goss 2002; Mohan, Goss, & Anantharamaiah 2005; Boomsma et al. 2005) infrared (Engelbracht et al. 1998), optical (Forbes et al. 2000; Arnaboldi et al. 1995) and X-ray (Weaver et al. 2002) wavelengths. Radio observations, which are not affected by dust absorption, are an excellent tool to study the structure and kinematics of the nuclear region of NGC 253. Observations in the 21-cm line (Boomsma et al. 2005) reveal extra-planar motions of HI that occur at a large scale of up to 12 kpc. High angular resolution radio continuum observations (Ulvestad & Antonucci 1997) have revealed a number (> 60) of compact sources in the central 300 pc

of this galaxy, supporting the scenario of a massive star formation episode occurring in the center of NGC 253. Nearly half of these compact continuum sources are dominated by thermal radio emission from HII regions (Turner & Ho 1985; Antonucci & Ulvestad 1988; Ulvestad & Antonucci 1997). The radio continuum and radio recombination line emission, observed at high angular resolution, have been modeled using different density components for the ionized gas (Mohan, Goss, & Anantharamaiah 2005). The emission models suggest the existence of both low ($\sim 10^3$ cm^{-3}) and high-density ($> 10^4$ cm^{-3}) ionized gas in the central region of NGC 253. On the other hand, the most luminous source (5.79-0.39) is unresolved (< 1 pc) at 22 GHz suggesting the existence of an AGN in the center of this galaxy (Ulvestad & Antonucci 1997). Observations of broad H$_2$O maser line emission (≥ 100 km s^{-1}) near this radio continuum source has been invoked as further evidence of the presence of a massive object in NGC 253 (Nakai et al. 1995). Mohan, Anantharamaiah, & Goss (2002) modeled the VLA continuum and radio recombination line (RRL) emission for the nuclear region of NGC 253 and favor an AGN as the source responsible for the ionization. Observations of hard X-ray emission toward the core of NGC 253 were also interpreted as evidence of AGN activity (Weaver et al. 2002).

The bar-like structure was first observed toward NGC 253 in the near-infrared (NIR), covering the inner 150″ region of the galaxy (Scoville et al. 1985; Forbes & Depoy 1992). The existence of the stellar bar is supported by the observed morphology at optical and mid-infrared frequencies (Forbes & Depoy 1992; Piña et al. 1992). A counterpart of the stellar bar in NGC 253 has been found in CO (Canzian, Mundy, & Scoville 1988), HCN (Paglione, Tosaki, & Jackson 1995) and CS (Peng et al. 1996). Observations in the RRL H92α (Anantharamaiah & Goss 1996) at an angular resolution of $1.''8 \times 1.''0$ reveal a velocity field that is discrepant with the CO, CS and HCN observations. Anantharamaiah & Goss (1996) proposed that the kinematics observed in the H92α could result from a merger of two counter-rotating disks. The observed H92α and CO line velocity fields were modeled by Das, Anantharamaiah & Yun (2001) using a bar-like potential for NGC 253, which is in reasonable agreement with the observed H92α line velocity field. However, this kinematical model can only reproduce the velocity field of the CO and CS and does not agree with the H92α RRL observations. Based on the discrepancy of the CO and the ionized gas kinematics, Das, Anantharamaiah & Yun (2001) proposed that the accretion of a compact object ($\sim 10^6$ M$_\odot$) about 10^7 years ago could account for the velocity field observed in the H92α RRL. Paglione et al. (2004) observed the CO emission at 3″ angular resolution for the inner region and modeled the kinematics of the molecular gas using a bar

potential, concluding that motions of the CO gas in the central 150 pc are consistent with a bar potential and report evidence of the existence of an inner Linblad resonance (ILR).

In this paper we present VLA observations of the RRL H53α and the 43 GHz radio continuum, along with H92α line and 8.3 GHz radio continuum observations. Section 2 presents the observations and data reduction, while § 3 presents the results for the H53α and H92α RRLs. In subsection 4.1, a model for the emission of the RRLs H53α and H92α as well as for the radio continuum at 43 and 8.3 GHz is presented. Subsection 4.2 analyzes the kinematics for the ionized gas in the center of NGC 253 and § 5 presents the conclusions.

6.2   VLA Observations.

6.2.1   H53α line.

The H53α line (v_{rest} =43309.4 MHz) was observed in the CnD configuration of the VLA on 2003, January 18, 19 and 20. We used cycles with integration times of 10 min on NGC 253 and 1 min on the phase calibrator J0120-270 (~ 0.7 Jy). Four frequency windows (LOs) were used to observe the RRL H53α, centered at 42885.1, 42914.9, 42935.1, and 42964.9 GHz. For each frequency window, the on-source integration time was ~ 2 hrs, using the mode of 15 spectral channels with a channel separation of 3.125 MHz (~ 22 km s^{-1}). The data calibration was carried out for each frequency window using the continuum channel, consisting of the central 75% of the band. The flux density scales were determined from observations of J0137+331 (3C48; 0.54 Jy). The bandpass response of the instrument was corrected using observations of J0319+415 (3C84; ~ 7.5 Jy). The parameters of the observations are summarized in Table 6.1. In order to track reliably the phase variations introduced by the troposphere, the calibration of the data was performed correcting for the phases in a first step and subsequently correcting for both amplitude and phase. The line data were further calibrated using the solutions obtained by self-calibrating the continuum channel of each frequency window. The radio continuum images were obtained by combining the continuum channels of each frequency window using the task DBCON from AIPS, and the self-calibration method was also applied to this combined data. The H53α line cubes and the 43 GHz continuum image were made using a natural weighting scheme and then convolved to obtain a Gaussian beam of 1.″5 × 1.″0 (P.A.= 0°). The combination of the different frequency windows was made following a similar method to that used for the H53α line observed toward M82 (Rodríguez-Rico et al. 2004): (1) the line data from

Table 6.1: Observing parameters for NGC 253 using the VLA.

Parameter	H53α RRL (43 GHz)
Right ascension (J2000)	$00^h47^m33^s18$
Declination (J2000)	$-25°17'17.''0$
Angular resolution continuum	$1.''5 \times 1.''0$, P.A.= 0°
Angular resolution line	$1.''5 \times 1.''0$, P.A.= 0°
On-source observing duration (hr)	8
Bandwidth (MHz)	125
Number of spectral channels	38
Center V_{Hel} (km s^{-1})	200
Velocity coverage (km s^{-1})	1000
Velocity resolution (km s^{-1})	44
Amplitude calibrator	J0137 + 331
Phase calibrator	J0120 − 270
Bandpass calibrator	J0319 + 415
RMS line noise per channel (mJy beam^{-1})	0.5
RMS, continuum (mJy beam^{-1})	0.2

each frequency window were regridded in frequency using the GIPSY reduction package, (2) before combining the four LOs into a single line cube, the continuum emission was subtracted for each frequency window using the AIPS task IMLIN with a zero order polynomial fit based on the line free channels, and (3) the four line cubes (after subtraction of the continuum) were combined into a single line cube. The total line bandwidth, after combining all the windows, is about 150 MHz (1000 km s^{-1}). The line data cube was Hanning-smoothed using the task XSMTH in AIPS to reduce the Gibbs effect and the final velocity resolution is ~ 44 km s^{-1}.

6.2.2 H92α line.

We present observations of the RRL H92α (ν_{rest} =8309.4 MHz) at $1.''5 \times 1.''0$ (P.A.= 0°) and $0.''36 \times 0.''21$ (P.A.= −3°) angular resolutions toward NGC 253. The H92α RRL images at $1.''5 \times 1.''0$ angular resolution were produced by combining observations carried out in the B (August 31 and Sept 01, 1990), C (May 14 and 23, 1988) and D (July 01 and 19, 1988) configurations of the VLA. In order to obtain the same HPFW beam as the H53α line cube, the H92α line cube was made using these 'B+C+D' combined data applying a natural weighting scheme. Anantharamaiah & Goss (1996) have already used these 'B+C+D' combined observations to analyze the kinematics of the ionized gas in the central 10'' of NGC 253 with an angular resolution of $1.''8 \times 1.''0$, P.A.= 10°.

The higher angular resolution ($0\farcs36 \times 0\farcs21$, P.A.$= -3°$) observations of the H92α line toward NGC 253 were made with the VLA in the A array (July 9 and 12, 1999) and have been previously reported by Mohan, Anantharamaiah, & Goss (2002). Recently, Mohan, Goss, & Anantharamaiah (2005) used these H92α data along with observations in the RRLs H75α and H166α data to model the RRL and the radio continuum emission in order to determine the physical parameters of the ionized gas. We use these high angular resolution observations to study the kinematics of the ionized gas in the nuclear 5" region of NGC 253. Because of the different spectral line grid of the H92α A array data and the H92α 'B+C+D' data, a combined dataset 'A+B+C+D' was not produced.
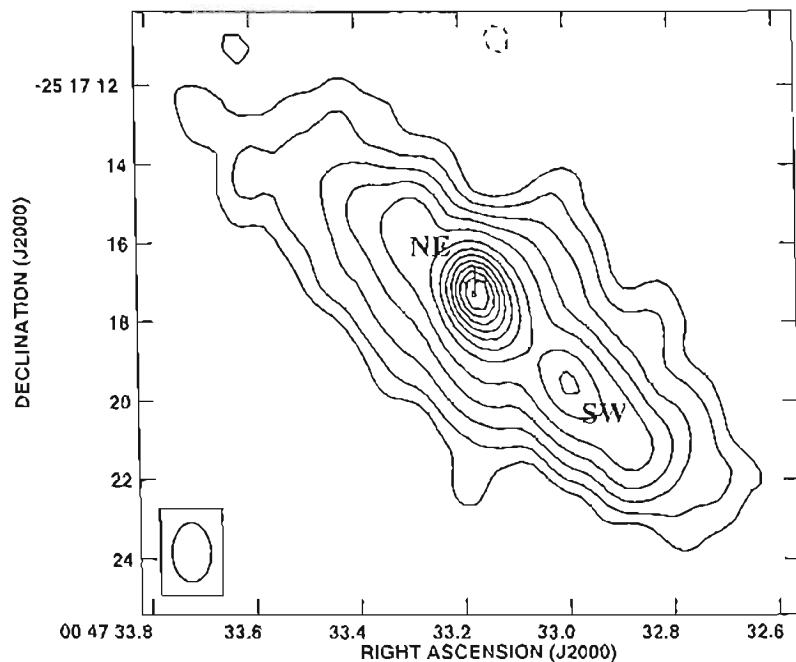

Figure 6.1: Radio continuum image of NGC 253 at 43 GHz obtained using the VLA. Contour levels are drawn at -3, 3, 6, 12, 24, 48, 96, 144, 192, 240, 288, 336, 384, and 432 times the rms of 0.2 mJy beam^{-1}. The cross shows the position of the compact source 5.79-39.0 (Ulvestad & Antonucci 1997). The angular resolution is $1\farcs5 \times 1\farcs0$, P.A.$= 0°$.

For the H92α line observations, the phase calibrator was J0118-216 and the bandpass calibrator was J2253+161. A spectral mode with 31 channels was used. The continuum images were obtained by averaging the data in the central 75% of the total band. The continuum data were processed using standard calibration and self-calibration procedures. The calibration and self-calibration used for the continuum data were then applied to the

line data. All the images were made in the AIPS environment. The line images were Hanning-smoothed to reduce the Gibbs effect and the velocity resolution is 56.4 km s^{-1}. Further observational details are summarized by Mohan, Anantharamaiah, & Goss (2002) and Mohan, Goss, & Anantharamaiah (2005).

6.3   Results

Figure 6.1 shows the radio continuum emission of NGC 253 at 43 GHz with an angular resolution of $1\rlap{.}''5 \times 1\rlap{.}''0$, P.A.= 0° ($1'' \simeq 12$ pc). The integrated 43 GHz continuum flux density is 360 ± 20 mJy, obtained by integrating the flux density over the nuclear $30''$ region using the task IRING in AIPS. The radio continuum image at 43 GHz shows two radio continuum components, NE and SW, in addition to extended emission (see Figure 1). Table 6.2 lists the peak position for each of these components in columns (2) and (3), the deconvolved angular size and P.A. in column (4) and the integrated continuum flux density in column (5). The physical parameters of the two radio continuum components have been obtained by fitting a Gaussian function using the task JMFIT in AIPS. The continuum peak position of the NE component coincides within $0\rlap{.}''2$ with the position of the compact source 5.79-39.0 (Ulvestad & Antonucci 1997).

Figure 6.2 shows the H53α velocity-channel images of NGC 253 with an angular resolution of $1\rlap{.}''5 \times 1\rlap{.}''0$ (P.A.= 0°). The H53α line emission is detected toward both the NE and SW continuum components above a 3σ level (~ 1.5 mJy). The ionized gas is observed in the H53α line at heliocentric velocities that range from 17 to 345 km s^{-1}. The velocity-integrated H53α line emission (moment 0) is shown in Figure 6.3 superposed on the moment 0 of the H92α line. There is good correspondence between the integrated line emission of the RRLs H53α and H92α. In addition, the peak position of the integrated H53α line emission is in agreement with the peak position of the 43 GHz radio continuum image. In the H53α line images, both the NE and SW components are spatially resolved only along the major axis.

Figure 6.4 shows the H53α line spectrum integrated over the central $10''$ region of NGC 253. By fitting a Gaussian, the estimated systemic velocity is 210 ± 10 km s^{-1}, the FWHM of the line is 230 ± 20 km s^{-1} and the peak line flux density is 21 ± 2 mJy. The resulting fit is shown in Figure 6.4 along with the residuals to the fit. The systemic velocity is in agreement with previous estimates in the optical (225 ± 5 km s^{-1}; Arnaboldi et al. 1995) and IR (230 ± 10 km s^{-1}; Prada, Gutiérrez & McKeith 1998). The velocity integrated
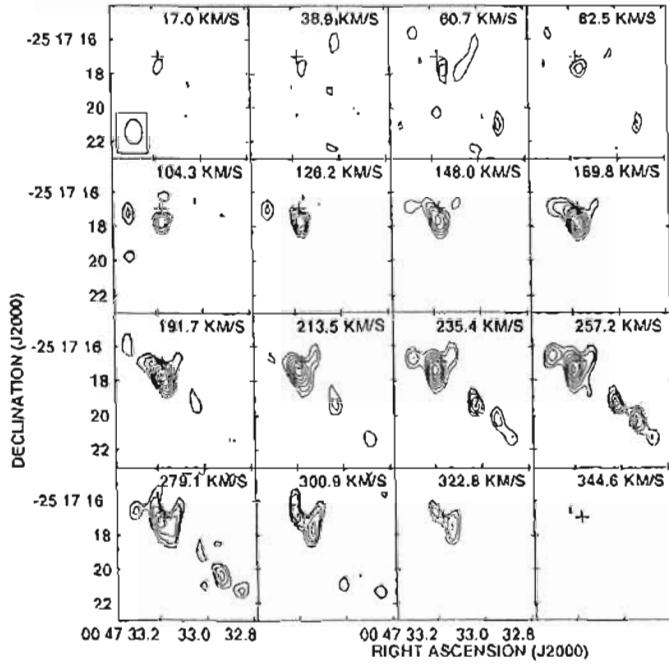
Figure 6.2: Channel images of the H53α line emission toward NGC 253 obtained using the VLA. Contours are −3, 3, 4, 5, 6, 7, 8, 9 and 10 times 0.65 mJy beam⁻¹, the rms noise. The cross shows the position of the compact source 5.79-39.0 (Ulvestad & Antonucci 1997). The synthesized beam (1."5 × 1."0 FWHM, P.A.= 0°) is shown in the first panel. The central heliocentric velocity is given above for each image.

Table 6.2: 43 GHz continuum components of NGC 253.

Feature	RA (J2000)	DEC(J2000)	Size, P.A.	S_C (mJy)
NGC 253 NE	$00^h47^m33.^s17 \pm 0.^s01$	$-25°17'17.''4 \pm 0.''1$	$1.''7 \times 1.''0, 41°$	190 ± 10
NGC 253 SW	$00^h47^m33.^s00 \pm 0.^s01$	$-25°17'19.''6 \pm 0.''1$	$2.''3 \times 0.''9, 44°$	81 ± 8

H53α line flux density determined from our observations is $0.69 \pm 0.09 \times 10^{-20}$ W m⁻², in agreement with the previous measurement of $0.94 \pm 0.38 \times 10^{-20}$ W m⁻² derived from single-dish observations (Puxley et al. 1997). A Gaussian function was also used to determine the characteristics of the spectra obtained by integrating over the NE and SW regions. Table 6.4 list the results for the total integrated H53α line emission profile, as well as for profiles that correspond to the NE and SW components. The values listed for the H53α line are peak flux density S_L, FWHM, the heliocentric velocity V_{Hel} and the velocity integrated H53α line emission.

Figure 6.5 shows the velocity field (moment 1) of the H53α line at an angular resolution
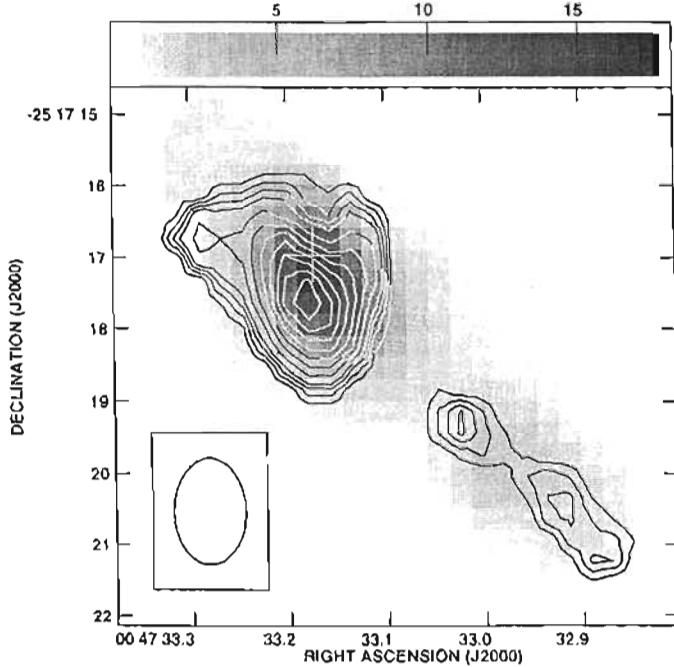
Figure 6.3: The velocity integrated (moment 0) of the H53α line emission (contours) superposed on the moment 0 of the H92α line emission (gray scale) toward NGC 253. Contour levels are drawn at 5, 10, 15, 20, 30, ..., 90% the peak line emission of 1.16 Jy beam^{-1} km s^{-1}. The gray scale (moment 0 of H92α) covers the range 0.18 − 18 Jy beam^{-1} km s^{-1}. The cross (+) shows the position of the compact source 5.79-39.0 (Ulvestad & Antonucci 1997). The HPFW, for both the H53α and the H92α line images is $1.''5 \times 1.''0$, P.A.= 0°.

of $1.''5 \times 1.''0$ (P.A.= 0°). Figure 6.6 shows the H92α velocity field made using the 'B+C+D' data of Anantharamaiah & Goss (1996) at the same angular resolution. The velocity field of the ionized gas as observed in the H53α line agrees with observations of the RRL H92α (see section 4.2 for a detailed comparison). In the NE component of NGC 253 the red-shifted gas is observed toward the NW and the blue-shifted gas toward the SE. In the elongated SW component, the red-shifted gas is located at the SW and the blue-shifted gas is at the NE. The velocity gradient was measured, at $1.''5 \times 1.''0$ angular resolution, along the major (P.A.= 52°) and minor (P.A.= −45°) axis for both RRLs the H53α and H92α. The H53α velocity gradient along the major axis of NGC 253 (measured over the NE component) is 12 ± 3 km s^{-1} arcsec^{-1}, comparable to the corresponding H92α velocity gradient (~ 11 km s^{-1} arcsec^{-1}). The velocity gradients measured in the RRLs H53α and H92α (both at $1.''5 \times 1.''0$) along the minor axis (P.A.= −45°) are 42 ± 8 km s^{-1} arcsec^{-1} and 24 ± 2 km s^{-1} arcsec^{-1}, respectively; these two velocity gradients agree within 2σ.
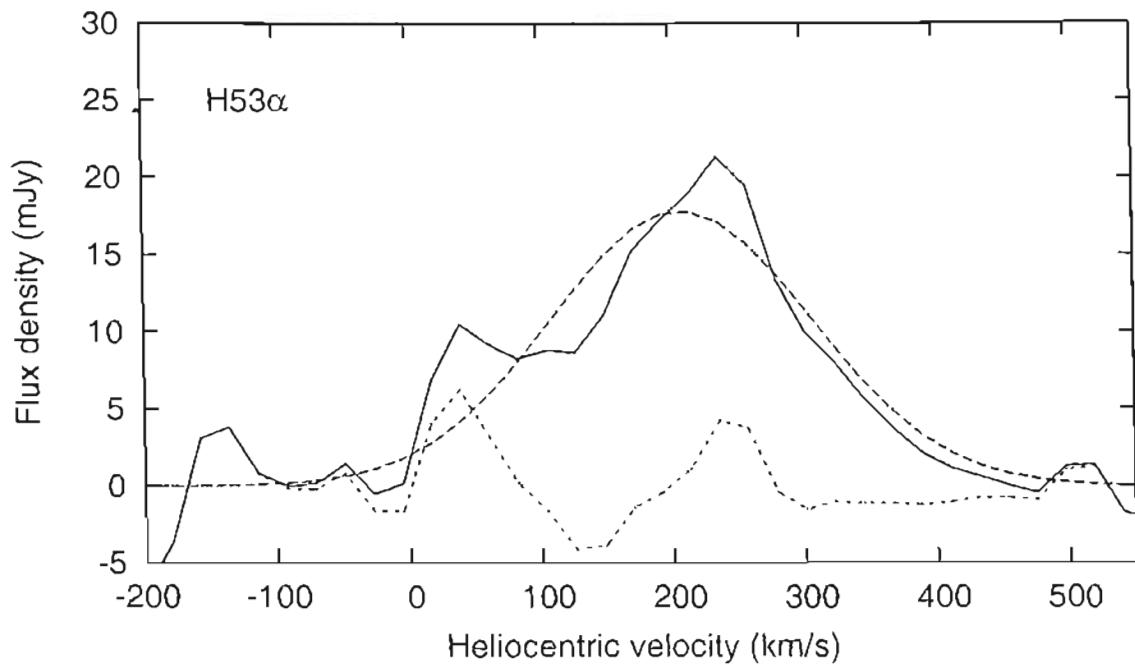
Figure 6.4: Total integrated H53α spectrum from NGC 253, obtained by integrating over the central 10″. The thick line shows the data, the dashed line shows the Gaussian fit and the dash-dotted line shows the residuals to this fit.

Figure 6.7 shows the H92α velocity field at an angular resolution of 0″36 × 0″21 (P.A.= −3°). At this angular resolution, the H92α line emission is detected only toward the NE component with an angular size of ~ 0″6 (9 pc). Based on these H92α data, a larger velocity gradient of 110 ± 20 km s^{-1} arcsec^{-1} is measured along a P.A.≃ −45°. This velocity gradient is about a factor of four larger than the velocity gradient estimated using the lower angular resolution H92α observations (1″5 × 1″0). The lower velocity gradient measured in the low angular resolution image of H92α (1″5 × 1″0) is due to a beam dilution effect. By convolving the high angular resolution data of the H92α with a Gaussian beam of 1″5 × 1″0 angular resolution, the velocity gradient measured along the P.A.= −45° is consistent with the lower angular resolution H92α data.
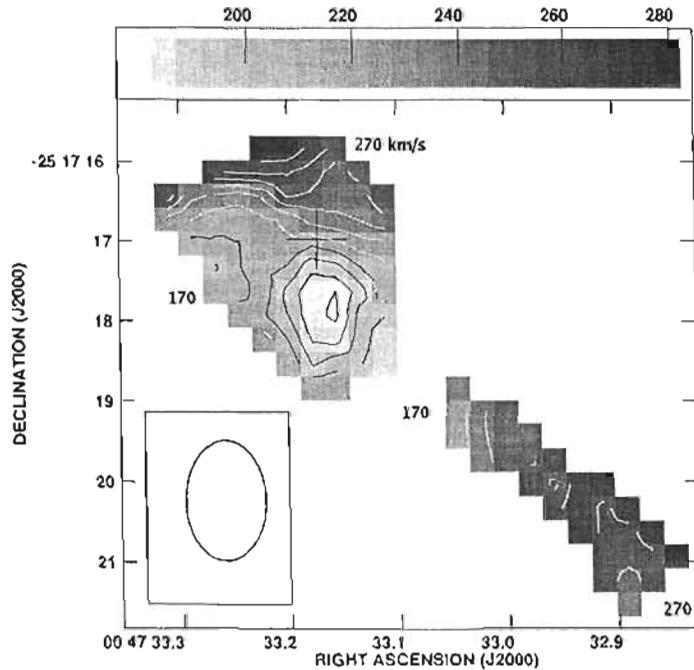
Figure 6.5: Velocity field observed in the H53α line from NGC 253. Contour levels are the heliocentric velocities at 220, 230, 240, 250, 260, 270, 280, 290 and 300 km s^{-1}. The gray scale ranges from 220 to 300 km s^{-1}. The cross (+) shows the position of the compact source 5.79-39.0 (Ulvestad & Antonucci 1997). The HPFW is 1″5 × 1″0, P.A.= 0°.

6.4 Discussion

6.4.1 Models for the radio continuum and recombination line emission

In Table 6.3, we summarize the 43 GHz continuum flux density measurement along with previous measurements (5 − 100 GHz) for the central 30″ region of NGC 253. All these flux density values have been used to determine the relative contributions from free-free, synchrotron and dust emission. At frequencies < 50 GHz, the relative contributions of free-free and non-thermal emission are dominant over the thermal dust emission. However, at frequencies > 50 GHz, dust contribution is more significant. In order to determine consistent values for the relative contributions of each different type of emission in the frequency range 5 − 100 GHz, dust emission must also be taken into account . The estimated contribution of the thermal free-free emission at 43 GHz is ∼ 100 mJy, while the non-thermal emission accounts for ∼ 250 mJy. These values were obtained assuming that the thermal continuum free-free flux density shows $S_{C-th}(\nu) \propto \nu^{-0.1}$ and the dust thermal
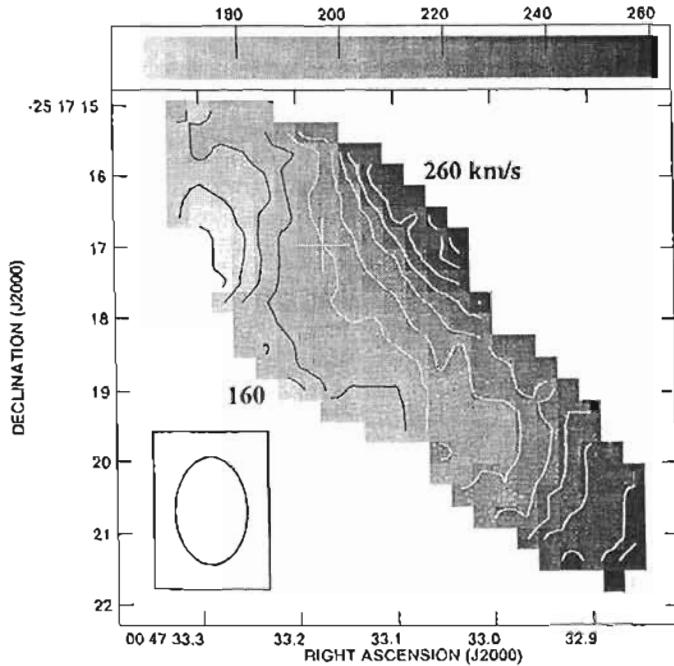
Figure 6.6: The H92α velocity field of NGC 253 (Anantharamaiah & Goss 1996), is shown in contours superposed on the gray scale image of the same H92α velocity field. Contour levels are drawn for the heliocentric velocities of the ionized gas from 160 to 260 km s^{-1} in steps of 10 km s^{-1} and the gray scale covers the same heliocentric velocity range. The cross (+) shows the position of the compact source 5.79-39.0 (Ulvestad & Antonucci 1997). The HPFW is $1\rlap{.}''5 \times 1\rlap{.}''0$, P.A.= 0°.

emission $S_D(\nu) \propto \nu^3$ (Banday & Wolfendale 1991). The resulting spectral index value for the non-thermal emission is $\alpha \simeq -0.8$. Figure 6.8 shows the contribution from thermal free-free, non-thermal and thermal dust emission along with the total radio continuum measurements at several frequencies. The thermal free-free radio continuum flux density at 43 GHz may be used to estimate the ionization rate (N_{Lyc}) from NGC 253 using (Schraml & Mezger 1969; Rodríguez et al.(1980),

$$\frac{N_{Lyc}}{s^{-1}} = 9.0 \times 10^{43} \left(\frac{S_{C-th}}{mJy}\right)\left(\frac{T_e}{10^4 K}\right)^{0.35}\left(\frac{\nu}{4.9\ GHz}\right)^{0.1}\left(\frac{D}{kpc}\right)^2, \qquad (6.1)$$

where T_e is the electron temperature, ν is the frequency and D is the distance to NGC 253. The estimated ionizing flux at 43 GHz, assuming $T_e = 10^4$ K and D= 2.5 Mpc is $\sim 7 \times 10^{52}$ s^{-1}. This N_{Lyc} value is a factor of ~ 5 lower than that estimated by Puxley et al. (1997) using the H40α line flux density and assuming local thermodynamical equilibrium (LTE) conditions. However, the RRL H40α line emission is mainly due to stimulated emission,
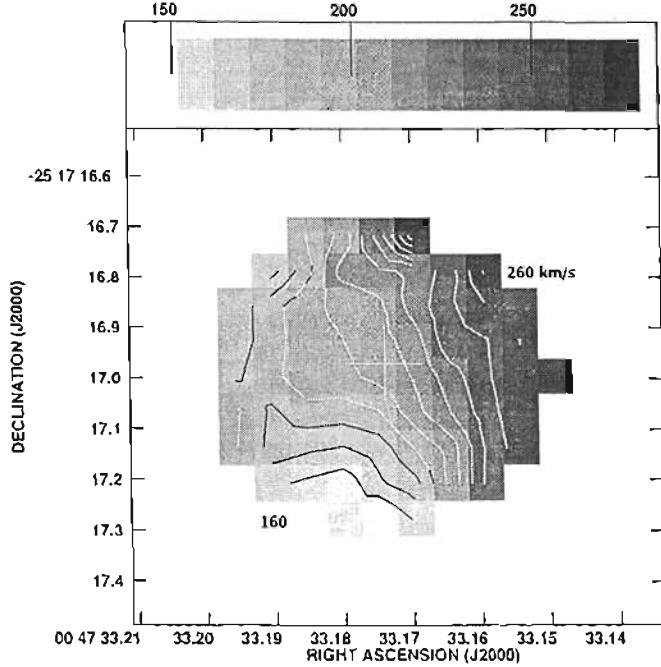
Figure 6.7: High angular resolution (0.''36 × 0.''21, P.A.= −3°) heliocentric velocity field (moment 1) image of the H92α line emission toward NGC 253 obtained using the VLA A array data. Contour levels are drawn at 160, 170, ..., 260 km s^{-1}. The cross (+) shows the position of the compact source 5.79-39.0 (Ulvestad & Antonucci 1997).

which implies a smaller value on the SFR. On the other hand, the star formation rate (Ψ_{OB}) can also be estimated using the relation $N_{Lyc} = 5.4 \times 10^{52} \times \Psi_{OB}$ s^{-1} (Anantharamaiah et al. 2000), which was obtained assuming a mass range of $1 - 100$ M$_\odot$ in the Miller-Scalo initial mass function (IMF). The total SFR derived in the nuclear regions of NGC 253 is ~ 1.3 M$_\odot$ yr^{-1}.

The emission in the RRLs H53α and H92α as well as the radio continuum at 43 and 8.3 GHz were modeled for the two continuum components, the NE and the SW, of NGC 253 observed at the 1.''5 × 1.''0 (P.A.= 0°) angular resolution. Morphologically, the velocity-integrated emission of the RRL H92α covers a larger area compared to the H53α line emission (see Figure 6.3). The line and continuum flux densities were measured for the regions where the H53α line is > 3σ. The models consist of a collection of two families of HII regions, each of these having different electron densities. The electron density ranges that were explored are $n_e = 10^2 - 10^4$ cm^{-3} and $n_e = 10^4 - 10^7$ cm^{-3}, for the low- and high-density gas components, respectively. The contribution from non-thermal
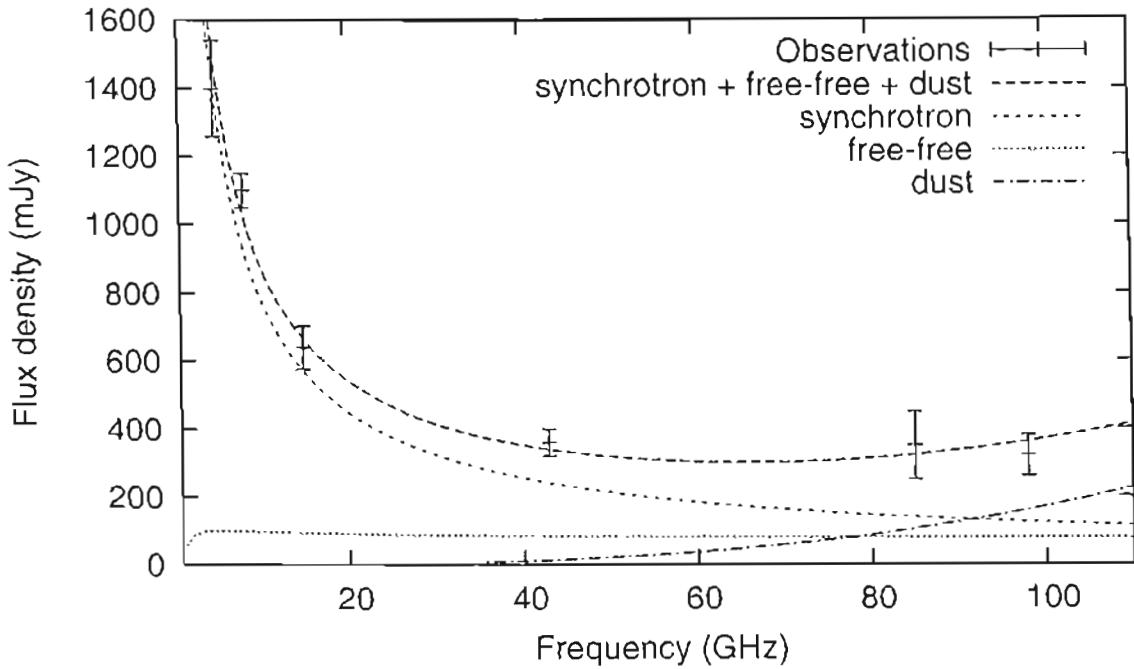
Figure 6.8: Integrated radio continuum emission measured toward the nuclear 30″ region of NGC 253 at 5, 15 GHz (Turner & Ho 1985), 43 GHz (this work), 85 GHz (Carlstrom et al. 1990) and 98 GHz (Peng et al. 1996). The contributions to the continuum flux density (Sc) are: free-free ($Sc_{free-free} \propto \nu^{-0.1}$), synchrotron ($Sc_{synchrotron} \propto \nu^{-0.8}$) and dust ($Sc_{dust} \propto \nu^{3}$) emission which are shown as indicated.

synchrotron emission that arise from SNR and the possible AGN and free-free emission from HII regions were considered. The RRL emission has been computed considering that the population of the atomic levels deviates from local thermodynamic equilibrium (LTE). The non-LTE effects result in both internally and externally stimulated line emission. The formalism used to compute the RRL and radio continuum flux densities at each frequency follows that used by (Rodríguez-Rico et al. 2004). In these models, the electron density (n_e), temperature (T_e), size (s_o) and the number of HII regions (N_{HII}) are the free parameters. In order to reduce the number of free parameters, the size of each HII region has been assumed to be a function of the electron density and the number of ionizing photons emitted by the embedded O star by [s_o $n_e^{2/3}$] $= U$, where U is a function of the spectral type of the star (Panagia 1973). In these models, early-type O7 stars have been used as the source of the ionizing continuum flux for each HII region. The results obtained for n_e and N_{HII} were constrained by the observed line and continuum flux densities as well as the volume of the total line emission assuming spherical HII regions.
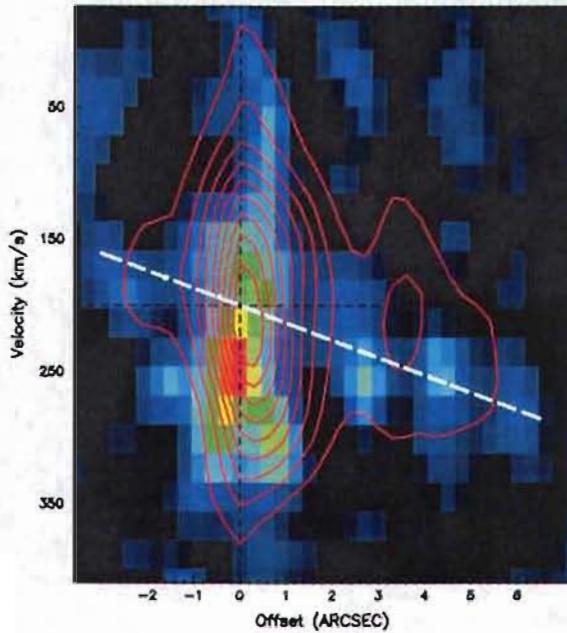
Figure 6.9: Position-velocity comparisons along the major axis (P.A.= 52°) of NGC 253. The H53α RRL PV diagram (color scale) was constructed from the data with angular resolution of $1''5 \times 1''0$, P.A.= 0° and velocity resolution of 44 km s^{-1}. The color scale covers the range $0.64 - 6.4$ mJy beam^{-1}. The H92α RRL PV diagram (contours) was constructed from the data of Anantharamaiah & Goss (1996) with angular resolution of $1''5 \times 1''0$, P.A.= 0° and velocity resolution 56 km s^{-1}. Contours are 10%, 20%, ..., 90% of the peak intensity 3.9 mJy/beam. The white dashed line shows the fitted velocity gradient of 11 km s^{-1} arcsec^{-1}.

Table 6.5 lists the results from the models. Based on these models, the RRL H92α arise mainly as externally stimulated line emission from the extended low-density ($\sim 10^3$ cm^{-3}) HII regions, with $\beta_n < -20$. The thermal free-free contribution from both the low- and high-density component to the total observed continuum emission ranges from $\sim 30\%$ to $\sim 80\%$. The models suggest that the thermally ionized gas in the NE component consists of a collection of extended ($\sim 1 - 4$ pc) low-density ($\sim 10^2 - 10^3$ cm^{-3}) HII regions and compact ($\sim 0.01 - 0.06$ pc) high-density ($\sim 10^5 - 10^6$ cm^{-3}) HII regions. The ionized gas in the SW region also consists of low- and high-density HII regions characterized by $n_e \simeq 10^2$ cm^{-3} and $n_e \simeq 10^5 - 10^6$ cm^{-3}. The total mass of thermally ionized gas in each component (NE and the SW) is $\sim 10^3$ M$_\odot$. The results obtained for the low-density gas component on the NE side of NGC 253 are in agreement with the results obtained by Mohan, Goss, & Anantharamaiah (2005) for the 15 pc region, observed with higher angular resolution observations ($\sim 0''3$) and using H166α, H92α and H75α line data. Despite the
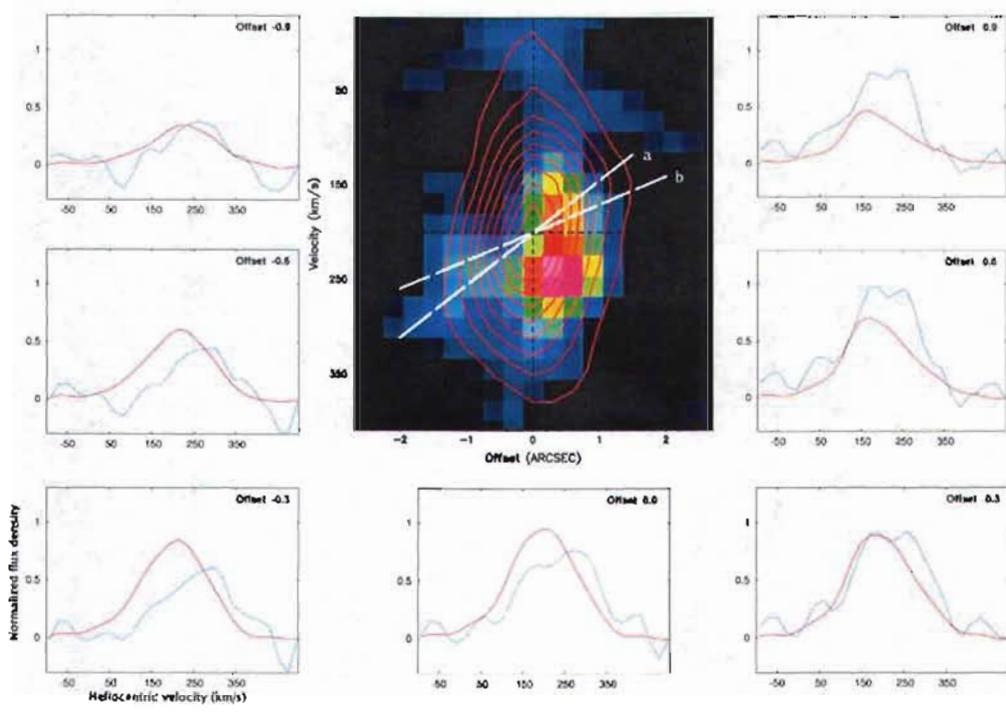
Figure 6.10: Position-velocity diagrams along a P.A.= −45° in NGC 253. The H53α RRL PV diagram (color scale) was constructed from the data with angular resolution of $1.''5 \times 1.''0$, P.A.= 0° and velocity resolution of 44 km s^{-1}. The color scale is from 0.64 to 6.4 mJy/beam. The H92α RRL PV diagram (contours) was constructed from the data of Anantharamaiah & Goss (1996), with angular resolution of $1.''5 \times 1.''0$, P.A.= 0° and velocity resolution of 56 km s^{-1}. Contours are 10%, 20%, ..., 90% of the peak intensity 3.9 mJy/beam. The white dashed lines marked with 'a' and 'b' show the fitted velocity gradients of 42 km s^{-1} arcsec^{-1} and 25 km s^{-1} arcsec^{-1}, respectively. The panels show the H53α (blue) and H92α (red) line profiles for the central $2.''1$. Each panel corresponds to a slice taken along the velocity axis of this PV diagram e.g. the panel at 0.0 is a slice along the velocity axis at offset position $0.''0$.

relative mass contribution of the high-density HII regions to the total mass of thermally ionized gas is small (< 1%), its contribution is significant (~ 40%) to the total H53α line emission. As noted before by Mohan, Goss, & Anantharamaiah (2005), the high-angular resolution observations are essential in the determination of the physical parameters of the HII regions. In addition to high angular resolution, high frequency observations (e.g. H53α) are required to determine the properties of the high-density (~ 10^5 cm^{-3}) HII regions. The consideration of non-LTE effects for the RRL emission is also relevant, showing that the total line flux density in the mm RRLs have considerable contribution (~ 50%) from stimulated emission. Thus, the results obtained assuming LTE conditions

Table 6.3: OBSERVED CONTINUUM FLUX DENSITIES FOR NGC 253[a].

Frequency (GHz)	Flux density (mJy)
5	1400 [b]
8.3	800 [c]
15	640 [b]
43	360 [d]
85	350 [e]
99	320 [f]

[a] Integrated flux density measured over the inner ~ 30″ region.
[b] Turner & Ho (1985).
[c] Mohan et al. (2002).
[d] This work.
[e] Carlstrom et al. (1990).
[f] Peng et al. (1996).

Table 6.4: RESULTS FROM GAUSSIAN FITTING TO THE H53α and H92α RRL PROFILES OF TWO REGIONS OF NGC 253.

Feature	S_C (mJy)	S_L (mJy)	ΔV_{FWHM} (km s^{-1})	V_{Hel} (km s^{-1})	$S_L \cdot \Delta V_{FWHM}$ ($\times 10^{-20}$ W m^{-2})
43 GHz				H53α	
NGC 253 NE	134 ± 5	9.0 ± 0.5	195 ± 10	250 ± 5	0.25 ± 0.01
NGC 253 SW	24 ± 2	2.8 ± 0.3	100 ± 10	280 ± 5	0.04 ± 0.01
NGC 253 Total	360 ± 20	21 ± 2	230 ± 20	230 ± 10	0.69 ± 0.09
8.3 GHz				H92α	
NGC 253 NE	278 ± 10	4.5 ± 0.1	190 ± 5	200 ± 2	2.4 ± 0.2
NGC 253 SW	40 ± 4	0.7 ± 0.1	160 ± 15	220 ± 10	0.3 ± 0.03
NGC 253 Total	605 ± 10	9.0 ± 0.5	190 ± 10	206 ± 4	4.7 ± 0.5

overestimate both the ionizing continuum flux and the SFR since the SFR is proportional to the line flux density.

6.4.2 Kinematics

The previous H92α line observations at 1″8 × 1″0 angular resolution (Anantharamaiah & Goss 1996) revealed velocity gradients of ~ 11 km s^{-1} arcsec^{-1} and ~ 18 km s^{-1} arcsec^{-1}

Table 6.5: RESULTS FROM MODELS USING A COLLECTION OF HII REGIONS FOR NGC 253.

Parameter	NE region	SW region	
T_e (K) [a]	7500 ± 2500	5000 ± 1000	
	7500 ± 2500	5000 ± 1000	
n_e (cm^{-3})[a]	$1.6 \pm 1.4 \times 10^3$	200 ± 100	(low)
	$5.5 \pm 4.5 \times 10^5$	$6.5 \pm 3.5 \times 10^5$	(high)
Size (pc)[a]	2.4 ± 1.7	4.5 ± 1.5	
	0.04 ± 0.03	0.02 ± 0.01	
EM (cm^{-6} pc)[a]	$3 \pm 2 \times 10^6$	$1.5 \pm 1 \times 10^5$	
	$50 \pm 45 \times 10^8$	$6 \pm 4 \times 10^9$	
M_{HII} (M$_\odot$)[a]	$3 \pm 2 \times 10^3$	$5 \pm 3 \times 10^3$	
	7 ± 6	0.4 ± 0.3	
τ_C (8.3GHz)[a]	$6 \pm 5 \times 10^{-3}$	$6 \pm 5 \times 10^{-4}$	
	32 ± 30	60 ± 40	
τ_C (43 GHz)[a]	$6 \pm 5 \times 10^{-5}$	$4 \pm 3 \times 10^{-5}$	
	1.0 ± 0.9	1.9 ± 1.3	
b_n (H92α)[a]	$0.881 - 0.973$	$0.819 - 0.887$	
	$0.997 - 0.999$	$0.998 - 0.999$	
b_n (H53α)[a]	$0.70 - 0.79$	$0.64 - 0.65$	
	$0.96 - 0.98$	$0.97 - 0.98$	
β_n (H92α)[a]	-55 ± 32	-70 ± 10	
	-1.25 ± 0.75	-0.15 ± 0.14	
β_n (H53α)[a]	-27 ± 13	-13 ± 2	
	-10 ± 3	-5 ± 1	
$S_{ff-43\ GHz}$ (mJy)[a]	70 ± 30	19 ± 2	
N_{Lyc} ($\times 10^{52}$ s^{-1})[a]	5 ± 2	0.9 ± 0.1	

[a] The first row corresponds to values of the low-density gas component and the second row to the high-density gas component. Both components were used to fit the continuum emission at 8.3 and 43 GHz as well as the flux densities in the RRLs H92α and H53α toward NGC 253.

along the major axis and minor axis, respectively. A qualitative comparison of the velocity field observed in the H53α and the previously reported H92α velocity field reveals kinematical behaviors that are consistent, i.e. the regions with red-shifted and blue-shifted ionized gas coincide (see Figs. 6.5 and 6.6). The coincidence of the red- and blue-shited regions in the H53α and H92α velocity fields implies that both the low- and high-density ionized gas components rotate in the same sense.

In order to compare in detail the kinematics of the ionized gas as observed in the H53α and the H92α lines, different PV diagrams were made using the task SLICE in GIPSY. A total of 11 slices, covering the central 3″3, were taken along the major (P.A.= 52°) axis of NGC 253 and then averaged to obtain the PV diagrams shown in Figure 6.9. The white line in this figure is the resulting fit to the velocity gradient of 11 km s^{-1} arcsec^{-1}. The same

procedure was made to obtain PV diagrams along the minor axis (P.A.= −45°) which are shown in Figure 6.10; the white lines are the resulting fits to the H92α velocity gradient (24 km s^{-1} arcsec^{-1}) and the H53α velocity gradient (42 km s^{-1} arcsec^{-1}). In Figure 10, the H92α and H53α spectra are shown superimposed at positions offset from the central source (5.79-39.0); these profiles were normalized using their respective peak line flux densities.

Based on the PV diagrams along the minor axis of NGC 253 (see Fig. 6.10), the low- and high-density components of the ionized gas trace different kinematics on the SW side of NGC 253. This difference is observed by inspection of the spectra taken at negative offset positions (0.''6 and 0.''9 in Figure 10). The relative velocity shift between the peak flux density of the H53α and the H92α lines, within 1 σ error, is ∼ 40 km s^{-1}. According to the line emission models, these two RRLs trace different density components. The relative velocity shift between these two RRLs suggests that, while both density components move in the same sense around the galactic nucleus, each of these gaseous components have also a particular kinematics. Thus, according to our observations the high-density component traced by the H53α line is also a higher-velocity component (red-shifted) compared to the low-density component.

Gaseous bar structure or an accreted object

Observations at IR wavelengths have revealed the existence of a gaseous bar in NGC 253 (Scoville et al. 1985). In a bar potential the gas follows two types of orbits, x1 and x2. The x1 (bar) orbits are those extended along the major axis of the bar and the x2 (anti-bar) orbits are those oriented perpendicular to the bar major axis. In the case of NGC 253, the x1 and x2 orbits would be oriented on the plane of the sky at a P.A. of ∼ 70° and ∼ −45°, respectively. In the H53α and H92α RRL images (at 1.''5 × 1.''0 angular resolution) the orientation of the largest velocity gradient is coincident with the expected orientation of the x2 orbits (P.A.∼ −45°). This coincidence suggests that a fraction of the ionized gas can be associated with these x2 orbits. However, since the ionized gas on the NE component rotates in opposite sense compared to the CO (Anantharamaiah & Goss 1996), Das, Anantharamaiah & Yun (2001), a simple bar potential does not account for the differences observed between the velocity fields of the RRLs (H92α and H53α) and CO. A secondary bar inside the primary bar may be invoked to explain the kinematics observed in the center of NGC 253. However, further observations and modeling are required to investigate the existence of this secondary bar.

Das, Anantharamaiah & Yun (2001) propose that the kinematics observed in the RRL

can be explained if there is an accreted object with mass of $\sim 10^6$ $M_\odot$; the CO tracing the galactic disk of NGC 253 and the ionized gas can be associated with the compact object near the center of NGC 253. Based on the H53α velocity gradient (~ 42 km s^{-1} arcsec^{-1}) along the minor axis of the NE component (~ 30 pc), the dynamical mass is $\sim 5 \times 10^6$ $M_\odot$. This mass estimate is consistent with that of the accreted object proposed by Das, Anantharamaiah & Yun (2001). The existence of a compact object is further supported by the higher angular resolution ($0\rlap{.}''36 \times 0\rlap{.}''21$) H92α observations, which reveal a larger velocity gradient (~ 110 km s^{-1} arcsec^{-1}, at P.A.$\simeq -45°$) over the central $\sim 0\rlap{.}''6$. This large H92α velocity gradient implies a dynamical mass of $\sim 7 \times 10^6$ $M_\odot$, similar to the mass determined from the $1\rlap{.}''5 \times 1\rlap{.}''0$ angular resolution observations of the RRLs H53α and H92α toward NGC 253. This dynamical mass is measured over a region a factor of three times smaller than that observed in the $1\rlap{.}''5 \times 1\rlap{.}''0$ angular resolution images.

The estimated dynamical mass ($\sim 7 \times 10^6$ $M_\odot$) for the nuclear region of NGC 253 is comparable to that of the compact source at the nucleus of our galaxy ($\sim 4 \times 10^6$ $M_\odot$, Ghez et al. 2005). This high mass in the central region of NGC 253 could exist in the form of a large number of stars combined with ionized gas and may also contain an AGN. The existence of an AGN has been proposed from radio continuum observations (Turner & Ho 1985; Ulvestad & Antonucci 1997) and RRL H92α observations (Mohan, Anantharamaiah, & Goss 2002). Radio continuum observations (1.3 to 20 cm), reveal that the strongest radio source 5.79-39.0 has a brightness temperature greater than 40,000 K at 22 GHz and is unresolved (< 1 pc, Ulvestad and Antonucci 1997). Broad (> 100 km s^{-1}) H_2O maser line emission is observed toward the nuclear regions supporting the existence of a massive object in the center of NGC 253 (Nakai et al. 1995).

In order to account for the different kinematics observed for the ionized and the molecular gas two possible scenarios can be proposed: a dense object accreted into the nuclear region of NGC 253 and/or a secondary bar exists within the primary bar, as proposed for other galaxies (Friedli & Marinet 1993). The accreted object model is supported by the high angular resolution H92α observations: the estimated dynamical mass of $\sim 7 \times 10^6$ $M_\odot$ is concentrated in a 7 pc region and the ionized gas traced by the RRLs rotates in the opposite direction compared to the CO. In the RRLs H53α and H92α we do not observe evidence on the existence of a set of bars. However, this scenario cannot be ruled out and higher angular resolution observations are necessary to discern between an accreted object and a set of bars.

6.5 Conclusions

The H53α RRL and radio continuum at 43 GHz were observed at high angular resolution ($1.''5 \times 1.''0$) toward NGC 253. We have also reanalyzed previous observations of the RRL H92α made at an angular resolutions of $1.''5 \times 1.''0$ (Anantharamaiah & Goss 1996) and $0.''36 \times 0.''21$ (Mohan, Anantharamaiah, & Goss 2002).

Based on the 43 GHz radio continuum flux density and previous measurements at lower and higher frequencies, we have estimated the contribution from free-free emission ($\sim$ 100 mJy). ·Using this value for the free-free emission, the derived SFR in the nuclear region of NGC 253 is ~ 1.3 $M_\odot$ yr^{-1}. The RRLs (H53α and H92α) and radio continuum (at 43 and 8.3 GHz) emission have been modeled using a collection of HII regions. Based on the models, the RRL H53α enables us to trace the compact (~ 0.1 pc) high-density ($\sim 10^5 - 10^6$ cm^{-3}) HII regions in NGC 253. The total mass of high-density ionized gas in the central 18 pc is $\sim 10^3$ $M_\odot$. A large velocity gradient (~ 42 km s^{-1} arcsec^{-1}, P.A.$\sim -45°$) is observed in the H53α line. The orientation and amplitude of the velocity gradients (angular resolution $\sim 1.''2$) derived using the H53α and H92α lines agree. The high angular resolution observations ($0.''36 \times 0.''21$) of the H92α line reveal a larger velocity gradient (~ 110 km s^{-1} arcsec^{-1}); this large velocity gradient implies a dynamical mass on the NE component (~ 7 pc) of $\sim 7 \times 10^6$ $M_\odot$.

The orientation of the H53α and H92α velocity gradients does not agree with the CO kinematics. The different kinematics observed for the ionized gas compared to the molecular gas and the derived dynamical mass ($\sim 7 \times 10^6$ $M_\odot$) suggest the existence of an accreted object. The derived dynamical mass can be accounted for by a large stellar density and/or the presence of an AGN. The star formation activity in NGC 253 may be a result of the merger process of NGC 253 and this massive compact object.

Chapter 7

Conclusiones Generales

En esta tesis hemos hecho un estudio de las propiedades físicas y cinemáticas del gas ionizado en regiones HII galácticas y extragalácticas usando para ello observaciones de líneas de recombinación en radio. Se seleccionaron fuentes brillantes en radiocontinuo y las observaciones se llevaron a cabo utilizando el Conjunto Muy Grande de radiotelescopios (VLA; Very Large Array). De manera novedosa hemos realizado observaciones de la línea H53α con los nuevos receptores a 7 mm, los cuales nos han permitido por primera vez hacer imagenes interferométricas con alta resolución angular ($\sim$ 1$''$) de esta emisión en galaxias.

Se realizaron observaciones en RRL H92α hacia las regiones HII galácticas G34.26+0.15 y G5.89-0.39. La galaxia con brote de formación estelar M82 se observó en las RRLs H92α y H53α. Arp 220 fue observada en la RRL H53α y hacia NGC 253 se llevaron a cabo observaciones de la RRL H53α y se reanalizaron observaciones de la RRL H92α. En todos estos casos de formación estelar, ya sea galácticas o extragalácticas, las observaciones de líneas de recombinación en radio fueron posibles debido a que las estrellas responsables de la ionización del hidrógeno son de tipo temprano OB, capaces de generar regiones HII lo suficientemente grandes y brillantes para ser observadas en líneas de recombinación por el VLA.

Las observaciones de regiones HII galácticas y extragalácticas difieren esencialmente en que mientras las regiones HII galácticas son resueltas espacialmente de manera individual, las regiones HII extragalácticas observadas son complejos de regiones HII, no resueltos espacialmente por el radiotelescopio y que pueden contener un gran número de estrellas OB. Para las regiones HII galácticas se puede estimar la temperatura electrónica usando la razón línea-continuo y la densidad electrónica se puede derivar si se observa el punto de re-

torno en la curva del espectro de radiocontinuo. Sin embargo, la temperatura y la densidad electrónica de las regiones HII extragalácticas no puede ser derivada de la misma manera debido a que se tiene una contribución importante de emisión sincrotrón, por lo que se necesitan modelos de emisión de RRL y radiocontinuo en los que se cuente con observaciones a diferentes frecuencias con el fin de restringir los parámetros de los modelos.

Para las regiones HII galácticas hicimos observaciones en G34.26+0.15 y G5.89-0.39. A partir de observaciones de radiocontinuo a 8.3 GHz y de la RRL H92α en estas regiones, se determinó la estructura de velocidad y variaciones de opacidad para dos regiones HII galácticas G34.26+0.15 y G5.89-0.39. Se detectó por primera vez la RRL H92α hacia la componente A de la región HII G34.26+0.15, lo cual fue sorprendente debido a que el continuo es ópticamente grueso. Además, reanalizamos datos de amoníaco (NH_3) hacia G34.26+0.15 usando las nuevas técnicas de calibración y deconvolución para imágenes en radiofrecuencias. Se detectó un nuevo grumo de amoníaco que bien puede ser calentado desde el exterior por una estrella masiva o puede tener una estrella masiva embebida. Se calculó la temperatura y masa de gas molecular asociada con el grumo recién detectado, usando observaciones de radiocontinuo a 23 GHz y de NH_3. Por otro lado, se modeló la emisión de la línea H92α y la razón de línea a continuo hacia la región HII G5.89-0.39. Se encontró que la emisión de línea en G5.89-0.39 es consistente con un disco en rotación, que tiene una cavidad en el centro.

Con respecto a las galaxias con brote de formación estelar, se observaron M82, Arp 220 y NGC 253. Todas estas galaxias fueron observadas con el VLA en la línea H53α. La galaxias con brote de formación estelar M82 fue observada también en RRL H92α (8.3 GHz) y para NGC 253 se reanalizaron observaciones de la RRL H92α. Con el fin de determinar los parámetros físicos del gas ionizado en las fuentes extragalácticas, se modeló la emisión de RRL H53α y H92α así como la emisión de continuo a 43 y a 8.3 GHz para M82 y NGC 253. En el caso de Arp 220, las densidades de flujo observadas en la RRL H53α han servido para corroborar los modelos de emisión de RRL y de radiocontinuo. Los resultados de los modelos indican que las RRLs sirven como filtros de densidad, la RRL H92α traza principalmente el gas ionizado con densidades entre 10^2 y 10^3 cm^{-3} y la RRL H53α es trazadora de gas ionizado de alta densidad ($\sim 10^5 - 10^6$ cm^{-3}).

En la galaxia M82, además de determinar los parámetros físicos de las regiones HII hacia cuatro regiones de la galaxia, se reportaron 19 nuevas fuentes compactas usando las observaciones de radiocontinuo a 8.3 GHz y cinco nuevas fuentes de las observaciones del radiocontinuo a 43 GHz hacia M82. Se analizó la cinemática del gas ionizado existente en

la parte central la galaxia con brote de formación estelar M82. Las RRLs H53α y H92α fueron usadas para obtener la curva de rotación de M82, en donde la cinemática observada es consistente con la existencia de una barra estelar, con el gas ionizado trazando las orbitas x2 de un potencial de barra. Se observó una conexión entre el brote de formación estelar y el viento galáctico de M82 usando la RRL H92α.

Arp 220 fue observada en la RRL H53α con alta resolución angular (0$\overset{''}{.}$7). La morfología de Arp 220 observada en el radiocontinuo a 43 GHz es consistente con la morfología observada en el radiocontinuo a otras frecuencias (1 − 23 GHz), exhibiendo un núcleo doble separado por $\sim$ 350 pc. Se determinaron los índices espectrales de las componentes de radiocontinuo E y W. Ambas componentes tienen índices espectrales que son típicos de emisión sincrotrón ($S_\nu \propto \nu^\alpha$; $\alpha = -0.9$). Basados en las densidades de flujo integradas en el radiocontinuo y en la RRL H53α, confirmamos las predicciones de los modelos de Anantharamaiah et al. (2000). La emisión integrada de la RRL H53α es $\sim$ 50 veces más grande que de la RRL H92α, lo cual implica que la RRL H53α traza las regiones HII compactas ($\sim$ 0.1 pc) de alta densidad ($\sim 10^5$ cm^{-3}) en Arp 220. La cinemática y la distribución espacial del gas ionizado, observado usando la RRL H53α, están de acuerdo con observaciones de CO y HI (Sakamoto et al. 1999; Mundell et al. 2001), respaldando el modelo de rotación en sentidos contrarios en Arp 220 a escalas más pequeñas.

NGC 253 fue observada con alta resolución angular (1$\overset{''}{.}$5 × 1$\overset{''}{.}$0) en la RRL H53α (43 GHz). y se reanalizaron las observaciones en la RRL H92α hacia NGC 253. Las emisiones de radiocontinuo a 43 y 8.3 GHz así como de RRL H53α y H92α fueron modeladas usando dos familias de regiones HII con densidades diferentes. De acuerdo a los modelos, los dos tipos de regiones HII son necesarias para reproducir las observaciones; una familia de regiones HII son extendidas ($\sim 3 - 5$ pc) de baja densidad ($\sim 10^2 - 10^3$ cm^{-3}) y la segunda familia de regiones HII son compactas ($\sim$ 0.02 − 0.04 pc) de alta densidad ($\sim 10^5$ cm^{-3}).

Se han comparado las observaciones de RRL H53α con las observaciones realizadas en la RRL H92α por Anantharamaiah & Goss (1996) a la misma resolución angular que la H53α (1$\overset{''}{.}$5 × 1$\overset{''}{.}$0). La orientación espacial de los gradientes de velocidad medidos en la RRL H53α concuerda con las mediciones hechas en la RRL H92α al observarlas con la misma resolución angular. La concordancia entre la orientación del gradiente de velocidad mayor (P.A$\simeq$ 45°) en la componente NE y la orientación, predicha por los modelos, de las orbitas x2 de un potencial de barra en NGC 253, sugiere que la RRL H53α traza el gas ionizado que se mueve principalmente en las orbitas x2 de un potencial de barra. La ori-

entacion de los gradientes de velocidad son consistentes en ambas RRLs, la H53α y H92α, pero no son compatibles con las observaciones de gas molecular CO, i.e. las regiones de isovelocidad no concuerdan al comparar el gas ionizado con el gas molecular observandose que el gas ionizado trazado por las RRLs rotan en sentido opuesto al CO. Usando las observaciones de RRL H53α en la componente NE ($\sim$ 30 pc) se estimó una masa dinámica de $\sim 5 \times 10^6$ M$_\odot$. Esta masa concuerda con la masa propuesta por Das et al. (2001) para un objeto acretado 10^7 años atrás y que podría explicar la falta de concordancia entre los campos de velocidades del gas ionizado y el gas molecular CO. Se reanalizaron también observaciones de la RRL H92α con resolución angular de $\sim 0.''3$ reportadas por Mohan et al. (2001). Estas observaciones de RRL H92α revelan la existencia de un objecto compacto que presenta un gradiente de velocidad, a lo largo del P.A.$\simeq 45°$, que es un factor de tres más grande que el estimado de las observaciones hechas a $1.''5 \times 1.''0$ de resolución angular, sugiriendo la presencia de un objeto más denso.

En general, las observaciones de las líneas de recombinación en radio han mostrado su gran importancia para lograr una comprensión total de la formación estelar y los fenómenos relacionados con esta. Los puntos más relevantes en el estudio de regiones de formación estelar llevado a cabo en esta tesis son que las líneas de recombinación nos permiten observar directamente la cinemática del gas ionizado y determinar sus parámetros físicos (temperatura electrónica, densidad y velocidad). El estudio de la cinemática del gas ionizado hacia las regiones de formación estelar extragalácticas ha permitido probar que las RRLs son una herramienta tan poderosa que pueden ser usadas para estudiar la conexión entre el brote de formación estelar y los vientos galácticos, como fue en el caso de M82. Por último, y no menos importante es el hecho de que las RRLs sirven como filtros de densidad, las líneas de recombinación a frecuencias de $\sim$ 8 GHz como la H92α traza gas ionizado de densidad $\sim 10^3$ cm^{-3} y las líneas de recombinación a frecuencias de $\sim$ 43 GHz como la H53α traza la componente de gas ionizado de densidades de $\sim 10^4 - 10^5$ cm^{-3}.

Chapter 8

Apendix A. Line and continuum imaging procedure for M82

The line imges were produced with the following procedure:

a) CLIPPING THE DATA. The 43 GHz data of M82 are incomplete for distances in the *u,v plane* < 10 kλ because of the lack of short baselines. Hence the structures with angular scales > 20″, if present, have been filtered out. From observations at other frequencies, e.g. the results at 8 GHz (see Fig. 3.1), we know that the radio continuum emission in M82 is elongated with a size along its major axis covering ∼ 30″. The Fourier transforms of the three incomplete *u,v* data sets result in images with strong broad ripples parallel to the major axis of M82 due to the sharp discontinuity (10 kλ) in the sampling of the visibilities for this extended source. These ripples are slightly different from channel to channel. We postulate that, with our velocity resolution of 44 km s^{-1}, the line emission in the different channels is not associated to large scale structures, and very unlikely contributes in the low spatial frequencies; this is supported by the fact that the H92α line emission at 8.3 GHz does not show large scale structures. We attribute this channel to channel variation in the structure of the ripples as due to uncertainties in the bandpass determination which we estimate to have an accuracy of not better than ∼ 1%. By clipping the visibilities amplitudes > 1 Jy below 10 kλ we reduce the discontinuity in the *u,v* plane and remove from the raw image some continuum, the component emitting on large scale. This clipping appears to be very effective; it is our first step which removes already part of the contamination by the continuum preventing us to see the line component in our data.

b) SELECTING THE CONTINUUM CHANNELS. At each position the selection of a

maximum number of channels is necessary to obtain a reliable determination of the continuum level. The maximum bandwidth of ~ 350 km s^{-1} per LO window makes this determination critical if broad-line features are present in M82. Based on the sub-arcsecond resolution achieved, the line profiles at each position are narrower than those observed at lower angular resolution. However, there is a variation of the line centroid which depends on position due to the rotation of the gas in M82. Because of this variation, the line-free channels vary with position. To overcome this difficulty, two different line cubes were used to define the line-free channels as a function of position. The mask, which is an image used to define the line emission regions in each channel, is used to obtain a three-dimensional image with line-free channels.

The first line images are observations af the $\lambda 12.8\mu m$ [Ne II] line at 2" and 30 km s^{-1} resolution (Achtermann & Lacy 1995). Althoug these near infrared observations may suffer some extinction (~ 0.25 mag), it is possible to use the higher sensitivity of the [Ne II] line images to define the line emission regions. In the [Ne II] line images, a cutoff of 0.02 Jy beam^{-1} was adopted to produce the mask (spatial and frequency). The second image is a low spatial resolution line cube image ($1\rlap{.}''9 \times 1\rlap{.}''7$) of H92$\alpha$, which has also a comparatively higher singal-to-noise ratio. A cutoff of 0.16 mJy beam^{-1} was adopted for the H92α line images.

c) ESTIMATING AND SUBTRACTING THE CONTINUUM LEVEL. The contribution of the continuum emission was estimated independently for each LO window. An independent estimate for each LO window is required because each window has a different u,v coverage. In order to compute the continuum level at each position, three different estimates were used: 1) A baseline that can be a zero or first order degree polynomial function, 2) an average continuum that is computed using the samel LO window and 3) an average continuum that is computed using the other two LO windows. These different estimates are obtained as follows:

c1) BASELINE FIT. At each position in each data set i, we fitted a baseline $b_i(x, y, v)(i = 1, 2, 3)$. Based on the number of line-free channels (N_{LF}) found at each position, two cases are possible: (1) If $N_{LF} > 3$, then a first degree polynomial was fitted, (2) If $N_{LF} \leq 3$, then a zero degree polynomial was used.

c2) AVERAGE ESTIMATE OF THE CONTINUUM OBTAINED FROM THE SAME LO WINDOW. For each position, the average value of the baseline obtained in 'c1' was computed $c_i(x, y,)$. This average level provides an initial estimate of the average continuum level with weights $n_i(x, y)$ that correspond to the number of line-free channels at each

position.

c3) AVERAGE ESTIMATE OF THE CONTINUUM USING THE OTHER TWO LO WINDOWS. For each data set i, we determined a seond average estimate of the continuum level $d_i(x, y)$. This was obtained by averaging all the line-free channels found in the data sets $j \neq i$ ($j = 1, 2$, and 3). The result is an image for which a beam can be associated. This beam is obtained as the average of the beams associated with each data set i. A component model of each image $d_i(x, y)$ was constructed using the CLEAN algorithm. This COMPONENT model was then convolved with the sinthesized beam associated with the data set i. This provides a second estimate of the continuum level $e_i(x, y)$ with weights $m_i(x, y)$ that correspond to the number of line-free channels found in the data sets $j \neq i$ at each position. This method provides a continuum image that is consistent with the u, v coverage of the data set i, since the beam associated with the data set i was utilized.

The line-free channel data set i is obtained by subtracting $b_i(x, y, v)$ and by adding an offset $(c_i \times m_i(x, y) + c_i \times n_i(x, y))/(m_i(x, y) + n_i(x, y) - c_i(x, y))$ in each channel v of the data set i. The offset correction has been used to minimize the offsets between the continuum levels in each LO window at each position. An absolute value of the continuum flux density at each position for each LO window is unknown. Minimizing the offsets in the continuum levels between adjacent LO windows results in minimizing the noise level in the frequency overlapping regions. The estimate of the continuum level in step 'c3' increases significantly the number of channels that contribute to the determination of the continuum. Using only the estimate found in 'c2' would give results of much lower quality, especially for those regions with broad line features. When broad line features are observed the number of line-free channels are limited and in some cases may not be totally line-free. In these cases, the value of the continuum level obtained in 'c2' is an overestimation of the continuum. Using the other LO windows to estimate the continuum level downweight properly the continuum level. This method is used for each LO window and minimizes uncertainties in the bandpass calibrations.

Bibliography

[1] Acord, J. M., Walmsley, C. M., & Churchwell, E. 1997, ApJ, 475, 693

[2] Achtermann, J. M. & Lacy, J. H., 1995, ApJ, 439, 163

[3] Afflerbach, A., Churchwell, E., Acord, J. M., Hofner, P., Kurtz, S., Depree, C. G. 1996, ApJS, 106, 423

[4] Akeson, R. L., & Carlstrom, J. E. 1996, ApJ, 470, 528

[5] Allen, M. L. & Kronberg, P. P., 1998, ApJ, 502, 218

[6] Anantharamaiah, K. R., Viallefond, F., Mohan, N. R., Goss, W. M. & Zhao, J.H., 2000, ApJ, 537, 613

[7] Anantharamaiah, K. R., Zhao, Jun-Hui, Goss, W. M. & Viallefond, F., 1993, ApJ, 419, 585

[8] Anantharamaiah, K. R. & Goss, W. M., 1990, Radio Recombination Lines: 25 Years of Investigation, ed: M. A. Gordon and R. L. Sorochenko, Kluwer Academic Publishers, 267

[9] Andersson, M., & Garay, G. 1986, A&A, 167, L1

[10] Antonucci, R. R. J., & Ulvestad, J.,1988, ApJ, 330, L97

[11] Arnaboldi, M., Capaccioli, M., Cappellaro, E., Held, E. V., Koribalski, B. ,1995, AJ, 110, 199

[12] Baan, W. A., 1985, Nature, 315, 26

[13] Baan, W. A., Gusten, R. & Haschick, A. D., 1986, ApJ, 305, 830

[14] Baan, W. A., & Haschick, A. D., 1995, ApJ, 454, 745

[15] Baan, W. A., & Haschick, A. D., 1984, ApJ, 279, 541

[16] Bartel, N., Ratner, M. I., Rogers, A. E. E., Shapiro, I. I., Bonometti, R. J., Cohen, N. L., Gorenstein, M. V., Marcaide, J. M., & Preston, R. A., 1987, ApJ, 323, 505

[17] Bell, M. B., & Seaquist, E. R., 1978, ApJ, 223, 378

[18] Benson, J., & Johnston, K. 1984, ApJ, 277, 181

[19] Boomsma, R., Oosterloo, T. A., Fraternali, F., van der Hulst, J. M., Sancisi, R., 2005, A&A, 431, 65

[20] Briggs, D. 1995, Ph.D. thesis, New Mexico Institute of Mining and Technology

[21] Campbell, M.F., Garland, C.A., Deutsch, L.K., Hora, J.L., Fazio, G.G., Dayal, A., & Hoffmann, W.F. 2000, ApJ, 536, 816

[22] Canzian, B., Mundy L. G., & Scoville, N. Z., 1988, ApJ, 333, 157

[23] Carilli, C. L., Holdaway, M. A., Ho. P. T. P., De Pree, C. G., 1992, ApJ, 399, L59

[24] Carral, P., Kurtz, S., Rodríguez, L. F., Martí, J., Lizano, S., & Osorio, M. 1999, RevMexAA, 35, 97

[25] Carral, P., & Welch, W.J., 1992, ApJ, 385, 244

[26] Carral, P., Welch, W. J., & Wright, M. C. H. 1987, RevMexAA, 14, 506

[27] Cesaroni, R., Walmsley, C.M., Kömpe, C., & Churchwell, E. 1991, A&A, 252, 278

[28] Chaisson, E. J., & Rodríguez, L. F., 1977, ApJ, 214, L111

[29] Churchwell, E., Walmsley, C. M., & Wood, D. O. S. 1992, A&A, 253, 541

[30] Clements, D. L., & Baker, A. C., 1996, A&A, 314, L5

[31] Colbert, J. W. et al., 1999, ApJ, 511, 721

[32] Das, M., Anantharamaiah, K. R., & Yun, M. S., 2001, ApJ, 549, 896

[33] de Vaucouleurs, G., de Vaucouleurs, A., & Corwin, H. G., 1976, Second Reference Catalogue of Bright Galaxies (University of Texas Press, Austin)

[34] Dietz, R. D., Smith, J., Hackwell, J. A., Gehrz, R. D., & Grasdalen, G. L., 1986, AJ, 91, 758

[35] Downes, D., & Solomon, P. M., 1998, ApJ, 507, 615

[36] Downes, D., Reynaud D., Solomon, P. M., & Radford, S. J. E., 1996, ApJ, 461, 186

[37] Downes, D., Wilson, T. L., Bieging, J., & Wink, J. 1980, A&AS, 40, 379

[38] Dupree, A. K. & Goldberg, L. 1970, ARAA, 8, 231

[39] Eckart, A., & Downes, D., 2001, ApJ, 551, 730

[40] Engelbracht, C. W., Rieke, M. J., Rieke, G. H., Kelly, D. M., & Achtermann, J. M., 1998, ApJ, 505, 639

[41] Fey, A.L., Gaume, R.A., Nedoluha, G.E., & Claussen, M.J. 1994, ApJ, 435, 738

139

[42] Fey, A. L., Claussen, M. J., Gaume, R. A., Nedoluha, G. E., & Johnston, K. J., 1992, AJ, 103, 234

[43] Forbes, D. A., & De Poy, D. L., 1992, A&A, 259, 97

[44] Forbes, D. A., Polehampton, E., Stevens, I. R., Brodie, J. P., & Ward, M. J., 2000, MNRAS, 312, 689

[45] Friedli, D., & Martinet, L., 1993, A&A, 277, 27

[46] Garay, G., & Lizano, S. 1999, PASP, 111, 1049

[47] Garay, G., Lizano, S., Gómez, Y., 1994, ApJ, 429, 268

[48] Garay, G., Reid, M. J., & Moran, J. M. 1985, ApJ, 289, 681

[49] Garay, G., & Rodríguez, L. F. 1990, ApJ, 362, 191

[50] Garay, G., Rodríguez, L. F., & van Gorkom, J. H., 1986, ApJ, 309, 553

[51] Garay, G. & Rodríguez, L. F., 1983, ApJ, 266, 263

[52] Gaume, R. A., Fey, A. L., & Claussen, M. J. 1994, ApJ, 432, 648

[53] Gaume, R. A., & Mutel, R. L. 1987, ApJS, 65, 193

[54] Genzel, R., et al. 1998, ApJ, 498, 579

[55] Genzel, R., Ho, P. T. P., Bieging, J., & Downes, D. 1982, ApJ, 259, L103

[56] Genzel, R., & Downes, D. 1977, A&AS, 30, 145

[57] Gonzalez-Alfonso, E., Smith, H. A., Fischer, J., & Cernicharo, J. 2004, ApJ, 613, 247

[58] Gómez, Y., Rodríguez, L. F., Garay, G., & Moran, J. M. 1991, ApJ, 377, 519

[59] Gómez, Y., Rodríguez-Rico, C. A., Rodríguez, L. F., & Garay, G., 2000, RevMexAA, 36, 161

[60] Greve, A., Wills, K. A., Neininger, N., & Pedlar, A., 2002, A&A, 383, 56

[61] Harju, J., Walmsley, C. M., & Wouterloot, J. G. A. 1993, A&AS, 98, 51

[62] Harvey, P. M. & Forveille, T. 1988, A&A, 107, L19

[63] Hatchell, J., Fuller, G.A. & Millar, T.J. 2001, A&A, 372, 281

[64] Heaton, B. D., Little, L. T, Yamashita, T., Davies, S. R., Cunningham, C. T., & Monteiro, T. S., 1993, A&A, 278, 238

[65] Heaton, B. D., Little, L. T, & Bishop, I. S., 1989, A&A, 213, 148

[66] Heaton, B. D., Matthews, N., Little, L. T., & Dent, W. R. F. 1985, MNRAS, 217, 485

[67] Henkel, C., Wilson, T. L., & Mauersberger, R. 1987, A&A, 182, 137

[68] Hofner, P. & Churchwell, E. 1996, A&AS, 120, 283

[69] Huang, Z. P., Thuan, T. X., Chevalier, R. A., Condon, J. J., & Yin, Q. F., 1994, ApJ, 424, 114

[70] Hunter, T. R., Neugebauer, G., Benford, D. J., Matthews, K., Lis, D. C., Serabyn, E., & Phillips, T. G. 1998, ApJ, 493, L97

[71] Kennicutt, 1998, ARAA

[72] Keto, E., Ho, P. T. P., & Reid, M. J. 1987, ApJ, 323, 117

[73] Kronberg, P. P., Biermann, P., & Schwab, F. R., 1985, ApJ, 291, 693

[74] Kuchar, T. A., & Bania, T. M. 1994, ApJ, 436, 117

[75] Kurtz, S., Churchwell, E. & Wood, D.O.S. 1994, ApJS, 91, 659

[76] Larkin, J. E., Graham, J. R., Matthews, K., Soifer, B. T., Beckwith, S., Herbst, T. M., Quillen, A. C., 1994, ApJ, 420, 159

[77] Lester, D. F., Gaffney, N., Carr, J. S., & Joy, M., 1990, ApJ, 352, 544

[78] Lonsdale, C. J., Lonsdale, C. J., Diamond, P. J., & Smith, H. E., 1998, ApJ, 493, 13

[79] Matsumoto, H., & Tsuru, T. G., 1999, PASJ, 51, 321

[80] Matsushita, S., Kawabe, R., Matsumoto, H., Tsuru, T. G., Kohno, K., Morita, K., Okumura, S. K., & Vila-Vilarbo, B., 2000, ApJ, 545, 107

[81] McDonald, A. R., Muxlow, T. W. B., Wills, K. A., Pedlar, A., & Beswick, R., 2002, MNRAS, 334, 912

[82] McKeith, C. D., Castles, J., Greve, A., & Downes, D., 1993, A&A, 272, 98

[83] McKeith, C. D., Greve, A., Downes, D., Prada, F., 1995, A&A, 293, 703

[84] Mohan, N., Goss, W. M., & Anantharamaiah, K. R., 2005, A&A, 432, 1

[85] Mohan, N. R., Anantharamaiah, K. R., & Goss, W. M., 2002, ApJ, 574, 701

[86] Mundell, C. G., Ferruit, P., & Pedlar, A., 2001, ApJ, 560, 168

[87] Muxlow, T. W. B., Pedlar, A., Wilkinson, P. N., Axon, D. J., Sanders, E. M., & de Bruyn, A. G., 1994, MNRAS, 266, 455

[88] Nakai, N., Inoue, M., Miyazawa, K., Miyoshi, M., & Hall, P., 1995, PASJ, 47, 771

[89] Natta, A., Palla, F., Preite-Martinez, A., & Panagia, N. 1981, A&A, 99, 289

[90] Norris, R. P., Baan, W. A., Haschick, A. D., Diamond, P. J., & Booth, R. S., 1985, MNRAS, 213, 821

[91] Norris, R. P., 1988, MNRAS, 230, 345

[92] Paglione, T. A. D., Yam, O., Tosaki, T., & Jackson, J. M., 2004, ApJ, 611, 835

[93] Paglione, T. A. D., Tosaki, T., & Jackson, J. M., 1995, ApJ, 454, L117

[94] Panagia, N., 1973, AJ, 78, 929

[95] Pence, W. D., 1981, ApJ, 247, 473

[96] Peng, R., Zhou, S., Whiteoak, J. B., Lo, K. Y., & Sutton, E. C., 1996, ApJ, 470, 821

[97] Piña, R. K., Jones, B., Puetter, R. C. & Stein, W. A., 1992, ApJ, 401, L75

[98] Prada, F., Gutierrez, C. M., & McKeith, C. D., 1998, ApJ, 495, 765

[99] Puxley, P. J., Mountain, C. M., Brand, P. W. J. L., Moore, T. J. T., & Nakai, N., 1997, ApJ 485, 143

[100] Reid, M.J. & Ho, P.T.P. 1985, ApJ, 288, L17

[101] Rodríguez, L. F., Moran, J. M., Gottlieb, E. W., & Ho, P. T. P., 1980, ApJ, 235, 845

[102] Rodríguez-Rico, C. A., Goss, W. M., Viallefond, F., Zhao, J. H., Gómez, Y., & Anantharamaiah, K. R., 2005, accepted

[103] Rodríguez-Rico, C. A., Viallefond, F., Zhao, J.-H., Goss, W. M., & Anantharamaiah, K. R., 2004, ApJ, 616, 783

[104] Roelfsema, P. R., 1987, PhDT, Univ. Groningen, 126

[105] Rovilos, E., Diamond, P. J., Lonsdale, C. J., Lonsdale, C. J., Smith, H. E., 2003, MNRAS, 342, 373

[106] Ryle, M., & Downes, D. 1967, ApJ, 148. L17

[107] Sakamoto, K., Scoville, N. Z., Yun, M. S., Crosas, M., Genzel, R., & Tacconi, L. J., 1999, ApJ, 514, 68

[108] Salem, M., & Brocklehurst, M., 1979, ApJS, 39, 633

[109] Sanders, D. B., & Mirabel, I. F., 1996, ARA&A, 34, 749

[110] Schraml, J., & Mezger, P. G., 1969, ApJ, 156, 269

[111] Schwab, F. 1980, Proc. SPIE, 231, 18

[112] Scoville, N. Z., Sargent, A. I., Sanders, D. B., & Soifer, B. T., 1991, ApJL, 366, 5

[113] Scoville, N. Z. et al., 1998, ApJ, 492, 107

[114] Scoville, N. Z., Soifer, B. T., Neugebauer, G., Matthews, K., Young, J. S., & Yerka, J., 1985, ApJ, 289, 129

[115] Scoville, N. Z., & Kwan, J. 1976, ApJ, 206, 718

[116] Seaquist, E. R., & Bell, M. B., 1977, A&A, 601, 1

[117] Seaquist, E. R., Bell, M. B., & Bignell, R. C., 1985, ApJ, 294, 546

[118] Seaquist, E. R., Carlstrom, J. E., Bryant, P. M., & Bell, M. B., 1996, ApJ, 465, 691

[119] Shopbell, P.L., Bland-Hawthorn, J., 1998, ApJ 493, 129

[120] Smith, H. E., Lonsdale, C. J., Lonsdale, C. J., & Diamond, P. J., 1998, 493, 17

[121] Soifer, B. T., et al. 1984, ApJ, 283, 1

[122] Solomon, P. M., Downes, D., & Radford, S. J. E., 1992, ApJL, 387, 55

[123] Telesco, C. M., Joy, M., Dietz, K., Decher, R., Campins, H., 1991, ApJ, 369, 135

[124] Turner, B. E., Balick, B., Cudaback, D. D., Heiles, C., & Boyle, R. J., 1974, ApJ, 194, 279

[125] Turner, J. L., & Ho, P. T. P., 1985, ApJ, 299, L77

[126] Ulvestad, J., & Antonucci, R. R. J.,1997, ApJ, 488, 621

[127] Watt, S., & Mundy, L. G. 1999, ApJS, 125, 143

[128] Weaver, K. A., Heckman, T. M., Strickland, D. K., Dahlem, M., 2002, ApJ, 576, L19

[129] Weiss, A., Walter, F., Neininger, N., Klein, U., 1999, A&A, 345, 23

[130] Wills, K. A., Pedlar, A., Muxlow, T. W. B., & Wilkinson, P. N., 1997, MNRAS, 291, 517

[131] Wills, K. A., Das, M., Pedlar, A., Muxlow, T. W. B., & Robinson, T. G., 2000, MNRAS, 316, 33

[132] Wood, D.O.S., Churchwell, E. 1989, ApJS, 69, 835

[133] Zhao, J. H., Goss, W. M., Ulvestad, J. S., & Anantharamaiah, K. R., 2001, ASCP, 240, 404

[134] Zhao, J. H., Goss, W. M., Ulvestad, J., & Anantharamaiah, K. R., ASP Conference Series, 2000

[135] Zhao, J. H., Anantharamaiah, K. R., Goss, W. M., & Viallefond, F., 1996, ApJ, 472, 54

[136] Zheng, X., Reid, M.J., & Moran, J.M. 2000, A&A, 357, L37

[137] Zijlstra, A. A., Pottasch, S. R., Engels, D., Roelfsema, P. R., Te-Lintel Hekkert, P., & Umana, G. 1990, MNRAS, 246, 217.